



NNT number of order : 2016 LYSE1046

DOCTORAL THESIS OF UNIVERSITY OF LYON

Carried out in
University Claude Bernard – Lyon 1

Doctoral School N° 160
Électronique, Électrotechnique, Automatique de Lyon

Specialisation in : Information and Communication Sciences and
Technologies for Health

Discipline : Signal Processing

Publicly defended the 29/03/2016, by :

Omer Faruk EKER

IMPACT OF INTRACRANIAL ANEURYSM ON THE PARENT VESSEL HEMODYNAMIC

From *in vitro* observation to *in vivo* exploration

Members of the thesis JURY :

FOURNEL Thierry, Professeur, Université Saint-Étienne	President of the jury
ESTÈVE François, Professeur, CHU de Grenoble	Reviewer
FIEHLER Jens, Uni-Klinik de Hambourg – Eppendorf	Reviewer
LIEBGOTT Hervé, Maître de Conférence, UCBL Lyon 1	Jury
COURBEBASSE Guy, Docteur, INSA Lyon	Director
COSTALAT Vincent, Professeur, CHU de Montpellier	Co-director
BONAFÉ Alain, Professeur, CHU de Montpellier	Invited member



NNT number of order : 2016 LYSE1046

DOCTORAL THESIS OF UNIVERSITY OF LYON

Carried out in
University Claude Bernard – Lyon 1

Doctoral School N° 160
Électronique, Électrotechnique, Automatique de Lyon

Specialisation in : Information and Communication Sciences and
Technologies for Health

Discipline : Signal Processing

Publicly defended the 29/03/2016, by :

Omer Faruk EKER

IMPACT OF INTRACRANIAL ANEURYSM ON THE PARENT VESSEL HEMODYNAMIC

From *in vitro* observation to *in vivo* exploration

Members of the thesis JURY :

FOURNEL Thierry, Professor, Université Saint-Étienne	President of the jury
ESTÈVE François, Professor, CHU de Grenoble	Reviewer
FIEHLER Jens, Professor, UniKlinik Hambourg-Eppendorf	Reviewer
LIEBGOTT Hervé, Associate Professor, UCBL Lyon 1	Jury
COURBEBASSE Guy, Doctor, INSA Lyon	Director
COSTALAT Vincent, Professor, CHU de Montpellier	Co-director
BONAFÉ Alain, Professor, CHU de Montpellier	Invited member

UNIVERSITE CLAUDE BERNARD - LYON 1

Président de l'Université

Vice-président du Conseil d'Administration
Vice-président du Conseil des Etudes et de la Vie
Universitaire
Vice-président du Conseil Scientifique
Directeur Général des Services

M. François-Noël GILLY

M. le Professeur Hamda BEN HADID
M. le Professeur Philippe LALLE

M. le Professeur Germain GILLET
M. Alain HELLEU

COMPOSANTES SANTE

Faculté de Médecine Lyon Est – Claude Bernard
Faculté de Médecine et de Maïeutique Lyon Sud – Charles
Mérieux
Faculté d'Odontologie
Institut des Sciences Pharmaceutiques et Biologiques
Institut des Sciences et Techniques de la Réadaptation
Département de formation et Centre de Recherche en
Biologie Humaine

Directeur : M. le Professeur J. ETIENNE
Directeur : Mme la Professeure C. BURILLON
Directeur : M. le Professeur D. BOURGEOIS
Directeur : Mme la Professeure C.
VINCIGUERRA
Directeur : M. le Professeur Y. MATILLON
Directeur : Mme. la Professeure A-M. SCHOTT

COMPOSANTES ET DEPARTEMENTS DE SCIENCES ET TECHNOLOGIE

Faculté des Sciences et Technologies
Département Biologie
Département Chimie Biochimie
Département GEP
Département Informatique
Département Mathématiques

Département Mécanique
Département Physique
UFR Sciences et Techniques des Activités Physiques et
Sportives
Observatoire des Sciences de l'Univers de Lyon
Polytech Lyon
Ecole Supérieure de Chimie Physique Electronique
Institut Universitaire de Technologie de Lyon 1
Ecole Supérieure du Professorat et de l'Education

Institut de Science Financière et d'Assurances

Directeur : M. F. DE MARCHI
Directeur : M. le Professeur F. FLEURY
Directeur : Mme Caroline FELIX
Directeur : M. Hassan HAMMOURI
Directeur : M. le Professeur S. AKKOUCHE
Directeur : M. le Professeur Georges
TOMANOV
Directeur : M. le Professeur H. BEN HADID
Directeur : M. Jean-Claude PLENET
Directeur : M. Y. VANPOULLE

Directeur : M. B. GUIDERDONI
Directeur : M. le Professeur E. PERRIN
Directeur : M. G. PIGNAULT
Directeur : M. le Professeur C. VITON
Directeur : M. le Professeur A. MOUGNIOTTE
Directeur : M. N. LEBOISNE

Acknowledgments

*Firstly, I would like to thank Professor **Thierry Fournel** for honouring my jury by presiding it.*

*I would like to thank my thesis director Doctor **Guy Courbebaisse** for his helping hand, infinite patience and support throughout my thesis period.*

*I would like to thank my thesis co-director Professor **Vincent Costalat** for his support, wise advices and mostly for his inexhaustible energy.*

*I would like to acknowledge specially Professor **Alain Bonafé** who gave me the opportunity to pursue my journey in interventional neuroradiology. He is an unvaluable source of inspiration.*

*I would like to thank warmly Professor **François Estève** who got me interested in mathematics. I am glad he accepted to be a member of the jury of this thesis*

*I would like to thank Professor **Jens Fiehler** for the challenge he took in accepting to honor my jury by his presence. I appreciate particularly his precise and efficient reviewing of the my work.*

*I also thank Associate Professor **Hervé Liebgott** who accepted to honor my jury by his presence. I particularly appreciated his Masters courses that made me discover the world of the ultrasounds.*

*Finally and especially, I would like to thank my family for their
unfailing love, support and encouragement.*

*I would like to thank especially Eloise for
her English corrections and her love.*

*Last but not least, I also want to thanks all my friends and fellows
who shared my journey during these four years of work.*

Thesis abstract

Intracranial aneurysms are the most common lethal predisposition amongst young adults. Its understanding remains limited to date while the development of new innovative endovascular treatments are increasingly available and allow for the treatment of more and more complex aneurysms with a non negligible rate of complications. Most of the previous studies on intracranial aneurysms are based on low informative clinical series and/or are limited by the use of numerical simulation methods. The latter's reliability depends on physiological boundary conditions that are difficult to assess in clinical practice. In addition, these works almost exclusively target the intrasaccular mechanical phenomena irrespective of the interconnection between the aneurysm and the parent vessel. Indeed, the flow modifications inside the parent vessel have been largely neglected. In this context and as part of this research work, we have explored the impact of intracranial aneurysms on the hemodynamic conditions within the parent artery. First, the use of a cardiovascular simulator replicating pulsatile flow conditions measured *in vivo* and a patient-specific silicone model of aneurysm allowed to assess the aneurysm's impact on the parent vessel *in vitro*. It was characterised by a measurable and significant decrease of the resistance of the hydraulic circuit containing the aneurysm and its parent artery ($P < 0.001$). The deployment of a flow diverter stent within the parent artery allowed for the correction of the resistance modification. Secondly, this effect of intracranial aneurysms has been confirmed *in vivo* by the follow-up with 2D phase-contrast MRI of a patient cohort treated for intracranial aneurysms. The patients were treated by the endovascular flow diversion technique. They were compared to a control group of healthy subjects. *In vivo*, intracranial aneurysms were responsible for a demodulated blood flow and a collapse of the resistive and pulsatility indexes within the parent vessel segments downstream to the aneurysms ($P < 0.001$). These effects were significantly correlated to the aneurysm volume ($R = -0.90$, $P < 0.01$ for the modification of the resistive index and $R = -0.89$, $P < 0.01$ for the modification of the pulsatility index). The monitoring of the patients after the endovascular treatment demonstrated and also quantified the corrective effect of the flow diverter stents on the hemodynamic disturbances induced by the aneurysms and its stability over time. They allowed for the "hemodynamic reconstruction" of the parent artery by the restoration of a normo-modulated blood flow and normal resistive and pulsatility indexes within its downstream segment to the aneurysm. In the framework of this study, a new method for the segmentation of the internal carotid artery on 2D phase-contrast MRI was proposed. The method is based on a Fourier Transform analysis of the MR flow images, and especially of the velocities within each voxel during the cardiac cycle. It was characterised and validated. This new approach operating directly on the phase images was compared to two validated methods: the manual segmentation and the segmentation based on the active contours method according to Chan-Vese model. The analysis of the segmentation results (arterial sections, average velocities and average flow rates) showed a very high consistency with the results of the two reference methods (Lin concordance correlation coefficient > 0.95).

Keywords : arterial hemodynamic, endovascular flow diversion, flow diverter stent, Fourier transform, internal carotid artery, intracranial aneurysm, parent artery, resistive index, pulsatility index, phase-contrast MRI, segmentation.

Résumé de thèse

L'anévrisme intracrânien (AI) est la prédisposition mortelle la plus fréquente chez le sujet jeune. La compréhension de cette pathologie demeure limitée alors que nous assistons au développement de nouveaux traitements endovasculaires toujours plus innovants et permettant le traitement d'anévrismes de plus en plus complexes avec cependant des taux de complications non négligeables. La majorité des études précédemment rapportées sur les AIs est basée sur des séries cliniques peu informatives et/ou limitées par l'utilisation de méthodes de simulation numérique. La fiabilité de ces dernières dépend essentiellement des conditions hémodynamiques aux limites qui sont difficiles à évaluer en pratique clinique. En outre, ces travaux ciblent presque exclusivement les phénomènes mécaniques intrasacculaires sans tenir compte de l'interdépendance de l'anévrisme et de l'artère porteuse. Ainsi, les modifications d'écoulement induites par l'anévrisme au sein du vaisseau porteur sont largement négligées dans la littérature. Dans ce contexte et dans le cadre de ce travail de recherche, nous avons exploré l'impact des AIs sur les conditions hémodynamiques au sein de l'artère porteuse. Dans un premier temps, l'utilisation d'un simulateur cardiovasculaire reproduisant les conditions d'écoulement pulsatile mesurées *in vivo* et d'un modèle d'anévrisme en silicone patient-spécifique a permis d'évaluer l'impact de l'AI sur le vaisseau porteur *in vitro*. Cet impact était caractérisé par une diminution mesurable de la résistance du circuit hydraulique du banc d'essai contenant le modèle d'anévrisme et son artère porteuse ($P < 0,001$). Le déploiement d'un stent flow diverter (SFD) au sein du vaisseau porteur permettait la correction de cette modification de résistance. Dans un second temps, cet effet de l'AI sur son artère porteuse a été confirmé *in vivo* par le suivi en IRM en contraste de phase 2D d'une cohorte de patients traités pour des AIs par la technique de diversion de flux endovasculaire. Ils ont été comparés à un groupe contrôle de sujets sains. *In vivo*, les AIs étaient responsables d'une démodulation du flux sanguin et d'un effondrement significatif des index de résistance (IR) et de pulsativité (IP) du segment du vaisseau porteur en aval de la malformation ($P < 0,001$). Les modifications hémodynamiques au sein du vaisseau porteur ont été quantifiées et suivies après le traitement endovasculaire. L'importance de ces modifications était corrélée au volume de l'anévrisme ($R = -0,90$, $P < 0,01$ pour les modifications d'IR et $R = -0,89$, $P < 0,01$ pour les modifications d'IP). L'effet correcteur de la diversion de flux endovasculaire sur les modifications hémodynamiques induites par l'anévrisme ainsi que sa stabilité au cours du temps ont pu être objectivés. La technique de diversion de flux endovasculaire permettait une « reconstruction hémodynamique » de l'artère porteuse par la restauration d'un flux sanguin normo-modulé et d'index de résistance et de pulsativité dans les limites de la normale au sein du segment artériel en aval de la malformation. Dans le cadre de cette étude, une nouvelle méthode pour la segmentation de l'artère carotide interne en IRM en contraste de phase 2D a été proposée. La méthode est basée sur une analyse de la transformée de Fourier des images, et en particulier des vitesses au sein de chaque voxel au cours du cycle cardiaque. La méthode a été caractérisée et validée. Cette nouvelle approche opérant directement sur les images de phase a été comparée à deux méthodes validées : la segmentation manuelle et la segmentation basée sur les contours actifs selon le modèle de Chan-Vese. L'analyse des résultats de segmentation (aires des sections artérielles, vitesses moyennes et débits moyens) a montré une très grande concordance entre les résultats de la méthode proposée et les résultats des deux méthodes de référence (coefficient de corrélation de concordance de Lin $> 0,95$).

Mots clés : artère carotide interne, anévrisme intracrânien, artère porteuse, diversion de flux endovasculaire, hémodynamique artérielle, index de résistance, index de pulsativité, IRM en contraste de phase 2D, segmentation, stent flow diverter, Transformée de Fourier.

TABLE OF CONTENTS

1	General Introduction	21
1.1	Context and objective	21
1.2	Contributions.....	23
1.3	Chapters	24
2	State of the art	27
2.1	Epidemiology of intracranial aneurysms	27
2.2	Treatment of intracranial aneurysms	27
2.3	The issue of giant intracranial aneurysms	28
2.4	Flow diversion technique for the treatment of intracranial aneurysms	28
2.5	Its Hemodynamics in the intracranial aneurysms	29
2.6	Methods for <i>in vivo</i> measurements of arterial velocities and flow rates.....	31
2.7	Doppler ultrasounds technique.....	31
2.7.1	<i>Principle of Doppler ultrasounds</i>	31
2.7.2	<i>Endovascular application of Doppler ultrasounds</i>	32
2.8	Phase-contrast MRI technique	33
2.8.1	<i>Principle of phase-contrast MRI</i>	34
2.8.2	<i>Velocity encoding in phase-contrast MRI</i>	36
2.8.3	<i>ECG Synchronization</i>	36
2.8.4	<i>2D or 3D acquisitions in phase-contrast MRI</i>	38
2.9	Image segmentation.....	38
2.9.1	<i>Manual segmentation method</i>	39
2.9.2	<i>Automated segmentation methods</i>	39
2.9.3	<i>Active contours method for segmentation</i>	40
2.10	The internal carotide artery : a particular case for segmentation	42
2.10.1	<i>Anatomy of the internal carotide artery</i>	42
2.10.2	<i>Segmentation of the internal carotide artery</i>	42
3	Aneurysm and parent vessel : an <i>in vitro</i> study of pressures and resistance	45
3.1	Introduction	45
3.2	Materials and Methods	46
3.2.1	<i>Cardiovascular simulator</i>	47
3.2.2	<i>Silicone aneurysm models and flow diverter stents</i>	50
3.2.3	<i>Pressures and resistance measurements in the parent vessel</i>	52
3.2.4	<i>Fluid movements between the aneurysms and the parent vessel</i>	53
3.2.5	<i>Input flow instruction : an <i>in vivo</i> measured pulsatile flow</i>	56
3.2.6	<i>Statistical analysis</i>	56
3.3	Results	58
3.3.1	<i>Measured pressures and upstream and downstream to the aneurysm</i>	58
3.3.2	<i>Intrasaccular residency time of the fluid</i>	64
3.4	Discussion.....	65
3.5	Conclusion	67
4	Aneurysm and parent vessel : an <i>in vivo</i> study of flow rates, pulsatility and resistance ...69	
4.1	Introduction	69
4.2	Materials and methods	69
4.2.1	<i>Patient and control groups</i>	69
4.2.2	<i>Aneurysm population : endovascular treatment and morphological analysis</i>	70

4.2.3	<i>MRI examinations including 2D PC-MRI</i>	70
4.2.4	<i>Image post-processing</i>	71
4.3	Results	74
4.3.1	<i>Aneurysms characteristics and treatment details</i>	74
4.3.2	<i>2D PC-MRI of the ICA</i>	76
4.3.3	<i>Resistive and Pulsatility indexes ratios</i>	76
4.3.4	<i>Volumetric blood flow rates</i>	81
4.3.5	<i>Volumetric flow rate waveforms</i>	82
4.4	Discussion	83
4.5	Conclusion	86
5	2D PC-MRI segmentation : an original Fourier Transform based approach	87
5.1	Introduction	87
5.1.1	<i>Active contours method according to the Chan-Vese model for segmentation</i>	87
5.1.2	<i>New method of segmentation based on a Fourier Transform analysis</i>	91
5.2	Materials and methods	95
5.2.1	<i>Population and 2D PC-MRI examinations</i>	95
5.2.2	<i>Segmentation of 2D PC-MRI by three different methods</i>	96
5.2.3	<i>Analysis of the impact of the Fourier Transform amplitude threshold</i>	97
5.2.4	<i>Parameters of analysis : average, resistive and pulsatility equivalent indexes</i>	97
5.2.5	<i>Normalization of the average, resistive and pulsatility equivalent indexes</i>	98
5.2.6	<i>Agreement analysis of the segmentation results by the three segmentation methods</i>	98
5.3	Results	99
5.3.1	<i>MRI flow parameters</i>	99
5.3.2	<i>Manual Method : agreement analysis between two examiners</i>	100
5.3.3	<i>Agreement analysis of the segmentations by MM and ACM-CV</i>	100
5.3.4	<i>FTM : effect of varying the amplitude threshold on the segmentation results</i>	103
5.3.5	<i>Agreement analysis : FTM versus MM and FTM versus ACM-CV</i>	106
5.4	Discussion.....	107
6	General conclusion	109
7	References	115
8	Appendix	123
8.1	APPENDIX 1	123
8.2	APPENDIX 2	124
8.3	APPENDIX 3	125
8.4	APPENDIX 4	126
8.5	APPENDIX 5	127
8.6	APPENDIX 6	128
8.7	APPENDIX 7	129
8.8	APPENDIX 8	130
8.9	APPENDIX 9	131
8.10	APPENDIX 10	132

TABLE OF FIGURES

Figure 1 : Slowing flow downstream to a giant aneurysm. Exemples of DSA and TOF MRI images.	22
Figure 2 : The Principle of the Doppler ultrasounds.....	32
Figure 3: The application of the Doppler ultrasounds to endovascular exploration	33
Figure 4: The Principle of the Phase-contrast MRI.....	35
Figure 5: Illustration of 2D PC-MRI of intrapetrouse ICA	35
Figure 6 : The Principles of the Phase-contrast MRI ECG synchronization.....	38
Figure 7 : The Principle of the cardiovascular simulator (test bench).....	47
Figure 8 : The Principle of the flow regulation by the cardiovascular simulator.....	48
Figure 9 : Tested aneurysm silicone models.....	51
Figure 10 : The Pipeline TM Stent flow diverter.....	52
Figure 11 : Set up of the experiments 2 and 3.	54
Figure 12 : The segmentation of the intrasaccular RBCs distribution over one cardiac cycle.....	55
Figure 13 : The set point pulsatile flow used as input to the cardiovascular simulator.....	57
Figure 14: Flow rate curves over time measured in experiments 1 and 2.	59
Figure 15 : Pressure P1 measured before and after the FDS deployment with aneurysm A	60
Figure 16 : Pressure P2 measured before and after the FDS deployment with aneurysm A.	61
Figure 17 : Pressure P1 measured before and after the FDS deployment for the straight pipe.....	62
Figure 18 : Pressure P2 measured before and after the FDS deployment for the straight pipe.....	63
Figure 19 : area fraction of the aneurysmal sac occupied by the RBCs over time.....	64
Figure 20 : The 2D PC-MRI slices upstream and downstream to the aneurysm.....	72
Figure 21 : VFR waveform features of the ICA over a cardiac cycle.....	73
Figure 22 : Correlation analysis between RI-ratios, PI-ratios and the volumes.....	79
Figure 23 : Correlation analysis between RI-ratios, PI-ratios and the volumes.....	80
Figure 24 : Barplots of resistive index (RI) of the different groups and subgroups.	80
Figure 25 : Barplots of Pulsatility index (RI) of the different groups and subgroups.....	81
Figure 26 : Normalized VFR waveforms for volunteers group and patient group before EVT.	82
Figure 27 : Normalized VFR waveforms for patient group, subgroup A and subgroup B.	83
Figure 28 : Simplified illustration of the active contours and its sets (inside and outside).	88
Figure 29 : Exemple of an ICA 2D PC-MRI segmented with ACM-CV.	90
Figure 30 : Difference in velocity curve and FT result between a vessel and noise.....	91
Figure 31 : Principle of the segmentation of PC-MRI with FTM.....	93
Figure 32: Principle of the segmentation of PC-MRI with FTM.	94
Figure 33 : Positioning of 2D PC-MRI slice on the ICA.	95
Figure 34 : Agreement analysis between manual segmentations by users 1 and by user 2.	101
Figure 35 : Agreement analysis of MM and ACM-CV from segmentation.	102
Figure 36: The impact of the FT amplitude threshold on the area, velocity and flow rate curves.....	103
Figure 37: The impact of the Amp on the normalised area, Average, RI and PI values of A, V and D.....	105
Figure 38: Evolution of the CCCvalues averaged on the five subjects as function of Amp.	107

TABLE OF TABLES

Table 1 : Results of flow, pressure measurements and resistance calculations in the experiments 1 to 4. 58
Table 2 : Morphologic characteristics of the aneurysms in patient group 75
Table 3 : Values of resistive index (RI) and RI-ratio. 78
Table 4 : Values of resistive index (PI) and PI-ratio..... 78
Table 5 : Characteristics of the volunteers imaged with 2D PC-MRI..... 100

ABBREVIATIONS

ACM : active contours method
ACM-CV : active contours method according to the model of Chan-Vese
Amp : threshold of the Fourier transform amplitude
CCC : concordance correlation coefficient
CFD : computational fluid dynamic
CSF : cerebro-spinal fluid
 Q_{\max} : maximum mean flow rate
 Q_{\min} : minimum mean flow rate
 Q_{moy} : average mean flow rate
ECA : external carotid artery
EVT : endovascular treatment
FDS : flow diverter stent
FT : Fourier transform
FTM : Fourier transform based method of segmentation
IA : Intracranial aneurysm
ICA : internal carotid artery
MM : manual method of segmentation
UIA : unruptured intracranial aneurysm
RIA : Ruptured Intracranial Aneurysm
 A_{average} : mean value of area over a cardiac cycle (= area under the curve)
 V_{average} : mean value of velocity over a cardiac cycle (= area under the curve)
 D_{average} : mean value of flow rate area over a cardiac cycle (= area under the curve)
MRA : magnetic resonance angiography
MRI : magnetic resonance imaging
 nA_{average} : normalized mean value of area over a cardiac cycle
 nV_{average} : normalized mean value of velocity over a cardiac cycle
 nD_{average} : normalized mean value of flow rate area over a cardiac cycle
 $nPIA$: normalized pulsatility index on the curve of area over the time
 $nPID$: normalized pulsatility index on the curve of mean Flow rate over the time
 $nPIV$: normalized pulsatility index on the curve of mean velocity over the time
 $nRIA$: normalized resistive index on the curve of area over the time
 $nRID$: normalized resistive index on the curve of mean Flow rate over the time
 $nRIV$: normalized resistive index on the curve of mean velocity over the time
VFR : volumetric flow rate
mVFR : mean volumetric flow rate
PC-MRA : phase contrast magnetic resonance angiography
PC-MRI : phase contrast magnetic resonance imaging
PI : pulsatility index
PIA : pulsatility index on the curve of area over the time
PID : pulsatility index on the curve of mean flow rate over the time
PIV : pulsatility index on the curve of mean velocity over the time
PI-ratio : pulsatility indexes ratio
PED : pipeline endovascular device
RI : resistive index
RIA : resistive index on the curve of area over the time
RID : resistive index on the curve of mean flow rate over the time
S/N : signal on noise ratio

RIV : resistive index on the curve of mean velocity over the time
RI-ratio : resistive indexes ratio
S/N : signal noise ratio
TR : repetition time
TE : echo time
TOF : time of flight
VENC : velocity encoding
VFR (VBFR) : volumetric flow rate (volumetric blood flow rate)

CHAPTER 1

1 General Introduction

1.1 Context and objective

Intracranial aneurysm (IA) disease is the most common fatal predisposition amongst young populations with 6-7 cases estimated out of 100,000 per year and a prevalence between 2-6%¹. To date, the understanding of aneurysm disease is still limited, whilst the development of new innovative endovascular techniques allow for the treatment of increasingly complex and/or giant aneurysms. Most of the work on IAs are based on limited and uninformative clinical observations an/or numerical simulation techniques. The latters require reliable physiological boundary conditions which are difficult to have in clinical routine. What is more, they focus almost exclusively on the intra saccular mechanical phenomena².

However, a simple observation in clinical practice during cerebral angiography performed for exploring intracranial giant aneurysms suggests that an aneurysm changes the flow conditions in the parent vessel. Indeed, the cerebral angiographies in patients with giant aneurysms show stagnation of the contrast agent within the aneurysmal sac, followed by a slow opacification of the arterial segment of the parent artery downstream to the malformation. Similarly, the downstream arterial bed shows a significant and observable circulatory slowdown. These qualitative observations are corroborated by the time of flight MRI images (TOF MRI) that show a quantifiable decrease of the signal within the aneurysmal sac and within the parent artery downstream to the malformation. Figure 1 illustrates this phenomenon by comparing cerebral arteriography images of a patient with a giant aneurysm before and after treatment by flow diversion technique and TOF MRI images of a normal internal carotid artery (ICA) and an ICA presenting a giant aneurysm. Despite these visible circulatory changes, the majority of patients with these giant aneurysms have very little or no symptomatic ischemic suffering in the cerebral territory downstream to the aneurysm, certainly due to a progressive and effective cerebral autoregulation. In this context, a rigorous *in vitro* experimental approach that can drive *in vivo* investigations in the patient and take into account the aneurysm and parent vessel as a whole seem to us an important step for moving forward in the understanding of this disease.

The main goal of our work was to characterize the effect of the IA on the flow conditions within the parent artery that might have also had an impact on the brain circulatory slowdown visible downstream to the aneurysm. The characterization of this effect might be of interest for the understanding of the aneurysmal disease and the hemodynamic effect of the endovascular treatment (EVT) on the parent vessel and the downstream arterial bed.

Therefore, the main goals of this thesis work were the following:

1. To evaluate the impact of IA on the hemodynamic conditions within the parent artery.
2. To assess the effect of endovascular flow diversion treatment on the hemodynamic changes within the parent artery induced by IAs.
3. To characterize a new and original phase-contrast MRI (PC-MRI) segmentation tool based on a Fourier Transform analysis of the flow MRI images.

Unlike previous works focusing on the aneurysm disease and the associated hemodynamic changes, this work will distinguish itself by two new approaches. It examines the impact of the aneurysm on the hemodynamic conditions within the parent artery. It is not limited to the intraaneurysmal changes that are commonly reported in literature. It is based solely on quantified data (not simulated) from *in vitro* experimental measurements on a cardiovascular simulator to the *in vivo* PC-MRI flow measurements in patients followed and treated for IAs.

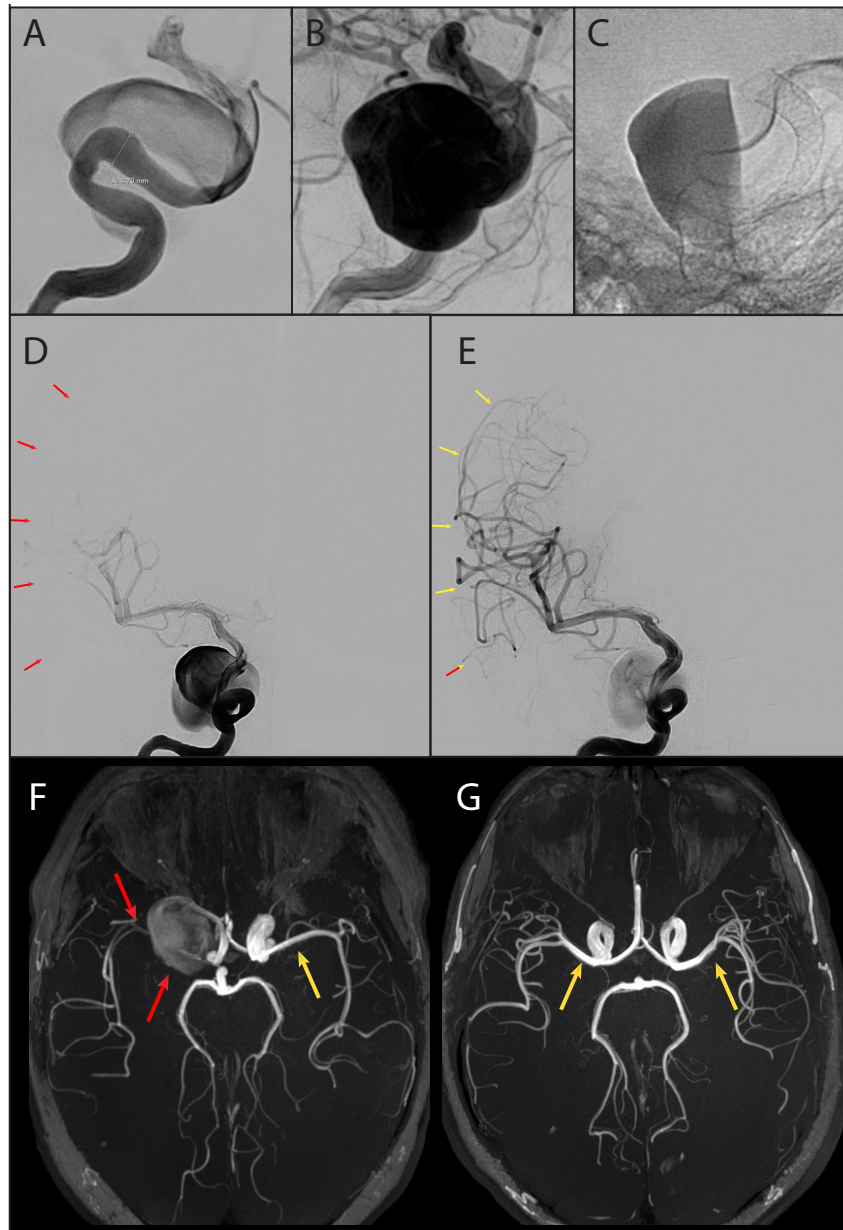


Figure 1 : Slowing flow downstream to a giant aneurysm. Examples of DSA and TOF MRI images.

Images A, B and C shows the magnified digital angiographic images of a giant intracavernous aneurysm of the right ACI before the FDS deployment (A and B) The stagnating contrast media within the large aneurysm sac is easily visible dense. The non-subtracted image (C) shows the deployed FDS and stagnating contrast media within the sac. The images D and E shows the circulation downstream to the aneurysm at the same acquisition time before (D) and after the FDS deployment. Before the treatment (D) the downstream vascular bed is slowly opacified (red small arrows) and associated to the distribution and the stagnation of the contrast media within the aneurysm sac. After the treatment (E), the opacification of the downstream is visible earlier (yellow small arrows). The TOF MRI of a patient followed for a right ICA giant aneurysm (F) shows a decreased TOF signal in the ICA segment downstream to the aneurysm and in the middle cerebral artery (red

arrows) compared to the normal signal in the contralateral middle cerebral artery or in the intracranial ICAs and middle cerebral arteries in a healthy volunteer (G) (yellow arrows).

This work was conducted under the direction of Dr. Guy Courbebaisse (CNRS UMR 5220 - INSERM U1044 - University Lyon 1 - INSA Lyon, France) and Prof. Vincent Costalat (University Hospital of Montpellier, France). It was initiated in the framework of the European THROMBUS-VPH project (<http://www.thrombus-vph.eu>). The *in vitro* experimental part of the work was conducted in the Laboratory of Experimental Medicine of the Vésale Hospital of Charleroi (Belgium) under the direction of Dr. Karim Zouaoui Boudjeltia, and with the collaboration of Dr. Kamil Chodzynski. The *in vivo* PC-MRI measurements study was conducted in the department of interventional neuroradiology of Gui de Chauliac Hospital in Montpellier (France).

1.2 Contributions

This work provides two main contributions.

The first contribution is an improvement in the understanding of aneurysm disease. In particular, several aspects of the impact of IA on the parent vessel's hemodynamic have been clarified. This impact is essentially characterized by a decrease in the resistance and the pulsatility of the parent vessel segment downstream to the aneurysm, which presents a measurable demodulation of blood flow. The decrease of the circulatory resistance associated with IAs was observed *in vitro* using a patient-specific IA silicone model within a cardiovascular simulator reproducing physiological flow conditions. Pressure measurements upstream and downstream to the aneurysm were performed before and after the deployment of a flow diverter stent (FDS) in the parent vessel model and the resistances were calculated. *In vivo*, this effect was confirmed by measuring the velocities in the parent artery upstream and downstream to the aneurysm with 2D PC-MRI technique. Volumetric flow rates (VFRs) were calculated within a group of patients treated for IAs by FDS. A control group of healthy subjects underwent the same 2D PC-MRI examinations and measurements. The comparative analysis of the VFRs in both groups showed decreased resistive and pulsatility indexes (RI and PI) in the parent vessel segment downstream to the aneurysm. This impact of the aneurysm on the parent vessel hemodynamic was inversely correlated to the aneurysm's volumes. The treatment of the aneurysms by FDS allowed for the correction of the hemodynamic disturbances within the parent vessel. The corrective effect of the FDS was quantified by 2D PC-MRI and was stable over time. The FDS allowed a "hemodynamical reconstruction" of the parent artery by increasing the RI and PI, and also by restoring an almost normally modulated blood flow within the parent artery segment downstream to the aneurysm.

The second contribution of this work is the proposal of a new automated method for 2D PC-MRI segmentation for the delimitation of internal carotid arteries (ICA). This segmentation method was based on an automatic Fourier transform (FT) analysis of the phase image (on each voxel) to differentiate vascular flow signals (arterial) from background noise. This work allowed the validation of this innovative approach by comparing it to two reference methods widely used in medical imaging: manual segmentation (MM) and a segmentation based on active contours method according to the Chan-Vese model (ACM-CV). An agreement analysis of the three segmentation methods (two by two) was performed. ACM-CV based segmentation was used for the semi-automatic and quantitative extraction of velocity and VFR curves of the ICA in the patient and control groups studied in this work.

1.3 Chapters

This manuscript is composed of six chapters including the introduction.

The first chapter (above) introduces and presents the contribution of our work.

The second chapter defines the problem that we have attempted to answer through this work. It consists of a "state of art" addressing the different topics and tools used in this research. Therefore, this chapter deals with the epidemiological context of IAs, clinical issues of complex and giant intracranial aneurysms and their specific treatment, such as the endovascular flow diversion technique. This latter technique for the treatment of such complex aneurysms was especially addressed. A review of studies on the hemodynamic disturbances associated with IAs is reported as well as the different methods of exploration of these changes. Non-invasive techniques for measuring *in vivo* blood flow are described with their advantages and disadvantages. This chapter ends with a non-exhaustive review of image segmentation methods. The peculiarities of the ICA with regards to its 2D PC-MRI segmentation and its specificities and constraints are also described.

The third chapter presents an *in vitro* exploration of the aneurysm's impact on the flow conditions within the parent vessel. The experimental part of this work was conducted using an *in silico* patient-specific IA model integrated within a cardiovascular simulator recreating physiological flow conditions. The principles and characteristics of the simulator, the input data, the measurements and the calculations of the flow parameters in the hydraulic circuit have been described. Experiments with the simulator and its results are presented and discussed.

The fourth chapter presents the *in vivo* exploration and validation of the previously described results observed in the conducted *in vitro* study. A group of patients followed and treated for unruptured intracranial aneurysms (UIA) were imaged and compared to a control group of healthy volunteers. The UIA were treated with FDS. All patients underwent blood flow measurements of the parent vessel (i.e., ICA) with 2D PC-MRI, at specific locations upstream and downstream to the aneurysm, before and after the EVT. The healthy volunteers underwent blood flow measurements in similar conditions and at similar locations on the ICA. The VFR curves were analyzed in both groups and compared. Based on those curves, resistive and pulsatility indexes were calculated. The results of these analyses are presented and discussed.

The fifth chapter presents a new method for the segmentation of the vascular structures on 2D PC-MRI images based on a FT analysis of the phase image. In a group of healthy volunteers, the cervical or intracranial ICAs were also imaged with 2D PC-MRI technique at similar locations. The arteries were segmented with this original technique. The results of the segmentation, in terms of vessel areas, mean velocities and mean VFR, were analyzed. These results were compared to the results of the segmentation obtained by other techniques: the manual method (MM) and the active contour method proposed by Chan-Vese (ACM-CV). An agreement analysis by achieving Bland-Altman graphs and the concordance correlation coefficient computation was performed. The results of the segmentations and the correlation analyses between the three methods are presented and discussed.

The sixth and final chapter summarizes the main findings of this thesis in a brief summary. We discussed and analyzed these results in light of existing literature and compare them to previously reported works. We try to clarify the choices and methodological orientations taken in this investigation work while specifying their limits. Finally, we discussed the prospects and future avenues of research on the topic. Particularly, we presented two research projects that have emerged from this work and which are ongoing in the department of interventional neuroradiology Gui de Chauliac Hospital in Montpellier (France).

CHAPTER 2

2 State of the art

2.1 Epidemiology of intracranial aneurysms

An IA is a saccular dilatation, or more rarely a fusiform, of a cerebral artery at risk of rupture and hence of intracranial bleeding (subarachnoid hemorrhage and/or intra parenchymal). Amongst younger populations, intracranial aneurysmal disease represents the most prevalent predisposition to a fatal risk with an estimated incidence of 5-7 cases per 100,000 persons per year and a prevalence between 2-6%³⁻⁵. It is the leading cause of hemorrhagic stroke and is responsible for a reduction in life expectancy and a potentially severe disabilities affecting quality of life. Six thousand intracranial hemorrhages secondary to ruptured IAs occur in France each year. The mortality rate associated with subarachnoid hemorrhage secondary to ruptured intracranial aneurysm (AIR) is estimated at 45% - 50% at 30 days⁶. The associated morbidity is estimated at 25-30%, with a dependence in nearly 30% of patients at 1 year despite appropriate and early treatment⁷. The UIA risk of rupture is difficult to estimate and varies between 0.4% and 17.8% at 5 years. This risk is increased by the following factors: age, gender, hypertension, smoking, aneurysm size and location in posterior circulation⁵. Finally, the aneurysmal rupture and its complications have a significant economic impact in terms of costs related to the management of the acute phase, the neurological deficits and / or subsequent dependence^{5,7,8}.

2.2 Treatment of intracranial aneurysms

The value and benefits of treating AIR by endovascular or surgical approaches allowing its exclusion from blood circulation have already been demonstrated^{7,9-11}. Many studies have also reported the benefits of the primary prevention treatment of UIA¹². Endovascular treatment consists in the aneurysm exclusion by filling it with a thrombogenic material, a coil, with or without balloon or stent-assistance. With surgery, treatment consists in clipping the aneurysm at its neck. These treatments have helped to reduce the morbidity and mortality rates associated to this disease and to increase the patient's survival significantly over the past two decades. Since the International Subarachnoid Aneurysm Trial results (ISAT)¹³, the EVT has become the first option for IAs, ruptured or not, when the two therapeutic possibilities are equivalent in terms of results after discussion in a multidisciplinary team^{14,15}. Indeed, EVT has reduced the morbidity and mortality rates associated to this disease and increased survival and also significantly increased the quality of life^{4,7,10,11,16}.

2.3 The issue of giant intracranial aneurysms

Giant aneurysms, defined by having a diameter higher than ≥ 25 mm (with large neck or not) are complex aneurysms that still remain a challenge to manage, despite the improvement and the development of endovascular techniques.

The estimated prevalence of these aneurysms is around 5-6% of all cerebral aneurysms. They typically present during the 5th to 7th decade with a slight female preponderance. Giant aneurysms are generally classified as : (1) saccular type, resulting from gradual growth from small berry aneurysm ; (2) fusiform type, progression from angioectasia due to atherosclerosis and/or connective tissue disorder ; and (3) serpentine type, (the less common) probably from thrombosis and recanalisation of fusiform aneurysms or possibly from saccular aneurysms. They occur at the same locations as the smaller aneurysms (2/3 in the anterior circulation and 1/3 in the posterior circulation). In the anterior circulation they present a predilection for the cavernous and proximal intracranial carotid arteries ¹⁷, among which the cavernous and ophthalmic aneurysms are the more frequent. In the posterior circulation 70% of them are located near the basilar tip and P1 segments of the posterior cerebral artery or the superior cerebellar artery ¹⁸. The fusiform giant aneurysm at mid basilar, vertebro-basilar junction and posterior inferior cerebellar artery locations are less common.

Their natural evolution is usually unfavorable, enameled by hemorrhagic complications with a rupture rate higher than that of smaller aneurysms and estimated between 20 and 70% according to reported series, ischemic manifestations seen in around 4% of giant aneurysms, and/or the consequences of compression phenomena on brain parenchyma or cranial nerves (cavernous sinus syndrome) ^{19,20}. Presumably, the ischemic symptoms occur secondary to distal thromboembolism from thrombi within the sac ¹⁹. Untreated giant aneurysms present a higher mortality rate of 68% at 2 years and 80% at 5 years ²¹. And some series showed a 100% mortality rate at 2 years in untreated patients ²². Subarachnoid haemorrhage has been found to be the most common cause of death with giant aneurysms when managed conservatively ²².

2.4 Flow diversion technique for the treatment of intracranial aneurysms

The treatment of these giant aneurysms still remains a challenge for neuroradiologists and neurosurgeons. Currently, the management of these technically more difficult to treat aneurysms is either endovascular, microsurgical or conservative in approximately 50 to 55%, 35-40% and in 10% of cases, respectively ¹³. Conservative management concerns mostly older patients. The recourse to the historical parent artery occlusion is less frequent since the considerable advances in endovascular and microsurgical techniques. Although parent vessel occlusion may provide a durable treatment, it presents strict inclusion criteria and patients may still be at high risk of ischemia after the treatment (between 4 to 15%) ^{23,24}. The occlusion test itself carries some risks of ischemic events secondary to embolic events between 0.4 and 1.6% ²⁵.

Since the ISAT trial, aneurysm management has changed considerably in terms of the treatment of these challenging malformations ^{12,14}. The development of intracranial coiling and stenting techniques (with balloon or stent assisted remodeling techniques), and especially the advent of FDS, have appeared as efficient and valid alternative techniques that allow for the parent artery preservation. They have considerably increased the resolution of these

complex aneurysms despite some limits of the long term results¹³. Indeed, the EVT of large and giant aneurysms with parent artery preservation is associated with high rates of recurrence, ranging from 37.5 % to 90 %²⁶⁻²⁸. Although the stent assisted-coiling technique improves the durability of treatment, recurrence rates remain also high, at 20–57 %^{29,30}. Moreover, the treatment of these aneurysms exposes the patients to a high risk of neurological deterioration in up to 50% of the patients whatever the therapeutic strategy (endovascular, microsurgical or conservative). The risk is higher for the patients presenting with SAH (up to 58%) than for patients presenting with pseudo tumoral or ischemic symptoms^{13,22,26}. The deterioration is marked by cerebral ischemia due to large vessel or perforator occlusions.

In the search for better treatment options, recently, the flow diversion technique has emerged as a new strategy for direct reconstruction of the parent artery and the treatment of large sized and complex aneurysms. It consists in the deployment of a reduced permeability stent, the FDS allowing for the blood flow to reroute in the parent vessel. This technique relies on the ability of FDS to redirect the blood flow out of the aneurysmal sac, allowing the reduction of the intra-aneurysmal blood flow and hence promoting the thrombosis of the aneurysmal sac and its regression³¹. As mentioned above, several studies have reported the value and effectiveness of this technique in the treatment of previously difficult to treat aneurysms, such as giant aneurysms^{31,32}. Compared to the conventional techniques (coiling, stent-assisted coiling or parent vessel occlusion), the FDS for the treatment of giant aneurysms presents a higher rate of occlusion, a lower rate of recurrence without increasing the rate of complications^{28,33,34}.

The flow diversion technique has also several limitations. In particular, an incomplete aneurysm occlusion rate is reported and still unexplained. Recent meta-analyses on the results of this technique reported an average rate of complete occlusion of 76% at 6 months (1451 patients / 1654 aneurysms between 2005 and 2012), of 76.2% at 9 months (897 patients / 1018 aneurysms between 2008 and 2012) respectively³⁵⁻³⁷. In an earlier meta-analysis, D'Urso et al reported an occlusion rate changing over time and estimated between 8% and 21% immediately after the treatment, 69% at 6 months and greater than 90% at 1 year³⁸. The permanent morbidity and mortality rates associated with this method are not negligible, around 10% and 5% at 6 months, respectively^{36,39}. Reported complications are essentially intracranial bleeding promoted by the antiplatelet therapy necessary to maintain the parent vessel and the FDS patency artery (4% HSA, 3% intraparenchymal hematoma), and ischemic lesions responsible for permanent neurological deficits (6% of ischemic strokes)^{36,39}. Some authors have suggested the use of FDS with additional coiling of the aneurysm to reduce the risk of post-diversion flow bleeding. But, this option is still subject to debate.

2.5 Its Hemodynamics in the intracranial aneurysms

Hemodynamic factors are considered to play a crucial role in the progression and the rupture of IA, as well as in the effectiveness of their EVT treatment^{2,40-42}.

The commonly accepted goal of the IA treatment is its exclusion from the blood circulation, the morphological reconstruction of the parent vessel and the correction of the hemodynamic disturbances in both the aneurysmal sac and the parent vessel. While new generations of endovascular devices acting on the hemodynamics of both the parent vessel and the aneurysm sac are proposed or in development, such as FDS^{32,35} or intrasaccular flow disruption devices (WEB device), the hemodynamic disturbances within the parent vessel induced by the

aneurysms are little known and investigated. Similarly, the changes induced by the FDS in the aneurysmal sac have been the subject of many studies. But the effect of the FDS on the parent vessel hemodynamics are poorly described in the literature ⁴³⁻⁴⁵.

The development of numerical simulation (computational fluid dynamic methods, CFD methods) based on patient-specific medical imaging has improved our understanding of the interaction mechanisms between the blood flow hemodynamics and the arterial wall, as well as the initiation and development of vascular diseases, such as aneurysm disease. These techniques have also helped us to understand better the changes in flow induced by certain endovascular devices (coils, stents and FDS) ^{2,41,46,47}. They have helped to increase our understanding of the natural history of IAs, and hence develop and improve the therapeutic options we offer the patients. Thus, it is now generally accepted that hemodynamic parameters, such as input flow into the aneurysmal sac, the impact zone of the latter on the aneurysmal wall, and the shear stress on the wall, contribute to the growth and rupture of IAs.

The CFD methods applied to IA disease allow for the prediction of local hemodynamic in a certain extent (e.g., in the aneurysmal sac) ^{32,42}. These numerical simulation methods are based on the calculation of the flow profiles by using a set of fundamental partial differential equations that describe the flow profiles ^{47,48}. The description into the detail of these differential equations is beyond the scope of this work. Nevertheless, it is useful to specify that these equations are based on three key principles: the principle of conservation of mass, the principle of conservation of momentum and the energy conservation law within the fluid. Given the complexity of the equations to be solved, iterations are performed to converge to a solution describing as closely as possible the characteristics of the fluid, with specific flow parameters, among which are the velocity, temperature and pressure values. These methods require significant computing resources to achieve and can solve thousands of calculations with significant levels of accuracy. These constraints have mainly contributed to limiting the spread and use of these tools in clinical practice.

These methods and their results have two main limitations. 1) They require prior knowledge of information and parameters on the fluid characteristics (hemodynamic boundary conditions) often difficult to measure *in vivo* (velocity, pressure, flow, viscosity conditions, etc, distribution of wall thickness, wall elasticity, and intra-arterial pressure waveform, etc.) ⁴⁶. To overcome this limit, approximations on these input parameters are performed limiting the precision and reliability of the results. However, the accuracy of these input parameters, especially the patient-specific velocity values, are essential for the correct calculation of the simulated flow characteristics. For instance, local shear constraints at the aneurysmal wall (wall shear stress as well as wall shear rate) are calculated with blood flow velocities taken in the parent vessel. A change in the amplitude of the blood flow velocities inevitably affects the amplitude of the calculated wall shear rates or wall shear stresses. Previously published work showed variations of wall shear stress with up to 25% secondary to changes (even small) of the measured flow profiles. These results underscore the importance of using reliable and accurate patient-specific input data for calculations in numerical simulations ^{47,49}. Therefore, although these approaches are interesting in a research perspective, they are not easily implementable and readily usable in clinical practice. 2) The use of these techniques focuses primarily on the intra-aneurysmal flow changes. Therefore, they neglect (and if not, at least underestimate) the impact of the aneurysms on the parent artery hemodynamic, and more importantly on the intracranial hemodynamic.

2.6 Methods for *in vivo* measurements of arterial velocities and flow rates

As noted above, the use of reliable input data (hemodynamic boundary conditions, patient-specific velocities, etc.) is crucial for the calculations and the relevance of results in numerical simulation. To date, the only two imaging techniques that allow us to explore and quantify, the hemodynamic parameters of blood flow in arteries non-invasively are the Doppler ultrasound and PC-MRI techniques.

2.7 Doppler ultrasounds technique

2.7.1 Principle of Doppler ultrasounds

When an ultrasound beam is emitted by a source through an environment (biological tissue, for example), it meets a number of interfaces, or targets, which reflect the beam to the source. Measurement of blood flow velocities with Doppler imaging is based on the frequency shift (or phase shift) of the reflected ultrasonic beam by moving targets⁵⁰. Indeed, the frequency reflected from the interfaces is variable depending on whether they are fixed or moving. The frequency reflected from stationary targets is identical to the transmitted frequency: there is no difference between the transmission frequency (F_0) and the reception frequency (F_r), namely:

$$F_r = F_0 \quad \text{Equation 1}$$

If the target moves, the frequency of the reflected beam is changed according to the following relationship:

$$F_r = F_0 + \Delta F \quad \text{Equation 2}$$

where ΔF is the difference in frequency (frequency shift) or Doppler frequency (see Figure 2). ΔF is a function of the target's velocity and direction according to the relationship:

$$\Delta F = 2V \cdot F_0 \cdot \cos\theta / c \quad \text{Equation 3}$$

Where V is the velocity of the target (in ms^{-1}), θ is the incidence angle in degrees of the ultrasonic beam to the moving direction, c is the ultrasonic propagation velocity in the biological tissue (constant = 1540 ms^{-1}). In vascular exploration, ΔF varie between 50 Hz and 20 KHz⁵⁰.

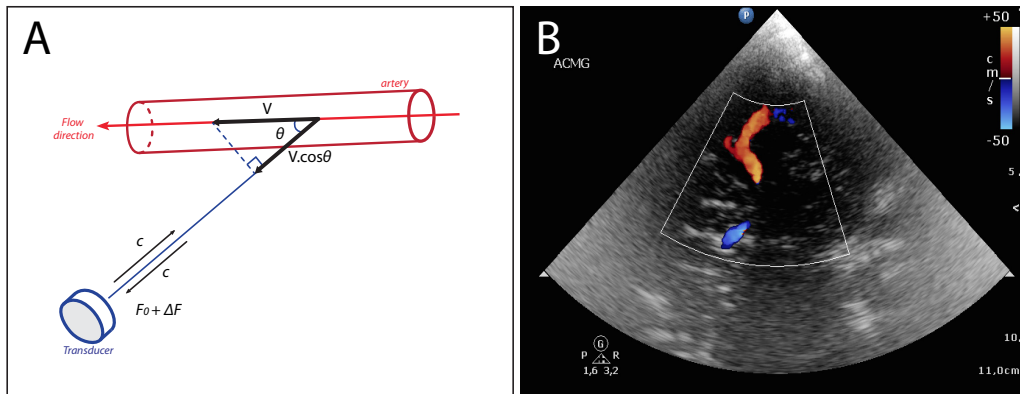


Figure 2 : The Principle of the Doppler ultrasounds.

The image A shows the principle of the Doppler ultrasounds, where V is the velocity of the target (in ms^{-1}), θ is the incidence angle in degrees of the ultrasonic beam to the moving direction, c is the ultrasonic propagation velocity in the biological tissue (constant = $1540 ms^{-1}$), F_0 is the transmission frequency, F_r is the reception frequency, ΔF is the difference in frequency (frequency shift) or Doppler frequency. Image B illustrates an example of the Doppler signal in color mode of a left middle cerebral artery in a healthy volunteer.

This principle of the ultrasonic waves has been historically used and applied to the measurement of blood velocities within the intracranial arteries. This technique of velocity measurement is still widely used in clinical practice, in intensive care units for example. But many factors limit the use of this method for the evaluation of ICA at its sub petrous or intracranial segments, particularly in the framework of this study. In particular the ICA anatomy characterized by very tortuous segments, the natural barrier to the ultrasound that shows the bony skull and the dependence of the measurements to the incidence angle all limit the accuracy and reliability of this technique⁵¹.

2.7.2 Endovascular application of Doppler ultrasounds

Recently, some authors have put forward an adaptation of this technique for endovascular velocity measurements in the coronary arteries and intracranial arteries. A specific probe adapted for endovascular navigation and carrying a Doppler velocity sensor and a pressure sensor was used (ComboWire, Volcano Corporation, Rancho Cordova, California ; (<http://www.volcanocorp.com>; see Figure 3). This technique has the advantage of measuring simultaneously the blood flow velocities and pressures. It has been validated for the assessment of coronary stenosis during interventional cardiovascular procedures^{52,53}. Measurements by this device have also been achieved in the intracranial ICA during EVT of IAs, even in patients with ruptured aneurysms. The measurements allow for the obtainment of patient-specific hemodynamic boundary conditions as an input for numerical simulation models. Although appealing, this approach has a number of limitations making it unattractive to the purpose of this study which aims to use and set up a non-invasive methodology usable in clinical practice. Indeed, this invasive approach provides velocities, flow rates and pressures measurements usable only in a retrospective purpose which limits its use to a prospective end. As part of the aneurysmal disease, the measurements could reasonably be conceivable only under general anesthesia given the size of the device (0.014 inch guide catheter and 0.021 inch) and its rigidity that might increase the duration of catheterization in tortuous arteries such as the intracranial ICA. But, sedation induced by general anesthesia results in a reduction in average of arterial blood pressures and velocities. This results in an

underestimation of these parameters. Furthermore, the technique is dependent on the angle of incidence due to technical and design constraints (small size sensors at the end of a microwire). Thus, the location of the endovascular device in the lumen of the target arterial segment may affect the accuracy and the reliability of the measurements, especially in very tortuous arterial segments, such as the carotid siphon⁵⁴. Sometimes, the latter limit requires the surgeon to maneuver until a significant systolic-diastolic signal is obtained, thus increasing the invasiveness of the technique and procedure related risk of complications. The size of the device compared to the size of the explored reduced arterial lumens, such as in the intracranial ICA (diameter varying between 3 to 5 mm), may also induce an obstruction and hence flow disturbance that might impact the accuracy of the measurements. Finally, an over- or underestimation of velocities is theoretically possible. It is due to the smoothing of velocity curves induced by the signal post-processing⁵⁴. All of these characteristics severely limit the usefulness of this approach for obtaining the measurements of flow rates and pressures in the framework of this study.

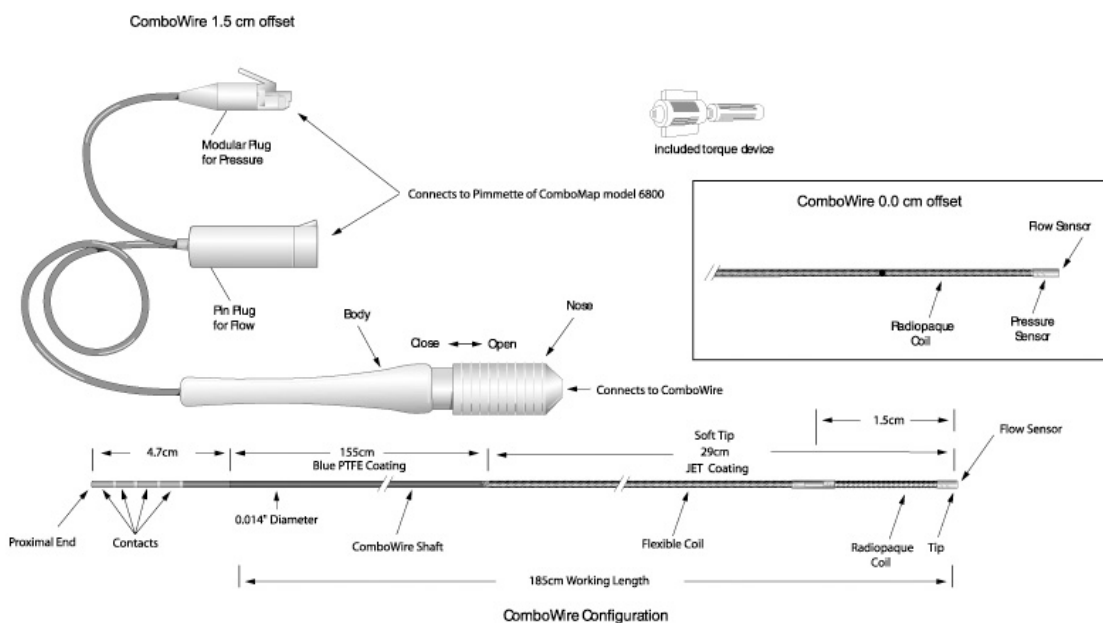


Figure 3: The application of the Doppler ultrasounds to endovascular exploration

The ComboWire[®] device consists of a flow sensor and a pressure sensor located at the tip of the distal end of the device. The device has a length of 184.7cm and a diameter of 0.014 inch. The signal recorded by the probes (velocities and pressures) are illustrated in image B. The pictures come from the website of the Volcano Corporation (<http://www.volcanocorp.com>).

2.8 Phase-contrast MRI technique

Phase contrast MRI (PC-MRI) provides high resolution images with both anatomical and functional information. It is not limited by the anatomy and can access all the anatomical regions in all directions. This approach allows for the measurement of a wide range of velocities and blood flow patterns during a cardiac cycle. This non-invasive and non-irradiating technique is considered accurate and reliable for quantification of velocity in the cervical and intracranial vessels in various cerebrovascular pathologic conditions⁵⁵⁻⁵⁸. It is

highly correlated with the Laser Doppler velocimetry (regarded as the reference method for *in vitro* flow measurements) and the endovascular Doppler technique for quantifying flow rates, particularly in large arteries, such as in the ICA⁵⁹⁻⁶¹.

The description and details of the principles of MRI is beyond the scope of this thesis. Only the principle of PC-MRI will be detailed in this chapter. We instead refer the reader to the following references to read about MRI techniques^{62,63}.

2.8.1 Principle of phase-contrast MRI

PC-MRI technique derives from the contrast between flowing blood and stationary tissues by manipulating the phase of the magnetization, such that the phase of the magnetization from the stationary spins is zero and the phase of the magnetization from the moving spins is non-zero at the signal reception. The phase measures the magnetization process from the time it is tipped into the transverse plane until the time it is detected. The data acquired with phase contrast techniques can be processed to produce phase differences, complex differences and magnitude images⁶³. In detail, the principle of PC-MRI is based on the phase shift in the transverse magnetization generated by mobile protons (or spins) subjected to a bipolar gradient. Two measurements of the phase shift after applying two inverted bipolar gradients are performed (consecutive negative and positive lobe for the first measurement and consecutive positive and negative lobe for the second measurement). PC-MRI is based on the subtraction of these two acquired measurements^{63,64}. Indeed, for a given bipolar gradient with given intensity and duration, the phase shift of mobile spins is related to their position within the vessel and therefore to their velocity. The gradient is oriented parallel to the vessel of interest. During the first acquisition, mobile and stationary spins undergo a first phase shift (phase shift 1, ϕ_1) according to their velocities (null for stationary spins and different from zero for the mobile spins). During the second acquisition after inversion of the lobes of the encoding gradient, the moving spins have a second phase shift (phase shift 2, ϕ_2), while the stationary spins have the same phase shift due to the heterogeneity of the field, but in the opposite direction. At the acquisition, stationary spins therefore have undergone an opposite phase shift of the same amplitude, so an overall null phase shift. While moving spins have undergone a phase shift corresponding to the sum of ϕ_1 and ϕ_2 which are in the opposite direction but with different amplitudes due to the movement of the spins, resulting in a total phase shift $\Delta\phi$, as illustrated in Figure 4. Stationary tissues are eliminated while mobile protons are enhanced. The faster the mobile protons move, the more intense their signal is.

The mobile protons have constant velocities within the explored vessel segment. The overall phase shifts $\Delta\phi$ are therefore proportional (and linearly) to their velocities. This MRI technique allows to quantify the relative velocities, flow rates and directions of flow in the arteries, veins and the cerebrospinal fluid (CSF) through the phase information, specifically the overall phase shift $\Delta\phi$. High resolution images can be achieved (up to 0.3 mm to 0.3 mm for the sequence used in this work). PC-MRI in a plane perpendicular to the direction of flow provides the velocity values in the direction through this plane for each voxel of the image at multiple time points of the cardiac cycle.

In 2D PC-MRI, the resulting images show the studied vessel in the acquisition plan, as illustrated in Figure 5. In 3D exploration, the movement of the mobile spin in the three directions of space is analyzed by repeating the acquisitions in all three spatial directions. An additional acquisition without a flow encoding gradient is used as a reference. The MRI sequences used for this technique are gradient echo sequence.

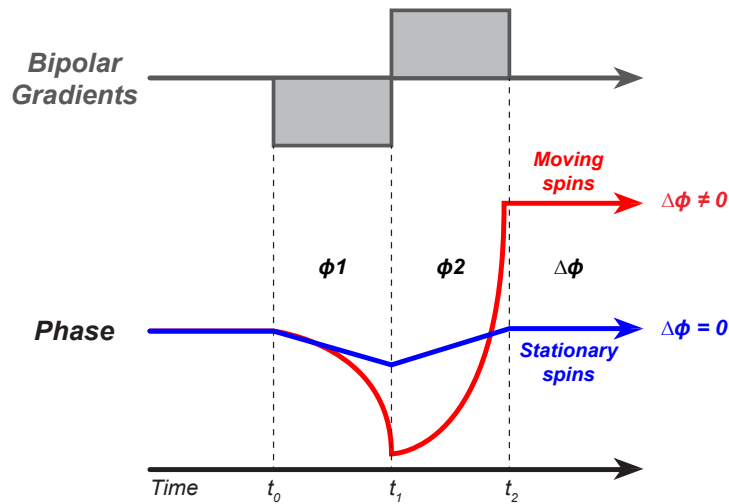


Figure 4: The Principle of the Phase-contrast MRI

This diagram shows the use of a bipolar magnetic field gradient applied in the direction of blood flow (and therefore perpendicular to the studied vascular section) at two instants t_1 and t_2 . The application of the negative part of the bipolar gradient introduces a phase shift (ϕ_1) of the spins in the direction of the gradient at time t_1 . The application of the positive part of the bipolar gradient (of the same amplitude and duration as the negative part) implies at time t_2 a phase shift (ϕ_2) of the spins in the opposite direction to that introduced by the first part of the bipolar gradient. Following the sequence acquisition, the spins of the stationary tissues exhibit a zero phase difference since $\Delta\phi = \phi_1 + \phi_2 = \phi_1 - \phi_1 = 0$. In contrast, mobile spins exhibit a phase shift according to their velocity defined by their starting and ending positions relative to the acquisition plane during the time of application of the bipolar gradient (since $\phi_1 \neq \phi_2$, $\Delta\phi = \phi_1 + \phi_2 \neq 0$).

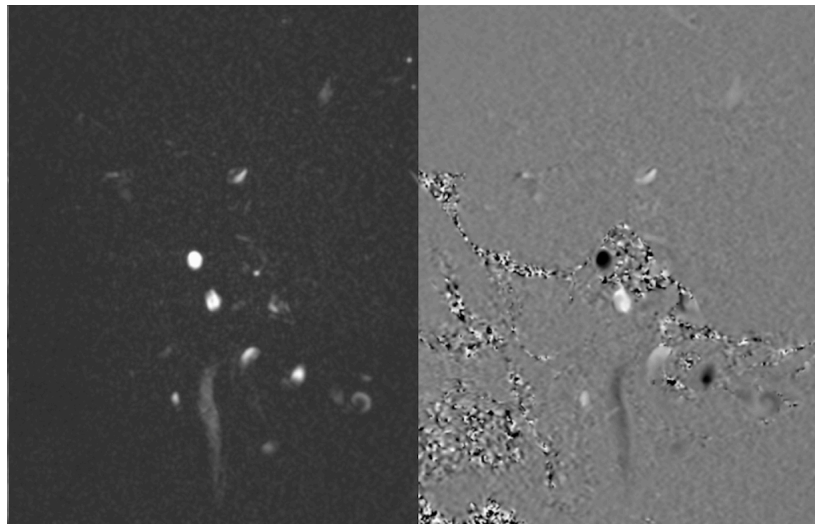


Figure 5: Illustration of 2D PC-MRI of intrapetrous ICA

This Figure shows the different images provided by the 2D PC-MRI including the image of magnitude (right picture) and the image of phase (left picture). The intra petrous segment of the ICA is visible in white on the amplitude image and black on the phase image because of the flow direction which is at the opposite of us.

The measured global phase shift $\Delta\phi$ is proportional to the velocity of the spin in the vessel within the limits of an angle of 2π , in other words $\pm\pi$ (from $-\pi$ to $+\pi$). Thus, when the offset is greater than 2π , a phase jump or aliasing can be observed. This type of artifact results from the improper use of gradients with respect to the measured velocities (usually low gradient compared to the expected velocities). The gradient adjustment avoids this artifact. This presupposes a prior knowledge of the magnitude of the maximum velocity explored and preselects a velocity scale to optimize the signal to noise ratio (S/R) and improve the sensitivity of the technique.

2.8.2 Velocity encoding in phase-contrast MRI

The principle of preselecting velocities is to define the phase shift caused by a velocity unit. Thus, we define the encoded maximum velocity V_{enc} which limits these artifacts while maintaining a good momentum of the measurements. Indeed, a high set V_{enc} compared to slow velocities in the studied vessel will result in very low phase shift (for short distance traveled) and therefore in a dynamic loss and a weak signal. Conversely, a low set V_{enc} compared to high velocities in the studied vessel will induce important phase shift (greater than π) and therefore a phase jump or aliasing artefact over time. (Aliasing artifact corresponds to voxels having a sharp signal intensity change compared to their nearest neighbors which do not have it). In the latter case, a correction of the measured velocities can be possible to some extent by using unfolding algorithms applied to the velocity spectra over time. For each voxel, the velocity v (in $\text{m}\cdot\text{s}^{-1}$) can be extracted according to the following formula defining the observed phase shift:

$$v = (\Delta\phi/\pi) * V_{enc} \quad \text{Equation 4}$$

Thus, the flow rate (in $\text{mL}\cdot\text{min}^{-1}$ or in $\text{m}^3\cdot\text{s}^{-1}$) through each voxel is obtained by multiplying the velocity of the voxel by its area. Therefore the average flow rate through the vessel section studied is obtained by multiplying the mean velocity through the vessel section by its the area.

PC-MRI provides paired images of amplitudes and phases over a cardiac cycle. The image amplitude is a traditional gradient echo image and the phase image is a parametric image of the phase shifts of the spins in a selected acquisition plane. The flow going towards the observer and away from him are coded in white and black, respectively (Figure 5).

2.8.3 ECG Synchronization

All the images could not be acquired during a single heart cycle. Repeated acquisition for each phase of the cardiac cycle is needed to observe the evolution of velocities over time. The PC-MRI is thus performed on several cardiac cycles. The images are acquired at different times therein. Therefore, this technique is synchronized to the heartbeat with an electrocardiogram (ECG) signal to acquire a series of images during a cardiac cycle as illustrated in Figure 6. This synchronization can be prospective or retrospective. Each synchronization approach has its advantages and disadvantages. The choice of synchronization depends on the purpose of the study.

The prospective synchronization method is triggered by the detection of the R wave on the ECG signal, which is the first positive component of the QRS complex (complex which

corresponds to the depolarization and contraction of the ventricles, right and left). It is the easiest to identify because it has the largest amplitude ⁶³. This type of synchronization requires the definition by the operator of an R-R time interval that can be done manually or automatically before the acquisition. This interval is in practice always shorter than the actual RR interval (corresponding to about 90% of it) in order to avoid any possible overlaps of two consecutive cardiac cycles (due to a change in heart rate during acquisition, for example). When the R wave is detected, acquisition is started until the obtainment of all the phases of the cardiac cycle. The advantages of this gating method are multiple. This approach to synchronization limits the time of acquisition because it avoids missing any heart cycles. It is a robust technique that limits the artefacts caused by cardiac arrhythmias. This latter can be ignored or attenuated with this method. Indeed, the acquisition always starts at the same phase of the cardiac cycle, the R wave. In addition, the possibility of assigning non-starting times of acquisitions after detection of R-waves can also help for the attenuation of artifacts related to arrhythmias. However, the main limitation of this gating technique is that it does not cover the entire cardiac cycle, since the end of the cardiac cycle does not get imaged (about 10% of the average cardiac cycle) ⁶³.

The retrospective gating method is an automatic method based on continuous ECG signal recordings associated with the continuous acquisition of the PC-MRI velocimetry (41). The image acquisition and the ECG recording start simultaneously upon the detection of a first R wave. The imaging data and the corresponding ECG signal data are stored. They allow image reconstruction for each phase of the cardiac cycle when the data acquisition ends (see Figure 6). Each phase of the cardiac cycle corresponds to PC-MRI acquisitions, which are averaged to rebuild the corresponding phase contrast image. This synchronization method allows us to generate high quality phase contrast images covering the whole cardiac cycle when the ECG is normal (in the absence of cardiac arrhythmia). However, this method requires more time than the previous acquisitions. Moreover, in the case of arrhythmia or variation of the cardiac cycle during the acquisition (i.e., modification of interval R-R duration), significant artifacts occur limiting the reliability of the measurements. In the latter case, the change in the duration of the R-R interval makes it difficult to match the phase contrast acquisitions phase to the specific phases of the cardiac cycle ⁶³.

As part of this work, we chose to use a prospective cardiac gating method to limit the duration of acquisitions and limit the artifacts associated with possible heart rhythm variations.

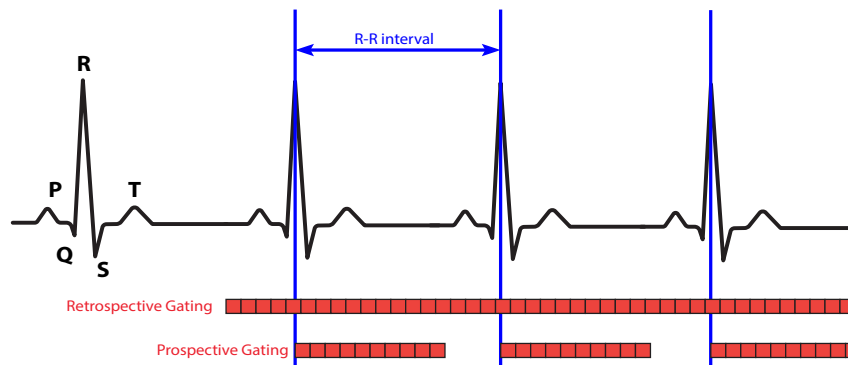


Figure 6 : The Principles of the Phase-contrast MRI ECG synchronization.

This diagram shows the use of the ECG signal with the QRS complexes over time. The red squares correspond to the data acquisition during the 2DPC-MRI sequences : one continuous acquisition with the retrospective gating or multiple acquisitions triggered by the R waves with prospective gating.

2.8.4 2D or 3D acquisitions in phase-contrast MRI

As previously described, the PC-MRI can be achieved in 2D or 3D over time. The technique allows us to obtain 3D anatomical images and 3D phase images in three perpendicular directions. It provides information about the velocity and the direction of the spin movements^{55,63}. The 3D PC-MRI requires repeated acquisitions in all three spatial directions. An additional acquisition without a flow encoding gradient is used as a reference. This approach is less sensitive to flow turbulence for a given blood section and allows for three-dimensional study and reconstructions. However, the repetition of sequences in three planes of space notably extends the acquisition time for significant acquisition volumes. Its use in clinical routines is then limited and this technique is mostly restricted to the field of research⁶⁵. A second drawback associated with this technique is the choice of the optimum V_{enc} compared to the various velocities present in the volume of acquisition. Indeed, a given V_{enc} value can be well suited to measure some velocities in some areas of the acquired volume, while it can cause aliasing artefacts or default contrasts and low signals elsewhere in the acquired volume⁶³. In addition, 3D PC-MRI presents lower spatial and temporal resolutions than the 2D technique at the same magnetic field intensity and for the same acquisition times⁶³. on top of that, an underestimation of velocity measurements at systolic peak can also be seen due to a low pass filter effect related to the post-processing of the signal⁶⁶. These limits, in particular, the long acquisition times which are not very compatible with daily clinical use, have led us to choose the 2D technique for the *in vivo* velocity measurements performed in this work.

2.9 Image segmentation

Segmentation is the process of partitioning a digital image into multiple sets of pixels (or segments) having similar characteristics. It allows, among other things, to extract a specific region of the image named the object of interest (or region of interest, ROI). This process can be applied to both the segmentation of written texts or more complex structures, such as tumors within the brain parenchyma in MRI^{67,68}. It simplifies the understanding of an image

from thousands of pixels to a few regions according to their morphological, signal or functional properties. It is generally the first step in the process of interpretation or use of information in an image. In clinical practice, the precise segmentation of medical images is crucial for the analysis and extraction of the "useful" information necessary for physicians.

As we have previously mentioned, the PC-MRI technique provides anatomical and functional structural information with excellent resolutions in soft tissue, spatially and temporally. It allows the characterization of flows (blood flow or CSF). But the calculation of blood flow parameters, for example, requires the delineation of the cross section of the vascular structure studied in a series of velocity encoded images over time. Many tools for segmentation have been developed to achieve this goal. But, sometimes the complex nature and the small size of the anatomical structures studied with the 2D PC-MRI technique (heterogeneous regions with noise or artifacts) makes the segmentation process difficult. The segmentation of the internal carotid artery (ICA) is an example illustrating precisely these limits (Chapter 2; §2.10).

2.9.1 Manual segmentation method

In the manual segmentation method (MM), the user defines and delineates the contours of the studied object in the image (i.e., a vascular structure in our work) on the sole basis of his judgment and his experience. The MM is the reference method (or “gold standard” method) in various applications, such as the analysis of the heart or aorta (in ventricular volumetric ejection for example). This approach has the advantage of a controlled, accurate and reliable segmentation when applied by an experienced user with expertise on the properties of the studied object, and the limits of imaging technique used (ie, ACI explored with 2D MRI-CP as part of our work). However, this method has many limitations. Processing images one by one is time consuming when it comes to treating large volumes of images ⁶⁹. Since the method implies a good knowledge of the segmented object and a certain experience in the imaging technique used to acquire the image, its reliability and reproducibility are limited in the hands of unexperienced users or new users. The limited size of certain anatomical structures, such as ACI or intracranial arteries, also poses the main problem of the difficult definition of the vessels’ boundaries. In fact, the low velocities at the periphery of the arterial lumen in these small vascular structures (compared to the velocities at similar intraluminal locations within the aorta or in the heart) are associated with a low signal and a low contrast in signal between the vessel lumen and the adjacent soft tissues. What is more, additional blurring artefacts and partial volume effect can also be seen at the boundaries of such vascular structures. All these factors combine to limit the use of the MM for the post-processing of ICA imaged by PC-MRI, and therefore the use of this latter technique in clinical practice. In this context, the value of developing automated methods of segmentation is easily understandable.

2.9.2 Automated segmentation methods

To overcome the previously mentioned limitations of manual segmentation, and in particular to speed up the processing for a large and growing amount of medical images, while maintaining the reproducibility of the segmentation, many automated segmentation algorithms have been proposed. The approaches on which these methods are based are many and varied. They depend on the type of image processed and the purposes of the segmentations and their applications ⁷⁰. Thus many techniques have been put forward based on the principles of : thresholding, histogram analysis, region growing methods known as

split / merge, pattern search, edge detection, surface analysis, etc. An exhaustive state of the art of the segmentation methods is beyond the scope of this thesis. We instead refer the reader interested in these methods to the specialized references ⁷¹⁻⁷⁴.

Segmentation algorithms can be divided into two categories: approaches based on the study of regions in the image, named "region-based approaches" and approaches based on the study of the contours of objects in the image, called "contour-based approaches" ⁷⁵⁻⁷⁷. The region-based approaches are contextual and are based on the similarity of related points in the image (pixels or voxels). Points having similar properties (gray intensity, color, textures, statistics, geometric properties, etc.) will be combined into the same set ⁷⁸. The most commonly used algorithm based on this approach proceeds by region growing. Neighboring points with common characteristics are grouped together to form regions that increase in importance. Contour-based approaches are not contextual techniques which ignore the potential relationships between regions in the image. Points are grouped as a function of a global attribute. They include edge detection techniques. A closed contour may be necessary if the pixel's contours are not related. After this step, the regions appear and are defined by the inner contours. We will note that these two approaches are dual, in the extent that a region defines a line on the outline (or border) and conversely a closed line (or outline) defines an inner region.

These approaches have many disadvantages. Contour-based approaches, for example, often require a closing contour algorithm and the final result may be different from the desired or expected partition or segmentation. The region-based approaches are, in turn, usually time consuming and need important computational resources. New approaches grouped under the name of active contour methods have been proposed to overcome the limit of aforementioned techniques.

2.9.3 Active contours method for segmentation

These new approaches also grouped under the name of deformable models have been suggested to overcome the limitations of the classic methods of segmentation ^{70,79}. These deformable models use an *a priori* knowledge of the contours or the regions to segment. This knowledge can be derived based on learning, patterns or modes of deformation. These approaches called "active contour methods" (ACM) received special attention and scope as they seemed quite promising to provide closed and smooth contours for an object with a sub-pixel accuracy. They were originally introduced in the form of minimizing curves (or snakes) for edge detection (contours approaches) ^{70,79}. Almost all the classic methods of segmentation mentioned above have their equivalent in ACM ⁷⁰. ACM may also be divided into approaches based on the region analysis or on contour analysis. These segmentation techniques are widely used for the segmentation of medical images, and more particularly, for the segmentation of the vessels.

The principle of MCA is to develop an initial curve towards the object of interest under the action of one (or more) force(s), depending on the complexity of the model, usually inferred as a functional minimization ^{67,72}. The curve can be continuous or closed, with a fixed end or not. It is defined from a starting position located close to the object of interest. The curve deforms and moves into the image under the effect of the force(s): an external force pushing the contour to the most remarkable characteristics of the image (such as contours and edges, for example), and an internal force imposing regularity to the contours. MCA are defined as following :

Let Γ an active contour defined as parametric curve by $p \in [a, b]$ and by an evolution parameter $\tau \in [0, T]$, such as :

$$\begin{aligned} \Gamma : [a, b] \times [0, T] &\rightarrow \mathbb{R}^2 \\ (p, \tau) &\rightarrow \Gamma(p, \tau) = \mathcal{X}(p, \tau) = \begin{pmatrix} x(p, \tau) \\ y(p, \tau) \end{pmatrix} \end{aligned} \quad \text{Equation 5}$$

The evolution of the contour is governed by an equation in the following general form:

$$(\partial \Gamma(p, \tau)) / \partial \tau = F(p, \tau) \quad \text{Equation 6}$$

$$\partial \Gamma(p, 0) = \Gamma_0(p) \quad \text{Equation 7}$$

Where $\Gamma_0(p)$ is the initial contour.

The contour is deformed following a force F whose direction is arbitrary. This force F can be decomposed in a Frenet reference whose base is constituted by the inner unit normal vector N , and the unit tangent vector T :

$$F = F_N N + F_T T \quad \text{Equation 8}$$

Where $F_N N$ is the normal component of the force that changes the shape of the contour, and $F_T T$ is the tangential component that influences the parameterization of the contour.

In order to simplify the model, only the normal component is taken into account, and the evolution equation of an active contour is usually written, as follows:

$$\partial \Gamma(p, \tau) / \partial \tau = F_N(p, \tau) N(p, \tau) \quad \text{Equation 9}$$

$$\partial \Gamma(p, 0) = \Gamma_0(p) \quad \text{Equation 10}$$

The region-based ACM have many advantages over those based on contours analysis approach. They are far less sensitive to noise and to the need of a contour initialization, since they use region information as a substitute for the image gradient to constrain the evolution of contours. In addition, these methods allow us to segment images with objects presenting fuzzy or inexistent boundaries. Indeed, the contour-based ACM approaches are rapidly limited for the analysis of brain images or images with small-sized objects such as ICA, with sometimes the loss of the edges of the structures studied. This is explained by the sensitivity of these methods with low contrast and low defined contours of objects encountered in these images (i.e., 2D MRI-CP), due, among others things, to an associated partial volume effect⁷⁶.

The most known region-based MCA method is the model put forward by Chan-Vese (MCA-CV) which was used in the fourth part of this study⁸⁰.

2.10 The internal carotid artery : a particular case for segmentation

The ICA is an artery presenting specific morphological and anatomical features which may complicate its segmentation in PC-MRI images.

2.10.1 Anatomy of the internal carotid artery

From an anatomical point of view, the ICA is branch of the common carotid artery rising from its bifurcation. It extends from the upper edge of the thyroid cartilage to an intracranial intradural location, after passing through the intrapetrous carotid canal at the skull base. ICA describes many flexures on all its path from its cervical segment to its intracranial segments. The marked curves imposed by the bony carotid canal at the skull base and the "S" shaped curve in the cavernous sinus are constant. On the constant curvatures, variable ones are added in its cervical portion according to age (between two or three very marked curvatures)⁸¹⁻⁸³. All these curves are all potential sources of flow artifacts (aliasing, turbulence, etc.) that might alter the PC-MRI signal.

From a morphological and functional point of view, cervical ICA at its subpetrous segment has an average diameter of $4.7 \text{ mm} \pm 0.9 \text{ mm}$ in female and $5.1 \text{ mm} \pm 0.9 \text{ mm}$ in male which decreases along its intracranial route⁸⁴. The mean velocity in the ICA without evidence of carotid stenosis is of around $65 \pm 20 \text{ cm.s}^{-1}$ at the peak of systole and $25 \pm 10 \text{ cm.s}^{-1}$ at the end of the diastole⁸⁵. The limited size and relatively low velocities (when compared to the velocities within the heart or aorta) are associated with a weak signal in PC-MRI that can make its segmentation difficult.

2.10.2 Segmentation of the internal carotid artery

The ICA presents some specific "neighborhoods" with numerous structures (vascular or not):

1. With the cervical internal jugular vein and in particular at the skull base.
2. With the external carotid artery in its proximal cervical portion.
3. With the cavernous sinus in which the artery runs in contact with the venous blood.
4. With the bones and the air of the skull base (in its portion intra petrous segment).
5. With the CSF within the subarachnoid space in its intradural segments.

All these neighboring structures are potential sources of magnetically susceptible artifacts or flow disturbances around the artery that can potentially affect and alter the flow measurements in PC-MRI.

Despite early promising works, the segmentation of ICA images performed with flow MRI is little reported in comparison to the abundant literature on the segmentation of the heart or aorta⁸⁶. Manniesing et al. segmented ICA by focusing only on morphological criteria at the carotid bifurcations based on computed tomography or computed tomography images (CT or CTA)⁸⁷. Tang et al. used for segmentation of the ICA morphological MRI data with triple fat and blood saturation (Black Blood MRI) and PC-MRI. In the latter work, the segmentation of PC-MRI was performed on the amplitude images⁸⁸. Other authors have developed methods for ICA segmentation based on the coherence measurements of the velocities for the 3D segmentation of vessels⁸⁹⁻⁹¹. These approaches were based on the displacement information of the protons within the three spatial directions in a volume. According to the orientation of the mean velocity vector, it enabled the separation of voxels regarded as belonging to the vascular structure studied from those regarded as not. These approaches are of interest for the use of 3D PC-MRI, but does not apply to 2D PC-MRI as used in this work. Recently, Fasquel

et al proposed a semi-automated method for extracting lumen boundaries of the carotid artery and compute both lumen area and blood flow evolutions over the cardiac cycle. Their method used narrow band region-based active contours in order to correctly capture the lumen boundary without being corrupted by surrounding structures⁹². However, the method was not fully automated, but required some interactions for the initialization of the segmentation process.

CHAPTER 3

3 Aneurysm and parent vessel : an *in vitro* study of pressures and resistance

3.1 Introduction

As previously discussed in Chapter 2, hemodynamic factors play a crucial role in the aneurysmal pathology and the effectiveness of EVT^{2,40}. The CFD numerical methods have improved our understanding of this disease. However, these methods are little used in clinical routine. They require patient-specific information about the boundary conditions of the vessels hemodynamic, which are sometimes difficult to access *in vivo*, and significant computational resources are needed to achieve significant levels of accuracy. To overcome the difficulties of access to patient-specific physiological parameters (velocity, flow, pressure, etc.), approximations are made on the input conditions to the models, reducing the accuracy and reliability of its results in certain conditions.

Given the known limits of the numerical simulation methods, we opted at first for an *in vitro* experimental investigation to explore the impact of the aneurysm on the parent vessel flow conditions. The *in vitro* studies based on silicone models offer the possibility to control and to measure numerous parameters in order to address complex phenomenon. Nevertheless, it requires to bearking down the main problem into simple questions.

Therefore, before describing our methodology, a reminder of the circulatory conditions in the ICA is required. To simplify our discussion, we consider in this recall only the most common case of a single ICA without addressing the various possible anatomical variants or those of the Circle of Willis and all hemodynamic implications that would result. ICA's main objective is to perfuse and feed the brain. This artery is involved in cerebral autoregulation and is also dependent on it. The vascular autoregulation is a local manifestation of the blood flow regulation. It is a property of organs whose sole aim is to maintain a constant blood flow despite perfusion pressure changes⁹³. The perfusion pressure is defined by the difference between arterial blood pressure (P_A) and venous blood pressure (P_V). For example, autoregulation comes into play after the stenosis, or extreme occlusion of an artery vascularizing an organ. If the perfusion pressure decreases, blood flow decreases initially, and returns to normal within minutes. This autoregulation response occurs in the absence of hormonal or neural influences. It is intrinsic to the organ. The initial flow reduction is explained by the relationship between perfusion pressure, the flow (F) and resistance (Re) under conditions of physiological flow, that is to say, laminar flow :

$$F = (P_A - P_V)/Res \quad \text{Equation 11}$$

In a second step, the blood resistance also decreases following the decrease of the vascular resistance (by vasodilatation of small arteries and arterioles), thereby allowing increased flow

(F). The more the resistances decrease, the more the blood flow increases despite the presence of a reduced perfusion pressure. Several studies suggest the involvement of metabolic, myogenic and endothelial mechanisms which are beyond the scope of this thesis.

The aim of our work is to understand the impact of the aneurysm on the parent vessel hemodynamics subjected to the effects of cerebral autoregulation. The aneurysm has a slow growth. Its impact on the flow in the ICA which is subjected to cerebral autoregulation, should be a slow and gradual process. As we have seen, the cardiovascular system is a complex system whose main objective is to maintain sufficient capacity for oxygenation and organ function. It acts through changes in resistance and flow. Exploring *in vitro* the impact of the aneurysm on parent vessel hemodynamics is at the start limited by the difficulty to reproduce all these known conditions and complex interactions *in vivo*.

Therefore, a simplification of the problem was imposed. Considering the *in vivo* relative constant flow due to the law of conservation of mass, if the aneurysm does affect the blood flow within the parent vessel, it must change the pressure and/or the resistance within it. We therefore naturally focused our methodology in quantifiable parameters of the hemodynamic within the parent vessel to characterize the effect the aneurysm. Because of the characteristics of the cardiovascular simulator used in this work which will be described later, the simplified main question in this experimental part of our work was the following: what is the effect of the aneurysm on the pressures and resistance within the parent vessel at constant flow? Secondly, we assessed the effect of FDS deployment on the flow within the parent vessel.

3.2 Materials and Methods

We favored experimental measurements instead of simulation in the methodological design of this work. A cardiovascular simulator allowing the reproduction of a pulsatile flow in a hydraulic circuit was used. Two silicon aneurysm models (A and B) and a straight tube (or "straight artery") in silicon were used and integrated within the circuit for different experiments.

A first study consisted to measure the pressures in the hydraulic circuit upstream and downstream to the aneurysm A and to calculate the hydraulic resistance between the two measurement points containing the aneurysm and the parent vessel. The experiment was performed before and after deployment of a FDS covering the aneurysm A. Similar measurements as control conditions were performed upstream and downstream to the right tube before and after the FDS deployment. A second study was conducted to evaluate fluid movement between the parent vessel and the aneurysm, before and after the deployment of a FDS. A spherical aneurysm model in silicon (aneurysm B) was used. The fluid circulating into the hydraulic circuit was marked by red blood cells (RBC) as a colored marker. The distribution of the RBCs within the aneurysmal sac has been recorded by a high resolution camera and the obtained images were post-processed. Segmentation and quantitative analysis of the RBCs' distribution within the aneurysmal over time were performed. The experiment was performed before and after the deployment of a FDS into the parent vessel.

3.2.1 Cardiovascular simulator

3.2.1.1 Cardiovascular simulator : Description of the test bench

A cardiovascular simulator was used to perform all the *in vitro* experiments. It was developed at the University of Mons by Dr. K. Chozinsky⁹⁴. The experimental setup allows the reconstitution and the precise control of flow conditions (either pulsatile or continuous) within a closed hydraulic circuit and the measurements of flow rates and pressures at various points of the circuit. The simulator is illustrated in Figure 7. It consists of a test bed powered by pressure constraints and an upstream flow and a signal post-processing module downstream. The system is controlled in real time and was originally designed for the *in vitro* reconstitution of pulsatile flow profile as close as possible to the physiological blood flow conditions measured *in vivo* in order to study endothelial cells⁹⁴. It includes a reservoir containing the fluid (usually a mixture of water and glycerin to reproduce the density and viscosity of the blood), a first configurable centrifugal pump characterized by its flow, its outlet pressure and speed of rotation (High-Performance Stator PS01-23x80F-HP-R and High Performance slider for H-Guide PL01-12x200/160-HP, Linmot), a one-way valve at the outlet of the centrifugal pump, a second piston pump (D-94-81, Diacom) consisting in a linear motor and a diaphragm piston, a thermocouple the real-time measurement of the fluid temperature. Several sensors for pressure (two in our work) and an electromagnetic flowmeter (EF, MM-04-XX-VD-SS-XX-0000-22-1A-1F-00-2R-00-SK, Minimag) are also available for real-time measurements of pressures and flow rates. These three components can be positioned at different points of the hydraulic circuit made of polymer tubing depending on the specifics of the study. The silicone tube circuit had a length of 0.83 m and a constant diameter of 4.8 mm, apart from a modifiable and interchangeable segment whose length corresponds to those of the aneurysm model or of the straight tube studied.

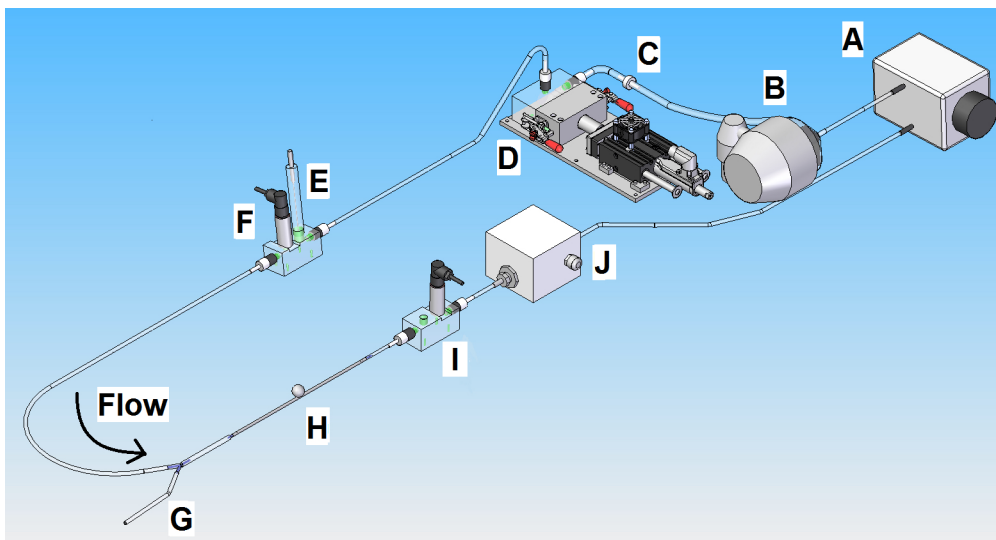


Figure 7 : The Principle of the cardiovascular simulator (test bench).

The hydraulic system consists on : (A) a tank comprising of a mixture of water and glycerin (mass 62% / 38%), (B) centrifugal pump, (C) one-way valve, (D) piston pump consists of a linear motor and a piston with a diaphragm, (E) Thermocouple (F) pressure transducer - Upstream, (G) silicone modifiable segment (H) allowing for the test of the aneurysm models, (I) pressure sensor - Downstream, (J) electromagnetic Flowmeter - Aval. The picture comes from the work of Kamil Jerzy Chodzyński⁹⁴.

3.2.1.2 Cardiovascular simulator : Principle of the flow regulation

The principle of the simulator is based on a joint regulation loop based on three regulators⁹⁴ as illustrated in Figure 8, including : an internal model control (IMC) incorporating a proportional integral controller (PI) and two additional PI controllers. The control by combining the first two regulators acts on the optimized piston pump. The main component of the flow is controlled by the IMC. Fluctuations of the flow around the main component are controlled by the PI controller. The additional PI controllers control in real-time the average flow rate and temperature within the hydraulic circuit respectively. The IMC based regulation is a robust and efficient corrector used in automation and robotics^{95,96}. It works by correcting deviations from the model (i.e., physiological pulsatile flow input or "set flow" in our work). The gap is sent down to the block entrance. It is seen as a disturbance to compensate. The system acts simultaneously on the flow production process (pump) and the model to decrease (at best cancel) the gap, until the desired flow condition is obtained. The IMC has an implicit integral action and unlike the proportional integral and derivative controller (PID), it takes into account the signal derivatives of order greater than 2. It therefore can achieve better reconstitution of complex pulsatile flow. The PI acts by two forces: one force proportional to the difference between the measured flow and the set point flow, and a second force proportional to the integration of the difference between the set point flow and the measured flow in time (the sum of all constantly measured deviations). The advantage of this controller is its action on the low frequencies of the signal and its zero static error. For a given input set, the static error is the difference between the input and output of the system for t tending to infinity (i.e., physiological pulsatile flow condition input in the simulator). From a reference flow profile, combining the centrifugal pump and the piston pump allows us to reproduce reliably and accurately blood flows ranging from of $40 \text{ ml}\cdot\text{min}^{-1}$ to $700 \text{ ml}\cdot\text{min}^{-1}$ with less than 5% of error⁹⁴.

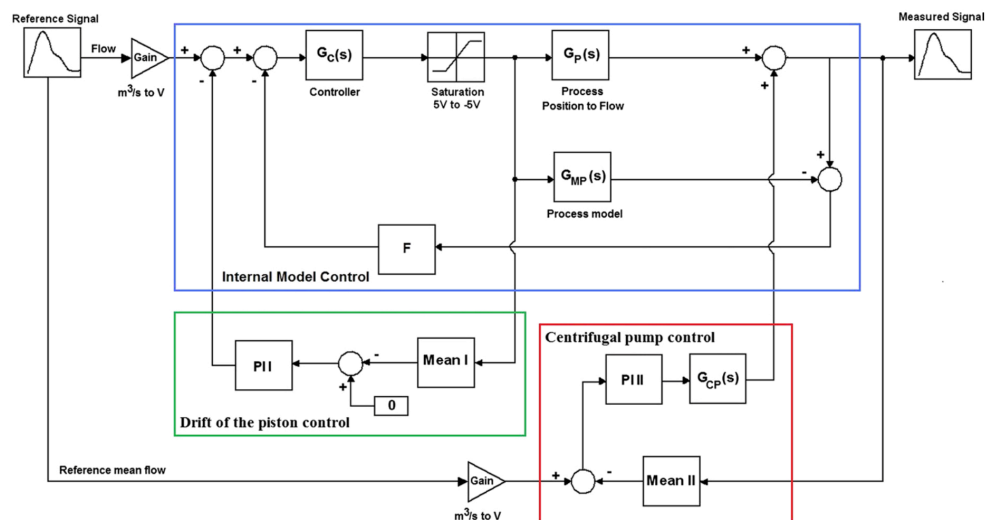


Figure 8 : The Principle of the flow regulation by the cardiovascular simulator.

The principles of the control system in the cardiovascular simulator can be defined in three parts. The internal model control (IMC, blue frame) responsible for controlling the position of the piston pump. To reduce the noise from the measurement signal flows during operation and thereby preventing the deflection of the piston pump, a filter (box F) and an additional control loop based on a proportional-integral (PI) controller and an Averaging function I have integrated into the system (green box). The average flow of control is provided by a second control loop composed of a PI controller and a function Average II (red frame). The picture comes from the work of Kamil Jerzy Chodzyński⁹⁴

3.2.1.3 Cardiovascular simulator : Differences with the vascular autoregulation

The simulator is differentiated from the cardiovascular system by its control mode and the possible actions on the flow, pressure and resistance parameters. The flow is constantly monitored by the sensors for pressure and flow rate which feed the control system. This latter intervenes and acts in turn on the pumps to correct the flow rate and/or the outlet pressure in order to align the measured flow within the circuit to the set point. The resistance of the system depends on the fluid properties and the geometry of the hydraulic silicon circuit (diameter, length and tortuosity of the pipes). It can be changed between two different experiments by varying the geometry of the circuit, but remains constant for the same experiment. In other words, flow regulation by the simulator is therefore based mainly on changes in pressure or flow rate from the pumps. However, these two parameters are interdependent. For a given resistance, any change in pressure will induce a change in the flow rate and vice versa. These characteristics portray significantly the different behavior of the test bench from those of the cardiovascular system for the regulation of flows. The first acts at constant resistance on the pressure or the flow rate without any possibility of simultaneous change to ensure the desired flow. The second acts on the resistances and/or flow, simultaneously or not, and secondarily on the perfusion pressure to provide the desired flow rates and maintain adequate tissue perfusion.

3.2.1.4 Characteristics of the flow within the test bench

The hydraulic system and the flow in the simulator were characterized by:

- A fluid consisting of a water and glycine mixture (62% / 38%) having a density ρ of 1098 kg.m^{-3} and a dynamic viscosity μ of $3.45 \times 10^{-3} \text{ Pa.s}^{-1}$ (or in $\text{kg.m}^{-1}.\text{s}^{-1}$), to get as close as possible to the properties of blood (μ_s is approximately equal to $6.0 \times 10^{-3} \text{ Pa.s}^{-1}$ and varying between 4.0×10^{-3} and 25.0×10^{-3} ; ρ_s varie between 1056 and 1066 kg.m^{-3}).
- A silicone tube diameter of $4.8 \times 10^{-2} \text{ m}$, resulting in a sectional area of $1.810 \times 10^{-5} \text{ m}^2$.
- A volumetric flow rate maintained by the pump 123 ml.min^{-1} ($2.05 \times 10^{-6} \text{ m}^3.\text{s}^{-1}$).
- A fluid velocity of 0.113 m.s^{-1} deduced from Q and S according to the equation $Q = S \times V$ and therefore $V = Q/S$.

The conditions of the fluid and the characteristics of the hydraulic circuit mentioned above resulted in a Reynolds number (Re) of 173 (less than 2300) according to the equation (12). Thus, it fulfilled the conditions of a permanent laminar flow (Poiseuille flow).

$$Re = (\rho \cdot d \cdot V) / \mu \quad \text{Equation 12}$$

$$Re = \frac{1098.8 \times 0.0048 \times 0.2303}{0.00345} = 173$$

Under these conditions, the flow rate Q (in $\text{m}^3.\text{s}^{-1}$), the pressure drop ΔP (or pressure drop in the direction of flow in Pa between the two points of pressure measurements, equivalent to the *in vivo* perfusion pressure) and the resistance Res (in Pa.s.m^{-3}) between the two points of pressure measurements satisfied the relation:

$$Q = \Delta P / Res \quad \text{Equation 13}$$

3.2.1.5 Modifiable and non-modifiable parameters of the cardiovascular simulator

All the experiments performed with the simulator were carried out under the same constant pulsatile flow (described later in Chapter 3, § 3.2.5). The overall resistance of the hydraulic circuit varied between experiments, but was constant for the same experiment, as well as the measured pressures P1 and P2. No modification of the circuit was made during an experiment and measurements. Therefore, the flow conditions within the circuit could be considered as stationary for all experiments (constant pulsatile flow and pressures, and constant resistance for each condition studied). The flow within the circuit could thus be expressed as:

$$Q = \int_0^R 2\pi r v(r) dr = [(\pi R^4)/8\mu L] \delta P \quad \text{Equation 14}$$

With r the radial position on the vessel section (in m), R the radius of the pipe (in m), L the discrete length of the pipe (in m), μ the dynamic viscosity of the fluid ($\text{Pa}\cdot\text{s}^{-1}$ or $\text{kg}\cdot\text{m}^{-1}\cdot\text{s}^{-1}$). The hydraulic resistance Res_h of this circuit (in $\text{Pa}\cdot\text{s}\cdot\text{m}^{-3}$) can thus also be expressed as:

$$Res_h = 8\mu L/(\pi R^4) \quad \text{Equation 15}$$

Equation (15) illustrates the dependence of Res_h from the power of 4 of the radius R of the tube, which is also its main determinant. To simplify the calculations of resistance, we opted for the simplest relationship described in equation (13).

3.2.2 Silicone aneurysm models and flow diverter stents

3.2.2.1 Silicone aneurysm models

Two aneurysm models in transparent silicone (Elastrat company, Switzerland, <http://www.elastrat.com>) were used in this work. A patient-specific aneurysm model with a complex morphology (aneurysm A) and a simple and spherical aneurysm (aneurysm B)⁹⁷.

The aneurysm model A measured 9.8 mm in diameter and 18.7 mm in depth, and had a neck measured to 10.6 mm. It was sacciform and oblong and had a volume of 1775 mm^3 and an aspect-ratio of 1.76. The parent artery presented diameters of 5 mm, 4.2 mm and 3.7 mm upstream, in front of and downstream to the aneurysm, respectively, with a thickness of 0.7mm. The most proximal end of the silicone model measured 5.5 mm in diameter and corresponded to a cervical sub-petrous segment of the ICA, while its most distal end measured 2.5 mm in diameter and corresponded to a M1 segment of the middle cerebral artery. The artery was 15 cm in length. This model was used to study pressure measurements and to calculate the resistance. The aneurysm model B measured 9.3 mm in diameter. It had a volume of 421 mm^3 and an aspect-ratio of 1.1. The parent vessel in this model was a straight silicone pipe and measured 3.5 mm in diameter, 280 mm in length, with a thickness of 0.7 mm. A straight silicone tube was used to test the condition “straight artery” (or “straight pipe”) compared to the aneurysm model A. It measured 4.2 mm in diameter, 15 cm long and had a thickness of 0.7 mm. The mechanical properties of silicone used for the realization of these models were the followings: stiffness (Shore A) 40 tensile strength of 6.7 MPa, elongation at break of 400%, ISO tear strength 34 Cutter 27 N / mm , density $1090 \text{ kg}\cdot\text{m}^{-3}$.

Figure 9 shows the aneurysm models A and B and the straight pipe used for the experiments.

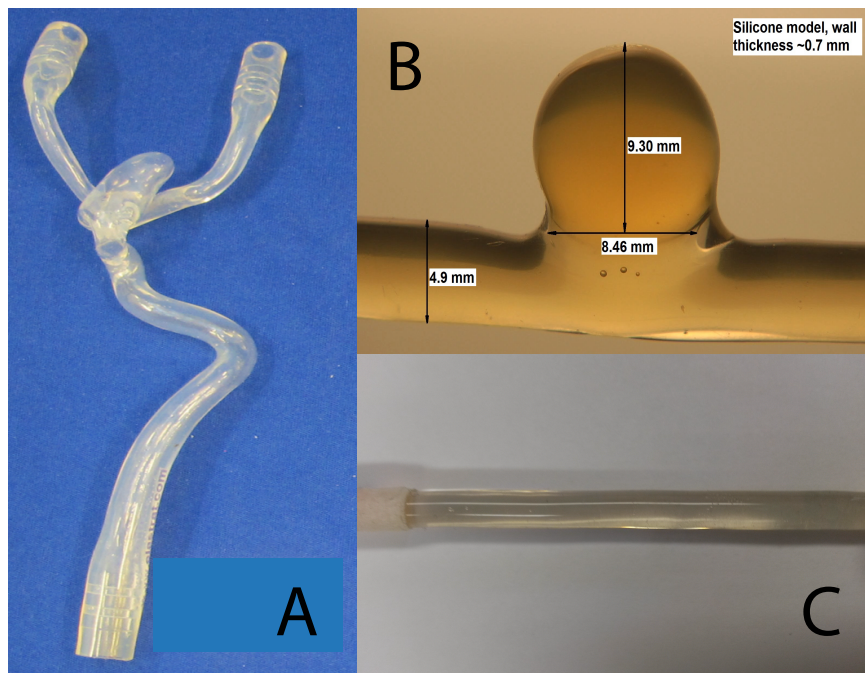


Figure 9 : Tested aneurysm silicone models

This picture shows the patient-specific aneurysm model A (A), the simplified aneurysm model B (B) and the straight pipe (C).

3.2.2.2 Flow diverter stents

A Pipeline Embolization Device (PED, EV3 company, Irvine, USA, shown in Figure 10) was deployed in each aneurysm and in the “straight pipe” for this work⁹⁸. This stent acts on the diseased arterial segment by redirecting the flow in the parent vessel, promoting therefore the blood stagnation and thrombosis into the aneurysmal sac. Thus it allows the geometric and hemodynamic reconstruction of the parent vessel^{32,98}. Each stent was braided from 48 cylindrical strands consisting of an alloy of 75% Chrome-Cobalt and 25% Tungsten-Platinum. The diameter of each strand was 30 micrometers. The first PED used in aneurysm A measured 4.25 mm in diameter and 20 mm length, while the second one used in aneurysm B measured 3.5 mm in diameter and 20 mm length. The PED used in the “straight pipe” measured 4.25 mm in diameter and 20 mm length. They were suited to the parent artery dimensions.

To reproduce the *in vivo* conditions of the device deployment in a patient, the FDS were deployed after navigation and positioning of a Marksman microcatheter (0.027 inch; EV3 company, Irvine, USA). The FDS deployments were performed in compression in all cases to maximize the flow diversion effect of the devices.

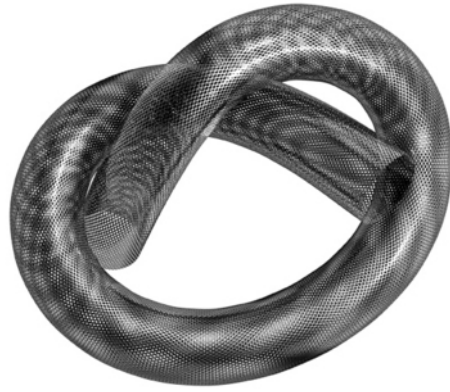


Figure 10 : The Pipeline™ Stent flow diverter.

3.2.3 Pressures and resistance measurements in the parent vessel

As we previously have described, the simulator works at constant resistance and allows the modifications of flow rate or pressure, not both. The last two parameters are interdependent. For a given resistance, any pressure change induced a reaction in flow rate change, and vice versa. Given these characteristics of the simulator, we chose to work at a constant flow rate and measure the pressure in the hydraulic circuit at two points on either side of the aneurysm. The used sensors, whose layout is illustrated in Figure 7, consisted of:

- A pressure sensor upstream to the aneurysm (P1)
- A pressure sensor downstream to the aneurysm (P2)
- An electromagnetic flowmeter positioned arbitrarily downstream to the aneurysm.

The sensors recorded the changes in the electrical current (V) within the fluid induced by pressure and flow changes corresponding to the electrical equivalent of pressures and flow rates. The pressure value conversions expressed in mmHg and flow expressed in ml.min⁻¹ were thus obtained by the following equations directly related to the electrical characteristics of the simulator:

$$P = (P_{measured} \times 150.012) - 750.06 \quad \text{Equation 16}$$

$$Q = (Q_{measured} \times 272.59) - 154.01 \quad \text{Equation 17}$$

With P and $P_{measured}$ the pressures measured in mmHg and V, respectively, Q and $Q_{measured}$ the flow rates measured in ml.min⁻¹ and V, respectively.

The H segment in the hydraulic system (see Figure 7) was changed between the two experiments and was allowed to integrate the silicone aneurysm model or the silicone straight pipe (as control condition). Several experimental conditions were conducted with:

- The aneurysm model A without any material in the parent artery (experiment 1).
- The aneurysm model A model after the deployment of the FDS in the parent artery (experiment 2).
- The straight silicone tube without any material ("straight pipe"; experiment 3).

- The straight silicone tube after the deployment of the FDS ("stented straight pipe". experiment 4).

Flow measurements made by the flowmeter and pressures P1 and P2 were recorded in real-time throughout the duration of the experiments. For each experiment (1, 2, 3 and 4), the simulator was starting a phase of preparation of the pulsatile flow. Once the reconstituted pulsatile flow reached the “ set point ”, the measuring experiment began. The measurement time was 60 seconds for all of the four experiments. The characteristics of the pulsatile flow used for the three experiments are described in subsection §3.2.5 (Chapter 3).

A total of 60 cycles were thus recorded for each experiment. For each cycle, the minimum values (min), average (mean) and maximum (max) of flow rates Q (in $\text{ml}\cdot\text{min}^{-1}$) and pressures $P1$ and $P2$ (in mmHg) were considered as Q_{min_i} , Q_{mean_i} , Q_{max_i} , $P1_{min_i}$, $P1_{mean_i}$, $P1_{max_i}$, $P2_{min_i}$, $P2_{mean_i}$ and $P2_{max_i}$, with i the cycle number ranging from 1 to 60.

As previously described in the simulator set up, the piston pump for the reconstitution of the flow modulations is associated with a hydraulic circuit made of silicone tubes which have a negligible capacitance. Accordingly, the pressure measurements P1 and P2 exhibit cyclic variations with positive and negative values of pressures. It was explained by the effect of the specific movements of the piston pump on the flowing fluid without any correction. Indeed, the periodic reversing of the piston pump is associated with a suction of the fluid within the closed hydraulic circuit. This suction phenomena induces negative pressures which are recorded during the diastole of each cycle. The absence of capacitance of the hydraulic system does not compensate for this effect and does not maintain positive pressure throughout the cycle. Consequently, only the positive pressure measurements and flow rates registered at the systolic peaks were considered for the calculation of the resistances for each cycle (ie, values of Q_{max_i} , $P1_{max_i}$, $P2_{max_i}$, and ΔP_{max_i}), such as:

$$Res_i = \Delta P_{max_i} / Q_{max_i} \quad \text{Equation 18}$$

The Res_i resistance corresponds to the overall resistance of the hydraulic circuit between the points P1 and P2, including the H segment (aneurysm model A or “straight tube”). The values of Q_{min_i} , Q_{mean_i} , Q_{max_i} , $P1_{min_i}$, $P1_{moy_i}$, $P1_{max_i}$, $P2_{min_i}$, $P2_{moy_i}$ and $P2_{max_i}$ were measured and the values of ΔP_i and Res_i were calculated for the aneurysm model A before and after FDS deployment and for the straight silicone tube before and after FDS deployment. The means and standard-deviations (mean \pm SD) over 60 cycles of each of these values (Q_{min_m} , Q_{mean_m} , Q_{max_m} , $P1_{min_m}$, $P1_{mean_m}$, $P1_{max_m}$, $P2_{min_m}$, $P2_{mean_m}$ and $P2_{max_m}$, ΔP_{max_m} , Res_m) were calculated. The obtained values of ΔP_{max_i} and Res_i between experiments 1 and 2 and between experiments 3 and 4 were compared and test with a Mann Whitney U test or a Student t-test according to the result of the Shapiro-Wilk normality test.

3.2.4 Fluid movements between the aneurysms and the parent vessel

Given the difficulty to precisely quantify the volume of fluid passing through an aneurysm with a complex morphology over time without direct intervention on the system (the test bench and the aneurysm), we opted for a simplified approach in this part of our work. We used simple spherical aneurysm model aneurysm B, and a two-dimensional analysis of the

fluid distribution within the aneurysmal sac before and after FDS deployment (experiments 5 and 6).

The method was based on the monitoring and the quantification of fluid movements between the parent vessel and the aneurysm on 2D images. The fluid was marked by a natural dye: the red blood cells (RBCs). RBCs were injected into the hydraulic circuit upstream to the aneurysm as illustrated in Figure 11 and their distribution in the aneurysmal sac was recorded by a high resolution camera.

For this experiment, a shadow-less tent with white walls was set up and a lamp placed in the background of the tent. It ensured the optimal illumination of the image background and therefore reduced the reflection and shadow effects on the aneurysm for the entire duration of the experiment and recording. The circulating fluid was the same mixture used previously (water and glycerin mixture with a ratio 62% / 38% resulting in $\rho = 1098 \text{ kg.m}^{-3}$ and $\mu = 3.45\text{e-}3 \text{ Pa.s}^{-1}$) in which a RBC mixture was injected very slowly (1mL of 77% RBCs diluted in 100mL of Sodium Adenine Glucose Mannitol buffer) at a speed of 211.7 ml/h. The injection was performed slowly with a syringe pump (model 78-91001 Fisher Scientific™) in the closed circuit over a period of 17 seconds upstream of the aneurysm as shown in Figure 9. This resulted in a hematocrit of marked fluid below 10% (around 7%) for the all the duration of the injection⁹⁹. This condition allowed also negligible change in viscoelastic properties of the fluid while maintaining a good visibility of the RBCs. The distribution of the fluid marked by RBCs in the aneurysmal sac (input and output) over time was recorded by a high resolution camera (Panasonic SD700 Full HD 1080p Camcorder). The recording started before the injection of the RBCs and lasted 90 seconds. All experiments were carried out at room temperature (21° C).

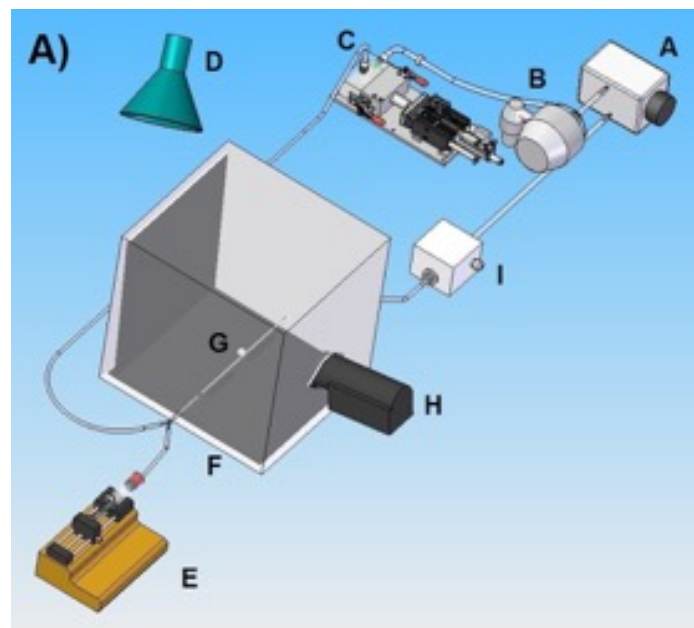


Figure 11 : Set up of the experiments 2 and 3.

In comparison to the previous experimental set ups (experiments 1 and 2), additionally the test bench included: a shadow-less tent with white walls (G) in which the aneurysm was put, a lamp placed in the background of the tent (D), a syringe pump for the RBC injection (C), and a high resolution camera (H). The picture comes from the work of Kamil Jerzy Chodzyński⁹⁴

The obtained high-resolution images were post-processed using the following steps (illustrated by Figure 12) :

1. Sequences of single images were extracted from the recorded movies from each experiment (Figure 12-A).
2. A mask was applied to the extracted images to provide a segment of the aneurysm (Figure 12-B).
3. RGB (Red Green Blue) color map images were converted into HSV (Hue Saturation Value) color map pictures. Only the significant color levels indicating the presence of RBCs (ranged from 330 to 30, centered on the color of RBCs) were extracted (Figure 12-C).
4. The processed images were converted into binary files in order to track the RBCs mixture passing through the spherical aneurysm model (Figure 12-D).

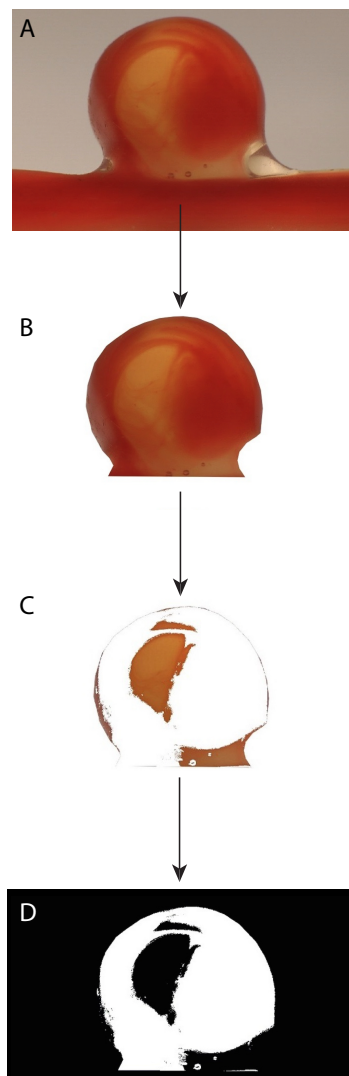


Figure 12 : The segmentation of the intrasaccular RBCs distribution over one cardiac cycle.

Segmentation of intrasacculaire RBCs distribution over time. The different steps included : the extraction of the images from the movie (A), the aneurysm masking, the Extraction of the desired range of colors (C) and the final binary output picture with a white tracer of the red blood cells enabling the RBC counting. The picture comes from the work of Kamil Jerzy Chodzyński⁹⁴

The amount of RBCs passing through the aneurysm was assessed using the following equation 19 describing the normalized mean residence time ($NMRT$ in s^{-1}) of the RBCs in the aneurysmal sac:

$$NMRT = \frac{1}{T} \int_0^T N(t)/N_0 dt \quad \text{Equation 19}$$

Where: N_0 is the number of white pixels assuming complete filling of the aneurysm by RBCs or the total surface in pixels of the 2D aneurysm (i.e., the number of white pixels corresponding to a binary image of the 2D saturated aneurysm), $N(t)$ is the number of white pixels covering the aneurysm surface at the time t (i.e., the surface in pixels of the aneurysmal sac occupied by the RBCs or the number of white pixels at the time t), and $N(t)/N_0 \leq 1$ is the area fraction of the aneurysmal sac occupied by the RBCs at time t (i.e., the normalized number of white pixels at time t), and T the full experiment duration.

The experiment was carried out before and after deployment of the FDS (experiment 5 and experiment 6, respectively). The time for which the values of $N(t)/N_0$ were maximal and minimal (for $[N(t)/N_0]_{max}$ and $[N(t)/N_0]_{min}$ respectively) and the $NMRT$ calculated for the two experiments were considered and compared.

3.2.5 Input flow instruction : an *in vivo* measured pulsatile flow

The input flow condition used in the test bed for reproducing the continuous pulsatile flow used in all the experiments (from 1 to 6) described above was obtained from a 2D PC-MRI flow measurement performed *in vivo* and provided by the interventional neuroradiology department of the CHU of Montpellier (France). It corresponded to a measured flow of the cervical ACI in a healthy volunteer aged 51 and having no cardiovascular risk factor. In particular, the voluntary showed no steno-occlusive anomaly of the supra aortic trunks or intracranial arteries. The flow was characterized by an average flow rate of $125 \text{ mL}\cdot\text{min}^{-1}$ and a frequency of 1 Hz (60 beats per minute). Figure 13 illustrates the flow profile reconstituted *in vitro* by the test bench. The technique and protocol of the used 2D PC-MRI are detailed in Chapter 4 (§ 4.2.3).

3.2.6 Statistical analysis

For Experiments 1, 2, 3 and 4, the values (mean \pm SD) of Q_{min} , Q_{moy} , Q_{max} in $\text{mL}\cdot\text{min}^{-1}$, and of $P1_{min}$, $P1_{moy}$, $P1_{max}$, $P2_{min}$, $P2_{moy}$ et $P2_{max}$ in mmHg were calculated over 60 cycles. The values for the aneurysm model A before and after FDS deployment (experiments 1 and 2) and for the straight tube before and after FDS deployment (experiments 3 and 4) were compared by the Rank Test of Mann-Whitney. The values of $NMRT$ expressed in s^{-1} calculated from experiment 5 and 6 were compared. A P-value less than 0.05 was considered to indicate a significant difference. The graphs and statistical tests were performed with free software R (R 3.2.1 software, Vienna, Austria, 2015; <http://www.R-project.org>)¹⁰⁰.

Input Flow Condition For all experiments

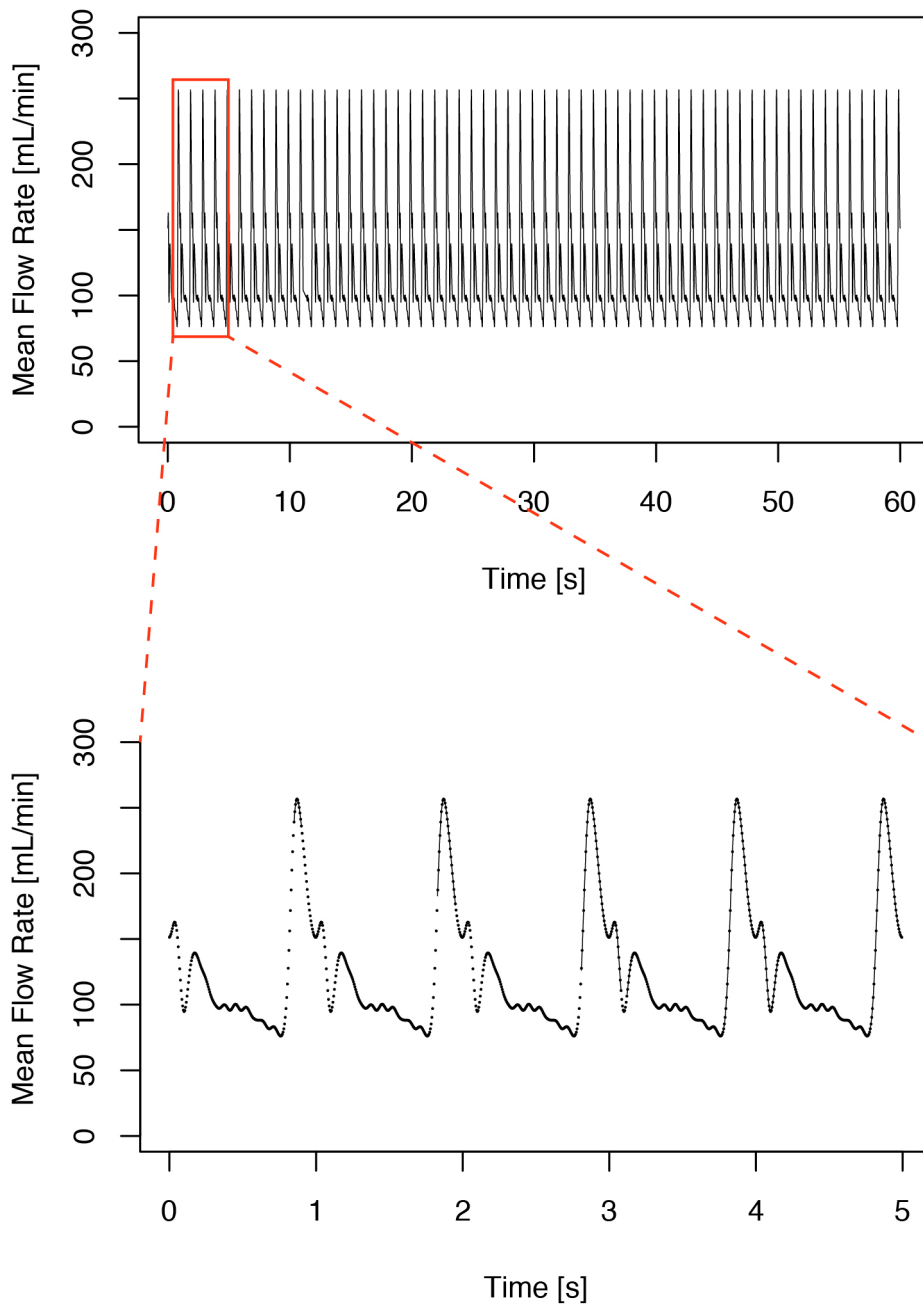


Figure 13 : The set point pulsatile flow used as input to the cardiovascular simulator

Input pulsatile flow condition (or "set point") of the simulator. This pulsatile flow was characterized by an average flow rate of 125.0 ± 1.9 L/min (minimum and maximum flow rates 88.0 ± 1.2 mL / min, and 259.4 ± 1.7) and a frequency of 1 Hz (60 beats per minute).

3.3 Results

3.3.1 Measured pressures and upstream and downstream to the aneurysm

The values over the 60 cycles of Q_{min_m} , Q_{mean_m} , Q_{max_m} , $P1_{min_m}$, $P1_{mean_m}$, $P1_{max_m}$, $P2_{min_m}$, $P2_{mean_m}$ and $P2_{max_m}$, ΔP_{max_m} , Res_m measured and calculated in experiments 1, 2, 3 and 4 are shown in Table 1. The flow rate curves, and the pressure curves $P1$ and $P2$ measured in the experiments 1, 2, 3 and 4 are reported in the Figures 14 to 18.

The values of Q_{min_m} , Q_{mean_m} , Q_{max_m} were 91.8 ± 5.6 , 125.2 ± 5.8 and 257.9 ± 7.5 in experiment 1, 71.55 ± 8.4 , 115.92 ± 6.3 and 260.4 ± 6.2 in experiment 2, 88.8 ± 1.2 , 127.1 ± 1.6 and 251.5 ± 1.6 in experiments 3 and 4. It resulted in average values of Q_{min_m} , Q_{mean_m} , Q_{max_m} of 84.0 ± 10.9 , 123.8 ± 5.35 and 255.3 ± 4.5 . The flow rate curves over time measured in the different experiments are illustrated in Figure 14.

Experiments		Measured parameters			Calculated parameters	
		Q (mL/min)	P1 (mmHg)	P2 (mmHg)	$\Delta P = P1 - P2$ (mmHg)	$R = \Delta P / Q$ (mmHg.min.mL ⁻¹)
Experiment 1 (Aneurysm A – FDS)	min	91.8±5.6	-73.3±3.0	-57.4±3.0	-	-
	moy	125.2±5.8	5.3±0.6	-6.5±0.7	-	-
	max	257.9±7.5	212.3±3.9	85.0±3.6	127.2±1.5	0.49±0.01
Experiment 2 (Aneurysm A + FDS)	min	71.5±8.4	-74.8±3.1	-46.9±1.3	-	-
	moy	115.9±6.3	6.6±0.9	-5.4±0.5	-	-
	max	260.4±6.2	206.4±3.8	67.7±2.0	138.7±2.2	0.53±0.01
Experiment 3 (Straight tube – FDS)	min	88.77±1.2	-27.7±1.3	-64.3±1.2	-	-
	moy	127.1±1.2	12.2±0.5	-1.4±0.3	-	-
	max	251.5±1.6	168.4±1.8	94.5±0.3	73.9±0.0	0.29±0.01
Experiment 3 (Straight tube + FDS)	min	88.8±1.2	-27.6±1.4	-61.7±0.5		
	moy	127.1±1.6	10.1±0.5	-2.1±0.1		
	max	251.5±1.6	167.8±1.6	93.8±0.5	74.9±0.0	0.29±0.01

Table 1 : Results of flow, pressure measurements and resistance calculations in the experiments 1 to 4.

Q is the flow rate (in mL.min-1), $P1$ and $P2$ the pressure (in mmHg) measured upstream and downstream to the aneurysm A or the straight tube. ΔP is the pressure drop between pressures $P1$ and $P2$ and R the calculated resistance (in mmHg.min.mL-1).

In experiments 1 and 2, the values of $P1_{max_m}$ before and after the FDS deployment were of 212.3 ± 3.9 mmHg and 206.4 ± 2.0 mmHg, respectively, without significant difference. The values of $P2_{max_m}$ before and after the FDS deployment were significantly different with a decrease of $P2_{max_m}$ after the FDS deployment, with values of 85.1 ± 3.6 mmHg before and of 67.7 ± 2.0 mmHg after the stent deployment. This difference was statistically significant ($P < 0.001$). It resulted in a significant increase in ΔP_{max_m} after the FDS deployment equal to 138.7 ± 2.2 mmHg versus 127.2 ± 1.5 mmHg before the FDS deployment (increase of 9%; $P < 0.001$). Similarly, there was a significant increase of Res_m after the FDS deployment equal to 0.53 ± 0.01 mmHg.min.mL⁻¹ versus 0.49 ± 0.01 mmHg.min.mL⁻¹ before the FDS deployment (increase of 8.2%; $P < 0.001$).

In experiments 3 and 4, the values of $P1max_m$ before and after the FDS deployment were of 168.4 ± 1.7 mmHg and 167.84 ± 1.6 mmHg, respectively, without significant difference. The values of $P2max_m$ before and after the FDS deployment were slightly different with values of 94.5 ± 0.3 mmHg and 93.8 ± 0.5 mmHg, respectively ($P < 0.001$). It resulted in slightly different $\Delta Pmax_m$ between before and after the FDS deployment with values of 73.9 ± 0.0 and of 74.9 ± 0.0 , respectively. However, the resulting Res_m before and after the FDS deployment were of 0.29 ± 0.01 and 0.29 ± 0.01 without significant difference.

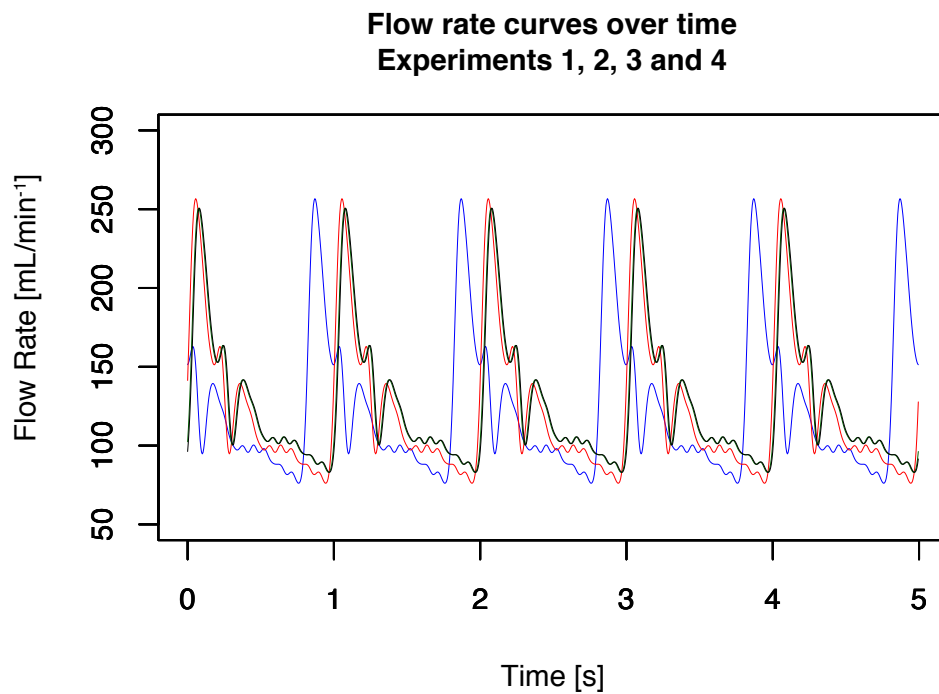


Figure 14: Flow rate curves over time measured in experiments 1 and 2.

The chart shows the reproduced flow conditions (flow rates over time) in the different experiments : experiment 1 (blue curve), experiment 2 (red curve), experiment 3 (green curve) and experiment 4 (black curve). All curves are highly consistent.

Aneurysm model A
P1 pressure measurements
Before and after FDS deployment

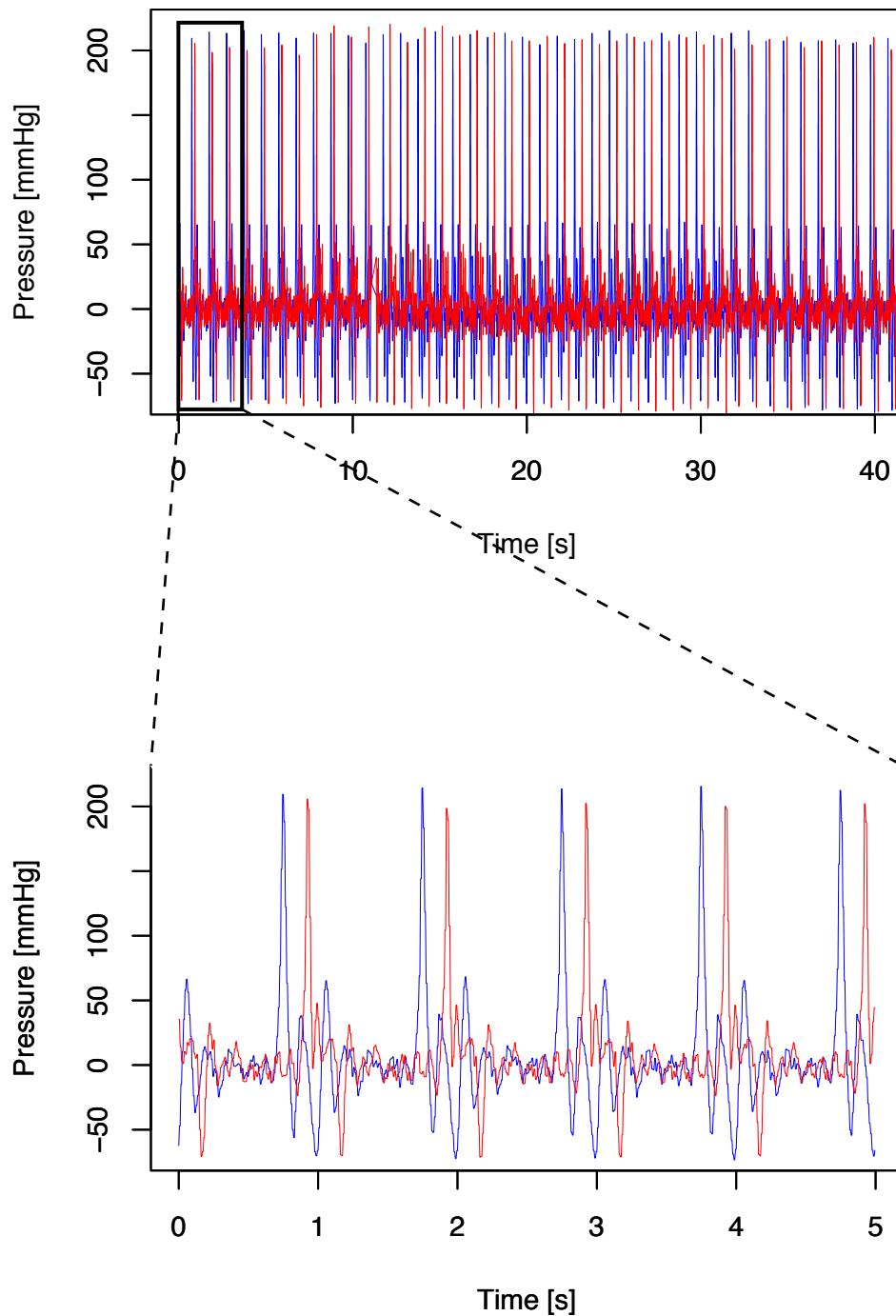


Figure 15 : Pressure P1 measured before and after the FDS deployment with aneurysm A

The charts show the Pressure P1 measured in the hydraulic circuit during the experiment 1 (blue curve) and the experiment 2 (red curve), namely before and after the FDS deployment respectively. The experiments 1 and 2 lasted 60 seconds. Only 40 and 5 cycles were represented respectively in this figure for a better readability. The P1 pressures before and after the endovascular treatment were not significantly different.

Aneurysm model A
P2 pressure measurements
Before and after FDS deployment

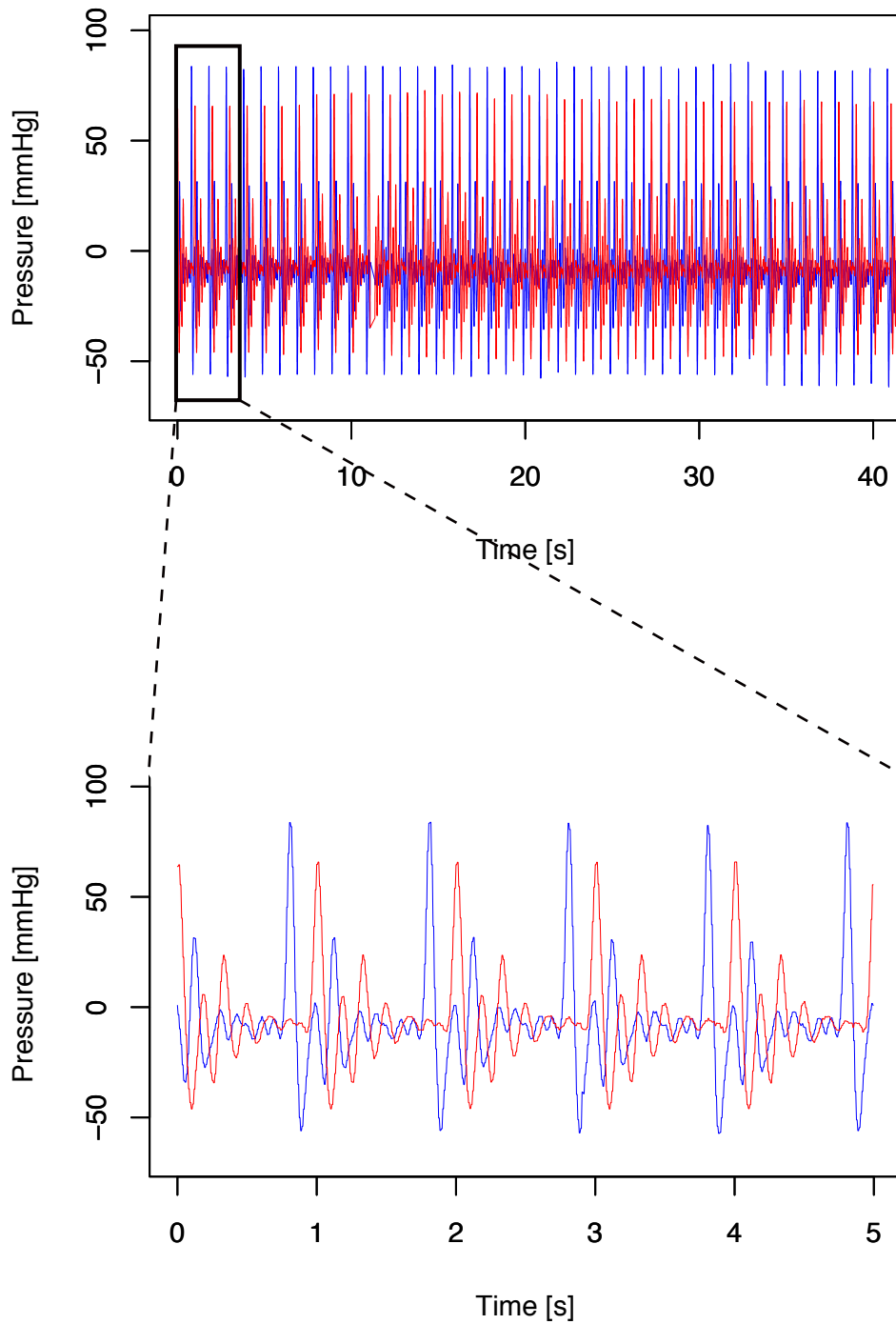


Figure 16 : Pressure P2 measured before and after the FDS deployment with aneurysm A.

The charts show the Pressure P2 measured in the hydraulic circuit during the experiment 1 (blue curve) and the experiment 2 (red curve), namely before and after the FDS deployment respectively. The experiments 1 and 2 lasted 60 seconds. Only 40 and 5 cycles were represented respectively in this figure for a better readability. The P2 pressures before and after the endovascular treatment were significantly different.

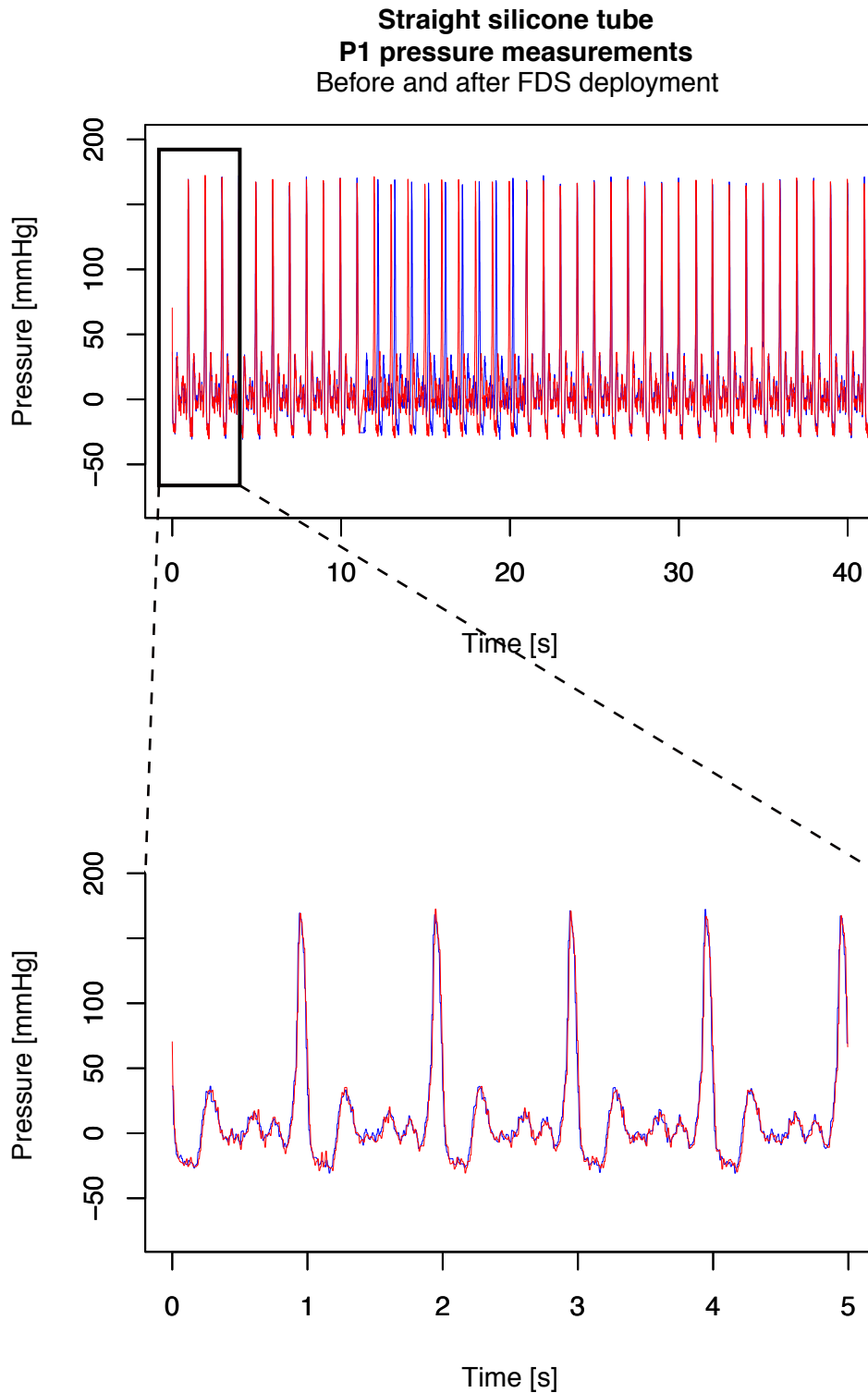


Figure 17 : Pressure P1 measured before and after the FDS deployment for the straight pipe

The charts show the Pressure P1 measured in the hydraulic circuit during the experiment 3 (blue curve) and the experiment 4 (red curve), namely before and after the FDS deployment respectively. The experiments 3 and 4 lasted 60 seconds. Only 40 and 5 cycles were represented respectively in this figure for a better readability. The P1 pressures before and after the endovascular treatment were strictly identical. It supports the high reliability and the high accuracy of the cardiovascular simulator used in this work.

Straight silicone tube
P2 pressure measurements
 Before and after FDS deployment

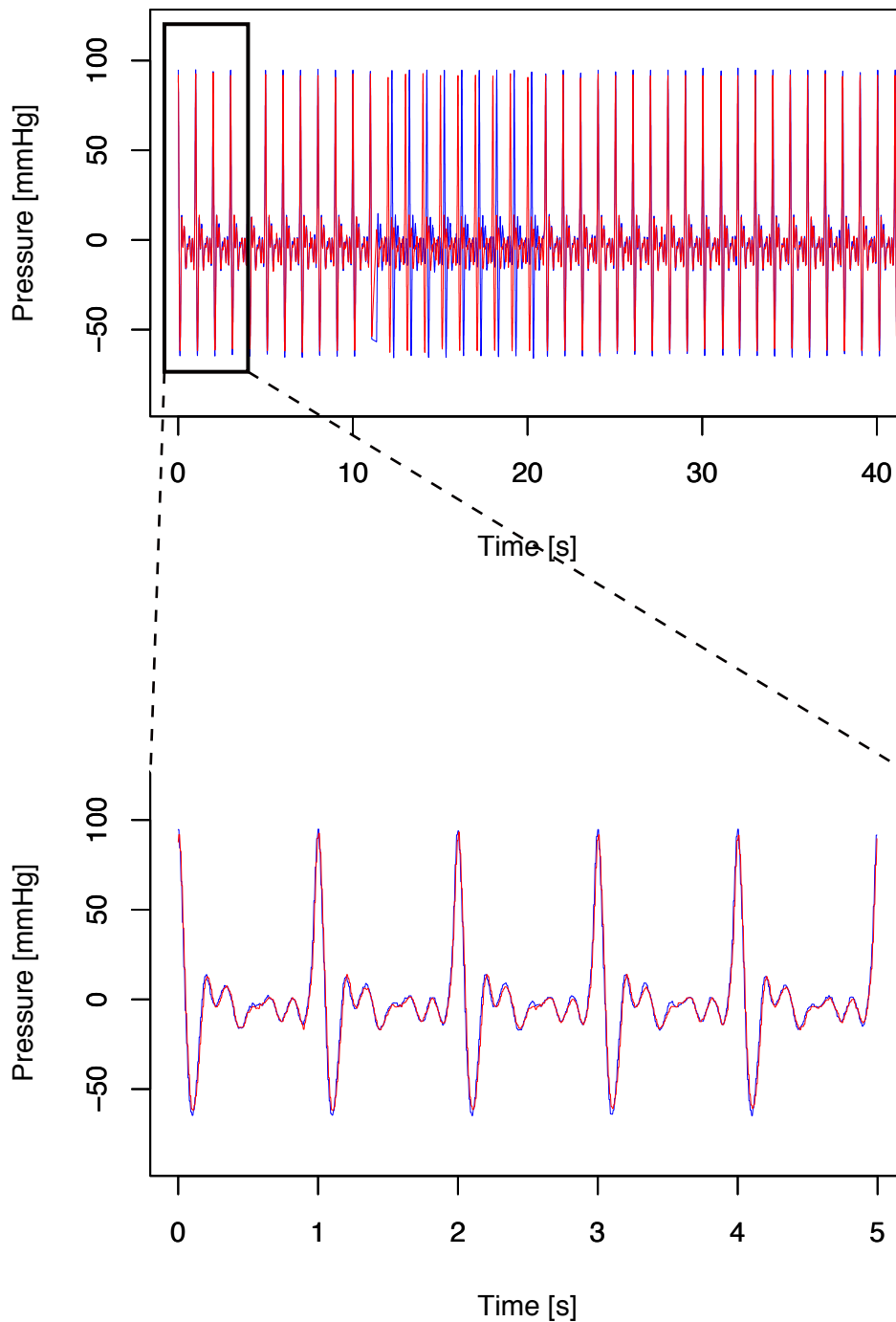


Figure 18 : Pressure P2 measured before and after the FDS deployment for the straight pipe.

The charts show the Pressure P2 measured in the hydraulic circuit during the experiment 3 (blue curve) and the experiment 4 (red curve), namely before and after the FDS deployment respectively. The experiments 3 and 4 lasted 60 seconds. Only 40 and 5 cycles were represented respectively in this figure for a better readability. The P2 pressures before and after the endovascular treatment were strictly identical. It supports the high reliability and the high accuracy of the cardiovascular simulator used in this work.

3.3.2 Intrascacular residency time of the fluid

The evolutions over the cardiac cycle of the fluid labeled by the RBCs within the aneurysmal through the $N(t)/N_0$ curve over time (i.e., the area fraction of the aneurysmal sac occupied by the RBCs) before and after the FDS (experiments 5 and 6) are reported in the Figure 19.

Before the FDS deployment (experiment 5), the $[N(t)/N_0]_{max}$ was observed at $t = 17.5$ seconds and was equal to 0.997. The fraction of the aneurysmal sac area occupied by the RBCs remained stable for 37.5 seconds around this value. The aneurysmal sac wash-out started at $t = 55$ seconds and was almost complete at $t = 77$ seconds with a $[N(t)/N_0]_{t=77}$ value of 0.05. It corresponded to a wash-out of the aneurysmal sac in approximately 22 seconds.

After the FDS deployment (experiment 6), $[N(t)/N_0]_{max}$ was observed at $t = 25$ seconds (7.5 seconds later than in Experiment 5) with a value of 0.980. The fraction of the aneurysmal sac area occupied by the RBCs was maintained around this plateau value for 25 seconds. At $t = 45$ seconds, a very slow and moderate wash-out of the aneurysmal sac began. At the end of the experiment at $t = 90$ seconds, the aneurysmal sac still showed a large amount of RBCs with a $[N(t)/N_0]_{t=90}$ value of 0.795. More than 79% of the sac was still occupied by RBCs (or 21% of RBCs was washed-out), while the parent vessel was completely washed-out.

Indirect quantification of the fluid movements between the aneurysmal sac and parent vessel showed NMRT values of 0.5859 s^{-1} and of 0.7581 s^{-1} before and after the FDS deployment.

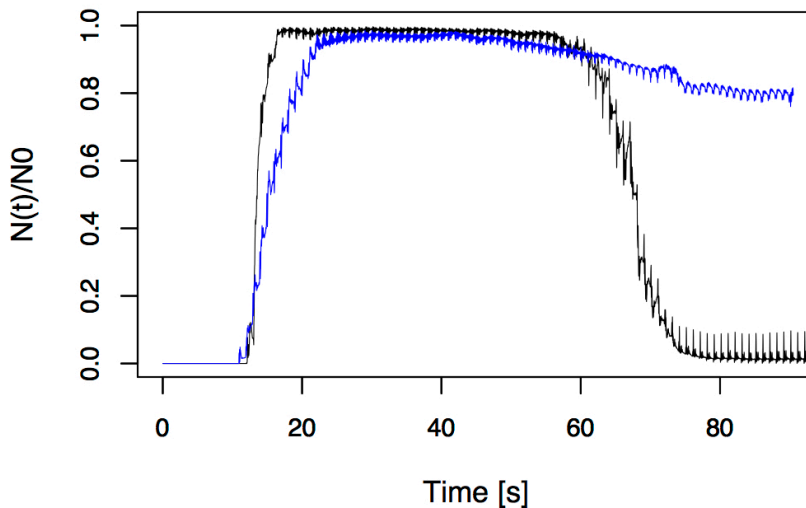


Figure 19 : area fraction of the aneurysmal sac occupied by the RBCs over time.

The graph shows the evolution of the $N(t)/N_0$ over the time before the FDS deployment (black curve) and after the FDS deployment (blue curve). The experiments lasted 90 seconds. After the FDS deployment, the saccular RBCs wash out was only of 21% (blue curve). The evolutions over time of the aneurysmal sac fractions occupied by RBCs before and after the SFD deployment show a significant decrease in the fluid movements between the parent artery and the aneurysm and a significant stagnation of the efluid within the aneurysmal sac.

3.4 Discussion

In this part of our work, we investigated the *in vitro* effect of the aneurysm on the flow in the hydraulic circuit (containing the parent vessel) using a cardiovascular simulator and a patient-specific silicone aneurysm models. Comparable experiments were conducted with a straight pipe instead of an aneurysm model as control condition. Two main results were observed. First, the resistance of the tested hydraulic segment containing the aneurysm increased significantly after the FDS deployment compared to that observed before. Whereas the resistance of the tested hydraulic segment containing the “straight pipe” as control condition remained unchanged after the FDS deployment compared to that observed before. Second, the FDS deployment within the parent vessel in a spherical model of aneurysm decreased the fluid movements between the parent vessel and the aneurysm.

Our work included measurements of the pressures upstream and downstream to the aneurysm and the calculation of the resistance of the circuit between the two measurement points, and thus on a long segment of the hydraulic circuit (0.83m) including the aneurysm and its parent vessel or the “straight pipe” (segment H, distance 0.15m). So, the observed changes concerned the overall resistance of the hydraulic circuit between the two measurement points and not only the aneurysm and its parent artery. However, in the hydraulic circuit, only the H segment was modified between the different experiments. In particular, within this H segment only the presence or absence of the FDS within the parent artery or the “straight pipe” changed the circuit between the experiments 1 and 2, and between the experiment 3 and 4 respectively. Therefore, it seems reasonable to attribute the changes of pressure P2 and the changes of the resistance in the hydraulic circuit observed between experiments 1 and 2 to the presence of the FDS at the location of the aneurysm. Since we did not perform any experiment with solely a parent vessel with a strictly identical geometry to that of the parent vessel in the model used (aneurysm model A), we reproduced similar experiments with a straight tube of silicone as control condition to assess the specific effect of the FDS deployment on the resistance of the hydraulic circuit independently from the effect of the aneurysm. Indeed, the FDS are known to allow the geometric reconstruction of the parent artery. The control experiments (3 and 4) showed no significant variation of the hydraulic resistance due to the FDS deployment in the straight tube. Therefore, these first result suggest that the aneurysm would impact the hydraulic system (and therefore the parent vessel) by decreasing its resistance. From a conceptual point of view, the aneurysm may be considered as a resistive object with a relatively low impedance compared to the resistance of the hydraulic circuit. Treatment with FDS allows for correction of this effect on the circuit by significantly increasing its resistance.

We have tested only a single aneurysm model and its parent vessel because of the significant cost and limited silicone aneurysm models available. Thus, our work does not allow to precisely characterize the resistance drop of the hydraulic circuit caused by the aneurysm according to its geometry or those of the parent vessel. Besides, the silicone model and real intracranial arteries have very different mechanical properties. In particular, the arteries present a capacitance whereas that of the silicon model is negligible. Therefore, we assume that in our experimental set up the resistance change can be imputed only to the geometrical change induced by the malformation and corrected by the FDS. If we consider the aneurysm as a resistance in a hydraulic circuit under laminar flow condition (as *in vivo* vascular network), according to equation (15) the decrease of the resistance related to the aneurysm should be inversely proportional to the size of the aneurysm (more precisely, inversely

proportional to the power of fourth of its radius). Indeed, the aneurysm is a pathological expansion of the parent vessel wall and so it can be considered from a strictly morphological point of view as an increase of its radius (or diameter). Further *in silico* studies with different aneurysm models and flow conditions are needed to confirm our results and characterize more precisely the resistance drop.

Secondly, the injection of a RBC mixture allowed to measure indirectly the effect of the FDS deployment on the fluid movement between the parent vessel and the aneurysmal sac. The analysis focused on an original approach based on a 2D high resolution image segmentation and the calculation of a parameter characterizing the residency of the RBCs within the aneurysmal sac: the NMRT. The latter was calculated before and after the FDS deployment in the aneurysm model B. The study showed the increase of the fraction of the aneurysmal sac occupied by RBCs, followed by its decrease to near zero in the experimental condition without the FDS deployment. After the FDS deployment, the RBCs wash-out from the aneurysmal sac was significantly decreased with a high amount of RBCs (79%) still present in the sac at the end of the experiment. NMRT increased after the stent deployment and it was probably underestimated. This underestimation is due to the limited duration of the experience. The movement of fluid between the parent vessel and the aneurysm are indirect evidence of the flow change in the parent vessel. One can reasonably assume that the volume of fluid entering the aneurysm is subtracted from the volume of fluid within the parent vessel at the entrance into the aneurysm. Inversely, the volume of fluid leaving the aneurysmal sac is added to the fluid volume within the parent vessel at the output of the aneurysm. The FDS significantly reduced these fluid movements. Therefore, they might have limited the flow disturbances induced by the aneurysm within the parent vessel. Our work allowed a semi-quantification of this mechanism by a 2D analysis.

We opted for a simplistic and indirect approach to highlight these fluid exchanges between the parent vessel and the aneurysm sac. A precise, three-dimensional quantification of these exchanges of fluids between the aneurysm and the parent vessel on realistic models has not been undertaken in this work for a number of methodological reasons. A complex morphology of the aneurysm is associated with complex intrasaccular flows whose study is in itself a work and beyond the scope of this thesis. Similarly, the use of 3D images would have required the development of 3D segmentation tools that would probably have been more demanding in terms of material resources (among other things, computing skills and resources) and more time consuming for the image post processing. The measurement of the flow changes induced by the aneurysm within the parent vessel by one (or more) flowmeter(s) facing the malformation was in practice not possible with the configuration of our test bed. One flowmeter was used and positioned downstream to the aneurysm. The flowmeter requires its positioning on a straight segment of the pipe on a minimum length of 10 mm. Moreover, the size of the flowmeter would have probably modified the geometry of the parent vessel with an impact on the measurement.

The impact of the aneurysm geometry on the distribution of the labeled fluid (with RBCs) has not been studied. Only one silicone simplified aneurysm model (model B) was tested. Consequently, only one surface of the aneurysmal sac (corresponding to an aneurysmal volume of 421 ml) has been tested, limiting the scope of our results. A 3D analysis and the tests of different aneurysms and parent vessel morphologies should allow us to have a better understanding of the FDS action on the parent vessel and aneurysm interactions. Further studies are needed to fully clarify the effect of these endovascular prosthesis.

3.5 Conclusion

This experimental work by using a cardiovascular simulator and silicone aneurysm models suggests that the aneurysm, which may be regarded simplistically as a dilatation of the diseased artery, would act by decreasing the resistance of the hydraulic circuit, and therefore of the parent vessel. Deploying a FDS induces the increase of the resistance in the hydraulic circuit and thus the correction of this effect of the aneurysm. The corrective effect of the FDS can be reasonably attributed to its ability to the restore a normal parent vessel geometry by reducing its diameter (i.e., a “morphological reconstruction”). Secondly, the FDS decreased also the fluid movements between the aneurysm and the parent vessel. This latter feature of the FDS might also contribute to its corrective effect by decreasing the flow modification induced by these fluid movement (i.e., “hemodynamic reconstruction”).

CHAPTER 4

4 Aneurysm and parent vessel : an *in vivo* study of flow rates, pulsatility and resistance

4.1 Introduction

The previous experiment conducted *in vitro* clearly demonstrated a significant effect of the aneurysm on its parent artery flow condition. It seemed to decrease the hydraulic resistance of the circuit. The FDS deployment corrected this effect probably by decreasing the diameter of the diseased arterial segment (i.e., a “morphological reconstruction”) and by limiting considerably the fluid movements between the aneurysm and the parent artery (i.e., “hemodynamic reconstruction”).

In this part of our work, we investigated the impact of the aneurysm on the parent vessel hemodynamic *in vivo* by following a group of patients treated for IAs by FDS. Because it is difficult to measure directly one of the parameters of pressure, volume flow or arterial resistance *in vivo*, we opted for blood velocity and flow rate measurements in the ICA by 2D PC-MRI. From the segmented ICA, mean blood flow curves were extracted and analyzed.

The ability of arterial compliance modifications, which is related to the status of the vasculature to alter the volumetric flow rate (VFR) waveforms over the cardiac cycle is well known¹⁰¹. This may be of important interest for characterization of pathologic conditions. Some authors have proposed to assess the changes in VFR waveforms as a marker of diseases^{102,103}. According to them, the evaluation of the VFR waveform of the parent vessel (i.e. ICA) could be of important value for the understanding of many diseases, such as IAs. Since PC-MRI is recognized to be an accurate and reliable non-invasive technique for velocity quantification in intracranial vessels^{55,104}, several authors have suggested the production of archetypal VFR waveforms in the ICA tree using this technique¹⁰⁵. Using quantitative flow MRI, Gwilliam et al. proposed an original approach to assess the hemodynamic changes on the carotid tree by the production of an average VFR waveform based on the averaging of identified key features of each waveform across subjects and by the computation of a pulsatility index (PI) derived from Doppler’s ultrasound technique¹⁰². The authors suggested that the analysis of the VFR waveforms over the cardiac cycle in the extracranial ICA might allow the monitoring or the screening of the cerebral aneurysms, similar to the one proposed for abdominal aortic aneurysms¹⁰⁶. The work of Gwilliam et al. established the method of waveform characterization adopted in this study.

4.2 Materials and methods

4.2.1 Patient and control groups

Ten patients with UIA selected for FDS implantation were prospectively recruited in our institution. The indication for FDS implantation was posed after a multidisciplinary meeting in our institution for all patients. Of these, seven were women. The range of patient’s age was

32 to 87 years resulting in a median age of 66 years with an interquartile range of 55 to 73 years. Aneurysms were located on the ICA from the carotid siphon to its termination. Ten healthy volunteers were also enrolled as a control group. Of these, five were women. The healthy volunteers were aged from 22 to 55 years resulting in a median age of 29 years with an interquartile range of 25 to 39 years. The ethics committee guidelines were followed for this study (DGRI CCTIRS MG/CP 2012.528 ; Ethics Committee of University Hospital of Lyon ; Lyon / France). The informed consent was obtained from all patients and volunteers. Image-data from these two groups was used for analysis. Five patients with no medical history were symptomatic because of the aneurysm's mass effect at the cavernous portion of the ICA. They presented with cavernous sinus syndrome associating headaches, ipsilateral ptosis and ophtalmoplegia due to third, fourth or sixth nerves palsy, without any visual acuity decreasing or pupillary abnormality. Two patients presented headaches without any obvious relationship to their aneurysms. One asymptomatic patient presented a medical history of high blood pressure, cigarette smoking and hypercholesterolemia. One healthy volunteer presented a medical history of cigarette smoking. All other patients and control subjects did not present any symptoms or medical history, and specially, any vascular steno-occlusive lesion of the supra aortic trunks or intracranial arteries.

4.2.2 Aneurysm population : endovascular treatment and morphological analysis

All patients were treated under general anesthesia by using a biplane angiographic system (ALLURA, Philips, Best, Netherland) after a preparation according to our institutional protocol (loading dose of 300mg of clopidogrel administrated one day before the EVT; systemic heparinization during the endovascular procedure, stopped at the end of the treatment; double antiplatelet therapy initiated for six months at day one after the treatment, with 75mg of acetylsalicylic acid and 75mg of clopidogrel / day). A 3D rotational angiography of the aneurysm and parent vessel was performed before the treatment allowing for 3D reconstructions and the treatment planning. One or more FDS were deployed in one session according to the aneurysm's neck size (PIPELINE[®], ev3-COVIDIEN, Irvine, CA, USA).

3D aneurysms and parent vessel geometries were segmented and reconstructed from the performed 3D angiographic acquisitions (spatial resolution $0.48 \times 0.48\text{mm}^2$) by using a new ACM dedicated to the near real time segmentation of 3D objects based on the level-set method¹⁰⁷. It allowed the calculation of the maximal diameter (mm), depth (mm), neck size (mm), volume (i.e., volume of the patent intrasaccular lumen; mm^3) and aspect ratio values of all aneurysms using dedicated software (ITK-SNAP, Penn Image Computed and Science Laboratory, University of Pennsylvania, USA).

4.2.3 MRI examinations including 2D PC-MRI

All patients underwent MRI examinations using a clinical system operating at 3 Tesla with 32-Channel Array Head-Neck coil before and within the three days following the EVT according to the MR scan availability in our institution (3 Tesla, 45 mT/m, 200 T/m/s, Skyra, SIEMENS, Erlangen, Germany). After 1 month, an additional follow-up MRI examination was performed. To visualize the circle of Willis (CoW), a 3D time-of-flight MRA (3D TOF-MRA) was performed (149 slices ; TR/TE 21/3.4 ms ; 18° flip angle ; 0.6mm section thickness ; in-plane resolution $0.27 \times 0.26\text{mm}^2$). Maximum intensity projections derived from the resultant 3D TOF-MRA dataset were used to define the placement of each two-

dimensional slice to be used for quantitative flow estimation. 2D PC-MRI scan slices were performed at target points in the ICA upstream (extracranial) and downstream (intracranial) to the aneurysm, respectively (one slice ; TR/TE 180.5/10.5ms ; 7.5° flip angle; 3.1mm section thickness ; 0.31×0.31mm² interpolated in-plane resolution ; 37.6-41.2 msec temporal resolution). The phase contrast sequence consisted of a K-space segmented 2D radio frequency-spoiled gradient echo sequence with prospective ECG gating (283 phase encoding steps ; 1 view per segment). It resulted in 283 acquired cardiac cycles for one phase-contrast measurement. Data acquisition resulted in a series of 2D slices representing 2D blood flow through the slice of acquisition in consecutive timeframes within the cardiac cycle. Thereby, the number of frames varied with the patient's individual heart rate. The number of measurement points over the cardiac cycle varied from 20 to 32 with a temporal resolution of 37.6 - 41.2 ms (temporal resolution was defined as following = RR interval/number of frames). Special care was taken to reduce the angulation error risk of the scan planes regarding to the axis of blood flow by ensuring that the 2D pc-MRI slices were placed orthogonal to the long axis of the vessel of interest and therefore to the direction of blood flow. Thus, upstream and downstream scan planes were placed 1) at the sub- or intra-petrous level of the ICA and at its intracranial terminal level, respectively, 2) on relatively long and straight segments and 3) before the posterior communicating artery, as illustrated in Figure 20. The part of the blood flow for the ophtalmic artery and small branches of carotid siphon was considered as negligible given their size compared to that of the ICA. Similarly, in the control group, the scan planes were placed as previously described at comparable locations on the ICA. An appropriate velocity-encoding factor was chosen by the operator based on previous experience and defined as to result in images with significant contrast between the stationary tissue and flowing blood with the lowest wrap-around artifacts. Typical settings were 80cm/sec for the upstream measurements and 110cm/sec for the downstream measurements. The same couple neuroradiologist and technologist imaged all patients and volunteers to minimize the scan set-up variability. With the comfort of the patient in mind, the scans were kept within 20 minutes, including the 3D TOF-MRA and the two 2D pc-MRI acquisitions.

4.2.4 Image post-processing

4.2.4.1 Segmentation of the 2D PC-MRI

Data of quantitative flow MRI were analyzed with a home-developed post-processing tool specifically developed for this study with MATLAB software (R2014a Student version 8.3.0.532, The MathWorks, Inc., Natick, Massachusetts, United States). Blood velocities were extracted by a ROI analysis from the phase difference images of the flow measurements. The arterial lumen boundaries were semi-automatically segmented from the surrounding stationary tissue by using the ACM-CV (described later in Chapter 5, § 5.1.1) allowing segmentation without an applied edge on all images during the cardiac cycle⁸⁰. In case of vessel motion through the 2D pc-MRI slice, due to superadded motion of the CoW at intracranial level, a manual segmentation of the arterial lumen over the cardiac cycle was performed by an experienced neuroradiologist. The software allowed for an automated extraction of mean blood velocities (MBV in cm.s⁻¹), vessel area (mm²) within the analyzed slice of the vessel for each time-point over a cardiac cycle. Volumetric blood flow rates (VBFR in mm³.s⁻¹), in and its waveforms were computed by integrating over time MBV within the region of interest that enclosed the vessel lumen closely.

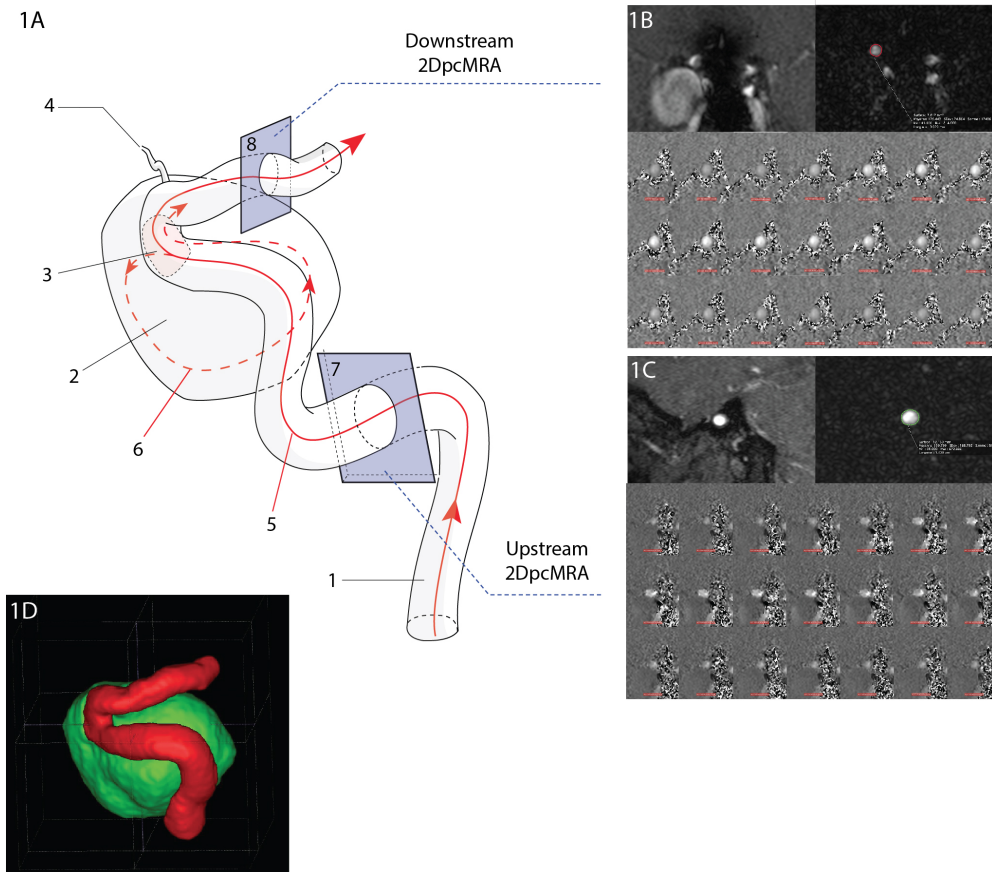


Figure 20 : The 2D PC-MRI slices upstream and downstream to the aneurysm

A: 1= Internal carotid artery, 2= aneurysmal sac, 3= aneurysmal neck, 4= ophthalmic artery, 5= parent vessel blood flow direction, 6= Intrasaccular blood flow direction, 7= Upstream. The 2PC-MRI acquisition plans were placed as shown on the figure A. The upstream slice was placed orthogonal to the flow direction on the intrapetrous (or sub-petrous) segment of the ICA. The downstream segment was placed orthogonal to the flow direction on its termination. They enabled the imaging of the ICA flow upstream (C) and downstream to the aneurysm. The picture D shows the 3D reconstruction of the aneurysm.

4.2.4.2 Extraction of the volumetric flow rate waveform features

The method of feature extraction and normalization mirrors that of Gwilliam et al. adapted from that of Ford et al.^{102,103}. The total flow values at each location were analyzed using the MATLAB software (R2014a Student version 8.3.0.532, The MathWorks, Inc., Natick, Massachusetts, United States). A semiautomated algorithm was used to identify the key points on the waveform. The points M0, P1, M1, P2, M2, and P3 were noted manually. The global peak, P1, was used as the initial feature point. Working backwards from P1, the point M0 corresponded to the point at which the gradient first changed sign and was defined as time 0. Working forwards from P1, the point where the gradient first changed sign was considered as M1. Similarly, points P2, M2 and P3 were identified. Points H0, H1, H2 and H3 were identified using an automated algorithm that linearly interpolated from the original waveform to find the time to the associated half peak from the associated local minima and peak. Points D1 to D3 were spaced equally between P3 and D4, D4 being the final point in the waveform. Splines were then fitted to the data to produce characteristic waveforms. An average

waveform for each measurements points on the ICA was produced by taking the mean of feature points, both their magnitude and time, and a spline was fitted in similar manner. Each waveform was normalized by dividing each by its mean and by dividing each time points by taking the time taken to complete a cardiac cycle for each waveform. As described by, Gwilliam et al., this feature-based approach minimizes the attenuation of more local minima and maxima, which can vary in time between subjects ¹⁰². The data was presented by graphical representations of VFR waveform over a cardiac cycle as illustrated in Figure 21 (from the original publication of Gwilliam et al. ¹⁰²).

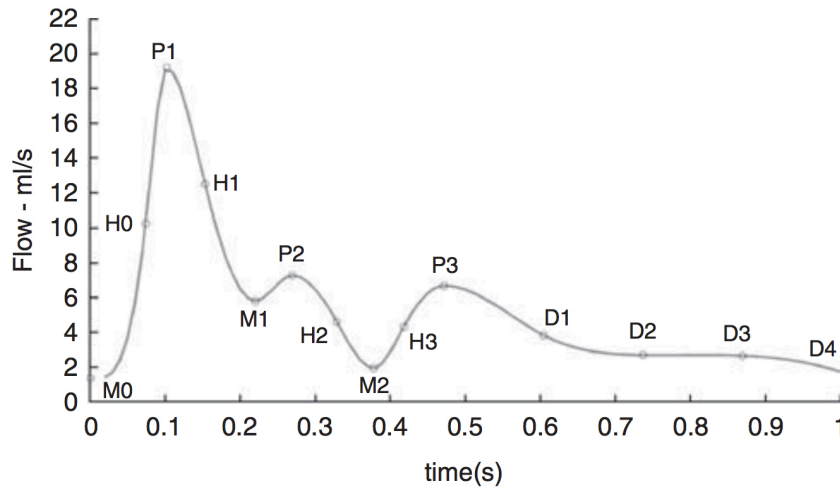


Figure 21 : VFR waveform features of the ICA over a cardiac cycle

The VFR waveform of the ICA blood flow from the original publication of Gwilliam et al ¹⁰². The key points M0, P1, M1, P2, M2, and P3 were noted manually. The global peak, P1, was used as the initial feature point. Working backwards from P1, the point M0 corresponded to the point at which the gradient first changed sign and was defined as time 0. Working forwards from P1, the point where the gradient first changed sign was considered as point M1. Similarly, points P2, M2 and P3 were identified. Points H0, H1, H2 and H3 were identified using an automated algorithm that linearly interpolated from the original waveform to find the time to the associated half peak from the associated local minima and peak. Points D1 to D3 were spaced equally between P3 and D4, D4 being the final point in the waveform.

4.2.4.3 Statistical analysis

The Mann-Whitney-Wilcoxon’s Rank test was used to compare the ages of the two analyzed groups. A Chi Square test with a correction of Yates was used to compare both groups regarding the cardiovascular risk factors. A quantitative assessment of the waveforms was performed through the computation of a resistive index (RI) and pulsatility index (PI) adapted from the indexes used in Doppler ultrasound for the characterization of velocity waveforms ¹⁰⁸, as follows:

$$RI = (Q_{max} - Q_{min})/Q_{max} \quad \text{Equation 20}$$

$$PI = (Q_{max} - Q_{min})/Q_{mean} \quad \text{Equation 21}$$

Where Q_{max} is the maximum flow rate in the waveform (at systolic peak), Q_{min} is the minimum flow rate in the waveform (at tediastole), and Q_{mean} is the mean flow rate in

waveform (area under the curve). Since the *RI* and *PI* in ICA might be affected by the age or some pathological conditions of the patients^{56,109}, such as high blood pressure, the effect of the aneurysm on the parent vessel hemodynamic was assessed through the computation of the *Rlratio* and *Plratio* values, as follows:

$$RI\ ratio = (RI\ downstream)/(RI\ upstream) \quad \text{Equation 22}$$

$$PI\ ratio = (PI\ downstream)/(PI\ upstream) \quad \text{Equation 23}$$

Results are expressed as median (25%-75% interquartile). The *Rlratio* and *Plratio* values in both patient and control groups, and within patient group before the EVT, after the EVT and at follow-up were assessed using a Student's t-test or a Mann-Whitney Rank Sum test when needed according to the results of the Shapiro-Wilk normality test. The Spearman's Rank correlation test was used to analyze the correlation between the *Plratio* values and the aneurysm volumes and aspect ratio values, respectively. The Kruskal-Wallis Rank Sum Test and the Mann-Whitney Rank Two-sided Test were used to compare the VFR (in $\text{mm}^3 \cdot \text{s}^{-1}$) in the patient group at each time points, and between patient and control group. A P value of less than .05 was considered to indicate a significant difference. The statistical analysis was performed with SigmaPlot software (Systat Software[®], San Jose, CA).

4.3 Results

The mean ages were of 63.8 ± 16 years old in patient group and of 32.6 ± 11 years old in control group, with a significant difference ($P < 0.001$). Both groups did not show any significant statistical difference regarding the cardiovascular risk factors ($P = 0.57$).

4.3.1 Aneurysms characteristics and treatment details

Table 2 summarizes the morphological characteristics of the aneurysms and the number of implanted FDS. Five aneurysms were located on the right side. The aneurysms were located at the C2 segment ($n=4$), the C3 segment ($n=3$) and C4 segment ($n=3$) of the carotid siphon according to the Fisher's classification of ICA segments. All aneurysms were saccular and two of them presented an intraluminal partial thrombosis. The median aneurysm volume was 2068 mm^3 ($698\text{-}3590\text{mm}^3$), the median maximal diameter was 19 mm ($10.8\text{-}22.3\text{mm}$), the median neck size was 6.5 mm ($5.7\text{-}11.9\text{mm}$), the median depth was 14.2 mm ($11.4\text{-}17.5\text{mm}$) and the median aspect-ratio value was 1.76 ($1.39\text{-}1.93$).

The EVT were successfully performed in 9/10 patients by deployment of one FDS ($n=6$), two FDS ($n=1$) and 3 FDS ($n=2$) depending on the width of the neck and the patient's anatomy. Because of anatomical difficulties, patient 8 could not be treated by FDS and was scheduled for a parent artery occlusion. The patient contributed only to the pre-EVT analysis. No complication occurred during or immediately after the treatment, nor during the hospitalization period.

N	Aneurysm Location*	Diameter (mm)	Neck size (mm)	Depth (mm)	Volume (mm ³)	Aspect-Ratio	Shape / Partial thrombosis	Number of implanted flow diverter stents
1	Left C2 segment	12.2	6.5	12.2	984	1.88	Saccular / Regular	1
2	Left C2 segment	4.8	2.4	3.6	55	1.5	Saccular / Irregular	1
3	Left C2 segment	10.4	5.7	11.1	603	1.95	Saccular / Regular	1
4	Left C4 segment	20.9	8.8	14.8	3648	1.68	Saccular / Regular	2
5	Right C3 segment	22	5.7	17.3	3417	3.04	Saccular / Regular	1
6	Right C4 segment	17.1	12.9	17.6	1817	1.36	Saccular / Regular	3
7	Left C2 segment	5.9	3.7	6.8	118	1.84	Saccular / Regular	1
8	Right C3 segment	25.4	20	23	6735	1.15	Saccular / Regular / Part. thrombosed	0
9	Right C3 segment	30.1	6.5	20	4888	3.08	Saccular / Regular / Part. thrombosed	1
10	Right C4-C3 segments	22.4	13	13.7	2319	1.05	Saccular / Regular	3
Median (25%-75% IQ)		19 (10.8-22.3)	6.5 (5.7-11.9)	14,2 (11.4-17.5)	2068 (698-3590)	1.76 (1.39-1.93)		

* Aneurysm location according to Fisher's segmental classification of the ICA. C2: ophtalmic segment of the ICA; C3: anterior genu of the siphon; C4: intracavernous segment.

Table 2 : Morphologic characteristics of the aneurysms in patient group

4.3.2 2D PC-MRI of the ICA

Before EVT, the 2D pc-MRI studies were successfully performed for all volunteers and patients (40/40; 100%). After the EVT, 2D pc-MRI was successfully performed in 17/18 acquisitions (94%) for the nine treated patients, at 6 hours (n=4), one day (n=1) and three days (n=4) after the endovascular procedure. The follow-up MRI examinations after one month were successfully performed between 1 to 12 months (median of 1 month; interquartile range of 1 to 3 months) in 17/18 (94%) of the treated patients. The downstream 2D PC-MRI was not analyzable in one patient (patient 7) after the EVT and at follow-up because the MR slice could not be appropriately placed. The FDS covered the downstream point of measurement on the ICA bifurcation resulting in a decrease of 2D PC-MRI signal due to the endovascular device. All upstream 2D PC-MRI were successfully performed and analyzable (100%). A manual correction of the segmentation was needed for two patients after the EVT and at follow-up, and for one patient at follow-up (5/58= 8.6%), because of superadded motion of the measured arterial segment through 2D PC-MRI slice at downstream locations. The parent vessels were patent in all treated patients at the post-EVT and at follow-up MRI examinations.

4.3.3 Resistive and Pulsatility indexes ratios

The *RI*, *PI*, *Rlratio* and *Plratio* values in the control group and in the patient group before the EVT, after the EVT and at follow-up are reported in Tables 3 and 4. The CoW configurations, the upstream and downstream computationed VBFR before the EVT, after the EVT and at follow-up are reported in Table 5.

The distribution of the *RI*, *PI*, *Rlratio* and *Plratio* values fulfilled the normality test for both the control group and the patient group before and after the EVT and at follow-up, except for the *Rlratio* values at follow-up in patient group (P=0.03). Therefore, the mean values of *Rlratio* and *Plratio* are expressed as mean±SD except for *Rlratio* at follow-up. This latter is expressed as median and the 1st and 3rd quartiles values were also given.

The control group presented a mean *Rlratio* of 0.98±0.08 and a mean *Plratio* of 1.01±0.10.

The patient group presented:

- A mean *Rlratio* of 0.84±0.22 and mean *Plratio* of 0.83±0.26 before the EVT.
- A mean *Rlratio* of 1.02±0.12 and means *Plratio* of 0.97±0.10 after EVT.
- A mean *Rlratio* of 0.96±0.05 (median = 0.97 [0.95, 1.08]) and means *Plratio* of 0.95±0.05 at follow-up.

The *Rlratio* and *Plratio* values in the control group and in the patient group before EVT, after EVT and at follow-up were not significantly different (P=0.40 for *Rlratio* values and 0.40 for *Plratio* values).

In the patient group:

- The *Rlratio* values were significantly inversely correlated to the volumes of the aneurysms before the EVT ($R=-0.90$, $R^2=0.80$, $P<0.01$) but not to their aspect-ratio ($R=-0.36$, $R^2=0.13$; $P=0.31$). There was no correlation between the *Rlratio* values and the volumes, nor between this ratio and the aspect ratio after the EVT ($R=-0.02$, $R^2=0.00$, $P=0.96$ and $R=-0.001$, $R^2=0$, $P=0.98$, respectively), nor at follow-up ($R=0.50$, $R^2=0.25$, $P=0.21$ and $R=0.31$, $R^2=0.09$, $P=0.46$, respectively).
- The *Plratio* values were also significantly inversely correlated to the volumes of the aneurysms before the EVT ($R=-0.89$, $R^2=0.79$; $P<0.01$) but not to their aspect-ratio ($R=-0.18$, $R^2=0.03$; $P=0.63$). There was no correlation between the *Plratio* values and the volumes, nor between this ratio and the aspect ratios after the EVT ($R=-0.07$, $R^2=0.00$, $P=0.86$ and $R=-0.41$, $R^2=0.17$, $P=0.31$, respectively), nor at follow-up ($R=-0.01$, $R^2=0.00$, $P=0.81$ and $R=-0.33$, $R^2=0.11$, $P=0.42$, respectively).

These results are illustrated in the Figures 22 and 23.

Retrospectively, by analyzing the values of the *Rlratio* and *Plratio* for each patient before EVT, two subgroups of patients could be identified according to whether their *Rlratio* and *Plratio* values before the EVT were significantly decreased or not compared to those of the control group.

Five patients (subgroup A; mean age of 64.4 ± 11.4 years old) presented mean *Rlratio* and *Plratio* values of 1.03 ± 0.04 and 1.06 ± 0.07 , respectively, before the EVT, which was not statistically different from that in the control group ($P=0.31$ and $P=0.79$, respectively). They presented mean *Rlratio* values of 0.94 ± 0.06 and 1.01 ± 0.08 after EVT and at follow-up respectively, without any significant difference with the values before EVT and that of the control group ($P=0.43$). This subgroup presented mean *Plratio* values of 0.95 ± 0.03 and 1.00 ± 0.14 after EVT and at follow-up, respectively, without any significant difference with the values before EVT and that of the control group ($P=0.58$). None of these patients were symptomatic because of their aneurysms.

A second group of five patients (subgroup B; mean age of 63.2 ± 21 years old) presented mean *Rlratio* and *Plratio* values of 0.65 ± 0.12 and 0.61 ± 0.14 , respectively, before the EVT, which was significantly different from that in the control group ($P<0.001$ and $P<0.001$, respectively). They presented mean *Rlratio* values of 0.97 ± 0.05 and 1.04 ± 0.16 after EVT and at follow-up respectively, without any significant difference compared to that of control group ($P=0.61$). These values were significantly different from the mean *Rlratio* before EVT ($P=0.004$). This subgroup presented mean *Plratio* values of 0.95 ± 0.07 and 0.94 ± 0.33 after EVT and at follow-up, respectively, without any significant difference compared to that of control group ($P=0.33$). These values were significantly different from the mean *Plratio* before EVT ($P<0.001$). All the patients in this subgroup were clinically symptomatic because of their aneurysm. They presented with a mass effect of their aneurysm at the cavernous portion of the ICA (cavernous sinus syndrome).

N	Before the EVT			After the EVT				At Follow-Up > 1 month			
	Upstream RI	Downstream RI	RI-ratio	Date	Upstream RI	Downstream RI	RI-ratio	Date	Upstream RI	Downstream RI	RI-ratio
Patient 1	0.413	0.414	1.003	D3	0.557	0.526	0.944	M1	0.556	0.522	0.937
Patient 2	0.554	0.543	0.981	D0	0.624	0.605	0.969	M12	0.544	0.583	1.073
Patient 3	0.430	0.467	1.087	D1	0.572	0.571	0.998	M11	0.596	0.570	0.956
Patient 4	0.515	0.534	1.038	D3	0.554	N/A	N/A	M3	0.549	N/A	N/A
Patient 5	0.469	0.277	0.590	D0	0.484	0.443	0.914	M1	0.556	0.537	0.965
Patient 6	0.623	0.484	0.777	D3	0.544	0.569	1.046	M1	0.600	0.586	0.977
Patient 7	0.702	0.540	0.768	D0	0.655	0.624	0.952	M1	0.558	0.517	0.928
Patient 8	0.559	0.273	0.488	N/A	N/A	N/A	N/A	N/A	N/A	N/A	N/A
Patient 9	0.598	0.370	0.619	D0	0.647	0.626	0.967	M1	0.491	0.627	1.277
Patient 10	0.581	0.598	1.029	D3	0.621	0.533	0.858	M3	0.531	0.576	1.085

Control 1	0.554	0.544	0.981
Control 2	0.504	0.498	0.988
Control 3	0.436	0.467	1.072
Control 4	0.457	0.472	1.032
Control 5	0.448	0.402	0.898
Control 6	0.509	0.419	0.824
Control 7	0.558	0.515	0.923
Control 8	0.565	0.552	0.977
Control 9	0.555	0.594	1.071
Control 10	0.478	0.522	1.092

EVT = endovascular treatment
N/A = non available data
RI = resistive index
RI-ratio = resistive indexes ratio

Table 3 : Values of resistive index (RI) and RI-ratio.

N	Before the EVT			After the EVT				At Follow-Up > 1 month			
	Upstream PI	Downstream PI	PI-ratio	Date	Upstream PI	Downstream PI	PI-ratio	Date	Upstream PI	Downstream PI	PI-ratio
Patient 1	0.616	0.611	0.992	D3	0.896	0.881	0.983	M1	1.037	0.899	0.867
Patient 2	0.942	0.973	1.033	D0	1.162	1.141	0.982	M12	0.935	1.062	1.136
Patient 3	0.572	0.616	1.077	D1	0.904	0.829	0.917	M11	0.855	0.775	0.906
Patient 4	0.813	0.946	1.164	D3	1.029	N/A	N/A	M3	0.788	N/A	N/A
Patient 5	0.826	0.580	0.702	D0	0.814	0.779	0.957	M1	0.920	0.872	0.948
Patient 6	1.199	0.860	0.717	D3	0.781	0.823	1.054	M1	1.184	1.111	0.938
Patient 7	1.230	0.761	0.619	D0	1.079	0.966	0.895	M1	0.788	0.714	0.906
Patient 8	0.920	0.346	0.376	N/A	N/A	N/A	N/A	N/A	N/A	N/A	N/A
Patient 9	1.008	0.625	0.620	D0	1.159	1.037	0.895	M1	0.860	0.849	0.987
Patient 10	0.877	0.898	1.024	D3	0.909	0.851	0.936	M3	0.728	0.805	1.106

Control 1	0.951	0.990	1.041
Control 2	0.980	0.878	0.896
Control 3	0.750	0.824	1.099
Control 4	0.736	0.760	1.033
Control 5	0.674	0.678	1.006
Control 6	0.665	0.558	0.839
Control 7	1.079	0.976	0.905
Control 8	1.245	1.278	1.027
Control 9	0.810	0.910	1.123
Control 10	0.891	1.010	1.134

EVT = endovascular treatment
N/A = non available data
PI = pulsatility index
PI-ratio = pulsatility indexes ratio

Table 4 : Values of resistive index (PI) and PI-ratio.

The two subgroups presented mean *Rlratio* values significantly different before the EVT ($P<0.029$), but not after the treatment ($P=0.76$ after the EVT and $P=1$ at follow-up). Their mean *Plratio* values were also significantly different before the EVT ($P<0.001$), but not after the treatment ($P=0.52$). The aneurysm's volumes in subgroups A and B were significantly different ($P<0.001$), with a median aneurysm volume of 603 mm^3 (118 mm^3 to 984 mm^3) in subgroup A and 3648 mm^3 (3417 mm^3 to 4888 mm^3) in subgroup B. The ages in these two subgroups were not statistically different ($P=1$). But, in these subgroups, the patients were significantly older than the control subjects in the control group ($P<0.01$ and $P=0.01$ for subgroups A and B, respectively).

These results are illustrated by Figures 24 and 25.

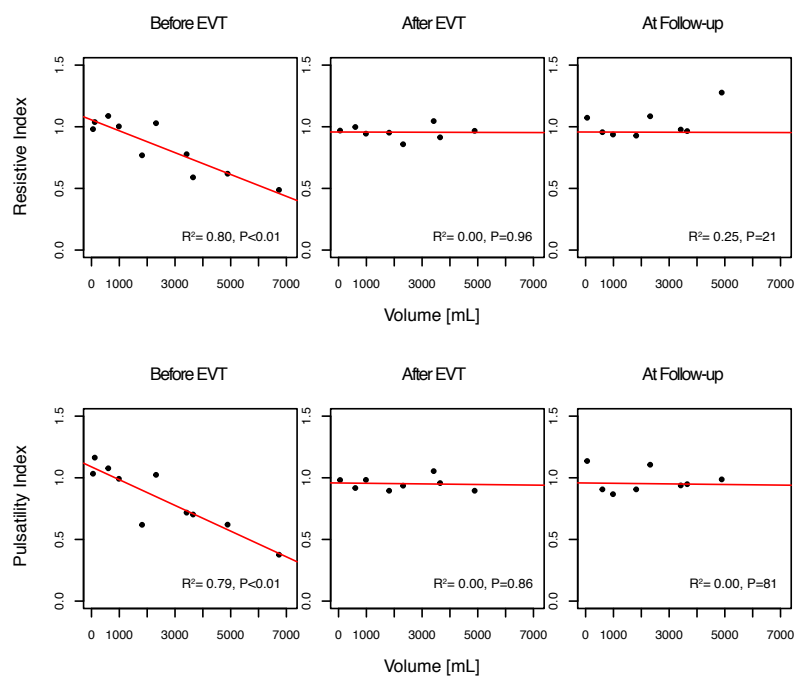


Figure 22 : Correlation analysis between RI-ratios, PI-ratios and the volumes.

The graphs represent the plot of the RI-ratio values (first row) and the PI-ratio values (second row) according to the volume of the aneurysm before EVT (first column), after EVT (second column), and at follow-up (third column). The values of the correlation coefficients R^2 and the P values are reported in each graph. The analysis and the graphs show a significant correlation between the ratios (RI and PI) and the volume of the aneurysm before EVT. After traitement endovasculaire and at follow-up there no more correlation between the ratios and the volume.

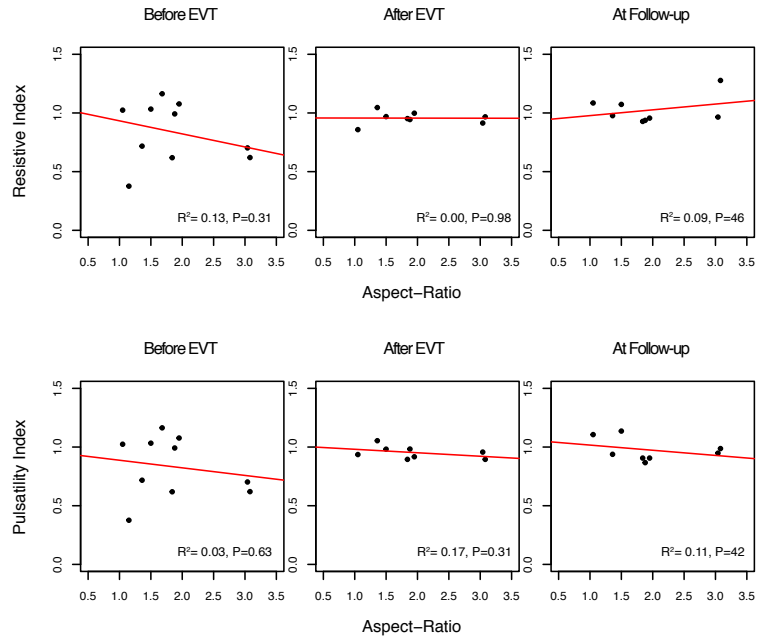


Figure 23 : Correlation analysis between RI-ratios, PI-ratios and the volumes.

The graphs represent the plot of the RI-ratio values (first row) and the PI-ratio values (second row) according to the aspect ratio of the aneurysm before EVT (first column), after EVT (second column), and at follow-up (third column). The values of the correlation coefficients R^2 and the P are reported in each graph. The analysis and the graphs show no correlation between the ratios (RI and PI) and the aspect ratio of the aneurysm.

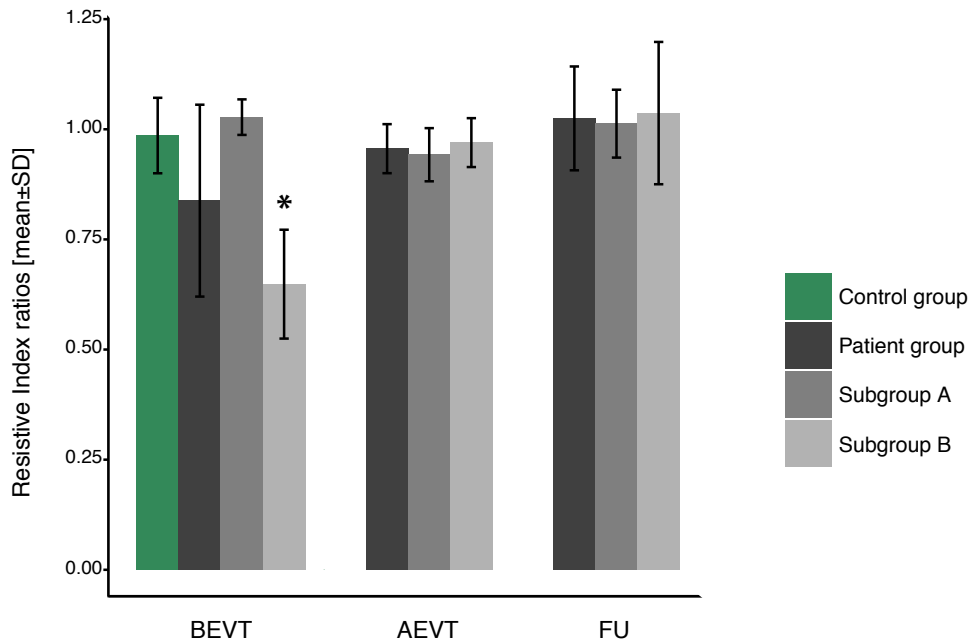


Figure 24 : Barplots of resistive index (RI) of the different groups and subgroups.

The bars represent the mean PI-ratios and their standard deviations. Before EVT, the mean RI-ratio in sibgroup B was significantly lower than that in the patient group, subgroup A and control group. After the EVT by FDS deployment, the mean RI-ratio in subgroup B increased significantly and was not statistically different than that in the patient group, subgroup A and control group.

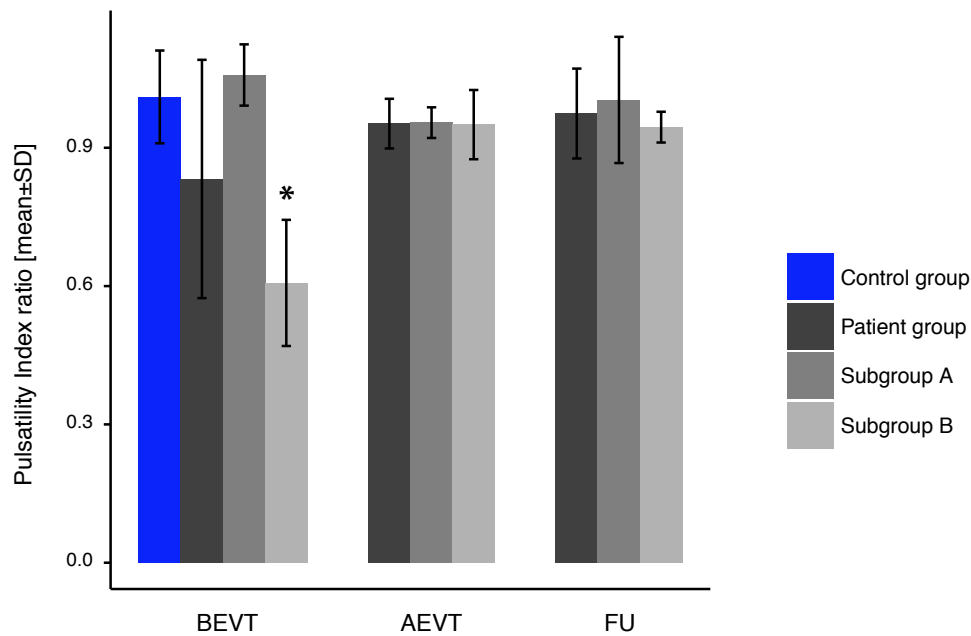


Figure 25 : Barplots of Pulsatility index (RI) of the different groups and subgroups.

The bars represent the mean PI-ratios and their standard deviations. Before EVT, the mean PI-ratio in subgroup B was significantly lower than that in the patient group, subgroup A and control group. After the EVT by FDS deployment, the mean PI-ratio in subgroup B increased significantly and was not statistically different than that in the patient group, subgroup A and control group.

4.3.4 Volumetric blood flow rates

In patient group, the mean volumetric blood flow rates (mVFR) at upstream and downstream locations were 244 ± 66 mL/min and 218 ± 50 mL/min before the EVT, 259 ± 50 mL/min and 246 ± 51 mL/min after the EVT, and 259 ± 47 mL/min and 235 ± 44 mL/min at follow-up. No significant differences were observed between the upstream and downstream mVFR at each timepoints ($p=0.44$), except in two patients (patients 4 and 10). They presented an important increase of the mVFR at downstream locations compared to the upstream locations (+20% and +44%, respectively) because of heart rate increases during downstream flow measurements (76 bpm vs. 106 bpm for patient 4 and 53 bpm vs. 75 bpm for patient 10). A discomfort felt by these two patients within the MR scan explained the heart rate variations. In the control group, mVFR were 306 ± 35 mL/min at upstream location and 294 ± 40 mL/min at downstream location, without any significant difference ($p=0.24$). The mVFR were higher in the control group compared to those in patient group at both upstream and downstream locations before the EVT ($P=0.02$ and $P<0.01$, respectively). This difference was also significant after the EVT and at follow-up ($P=0.02$ and $P=0.03$ after the EVT, and $P=0.02$ and $P=0.01$ at follow-up). The configuration of the CoW and the mVFR for each patients and control subjects are reported in Appendix 1.

4.3.5 Volumetric flow rate waveforms

The normalized VFR waveforms in the control group and in the patient group before EVT are shown in Figure 26. The normalized VFR waveforms for patients in subgroup A and subgroup B before EVT, after EVT and at follow-up are shown in Figure 27. The analysis of the VFR waveforms showed moderate modifications of the flow modulation at downstream measurement point in patient group before the EVT compared to the normal modulation in the control group. These modifications did not seem to affect the upstream segment of ICA. It was mainly characterized by a moderate increase of diastolic velocities (+14% of mean flow from P3 to D4 plate) associated to a slight decrease of systolic peak (-5% at P1) compared to the upstream VFR waveform. These modifications were more pronounced in the average VFR waveform of subgroup B before the EVT, with a clear increase of the diastolic velocities (+25%), a decreased (-10%) and moderately delayed (+6% of proportion of cardiac cycle) systolic peak with attenuation of the M1 and M2 minima. The average upstream and downstream VFR waveforms after the EVT and at follow-up were comparable to those of the control group. The subgroup A presented normally modulated VFR waveforms before the EVT, after the EVT and at follow-up similar to those of the control group.

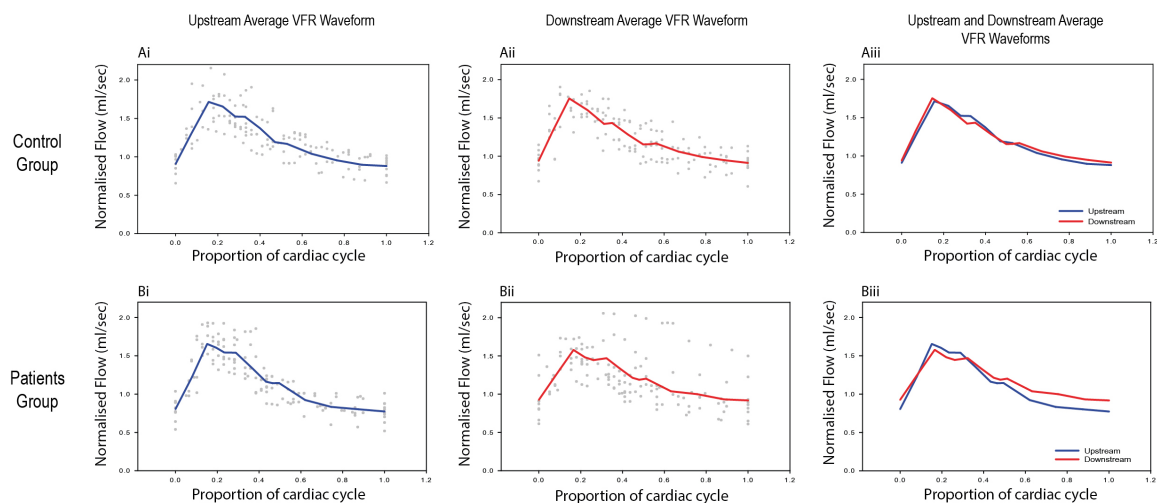


Figure 26 : Normalized VFR waveforms for volunteers group and patient group before EVT.

Mean normalized VFR waveforms at upstream (i; column 1), downstream (ii; column 2) and both upstream and downstream (iii; column 3) segments of the ICA for control group (A; row 1) and patient group (B; row 2) are represented. Features of the individual waveforms are also shown (x) for the upstream and downstream VFR waveforms (Ai, Aii, Bi and Bii).

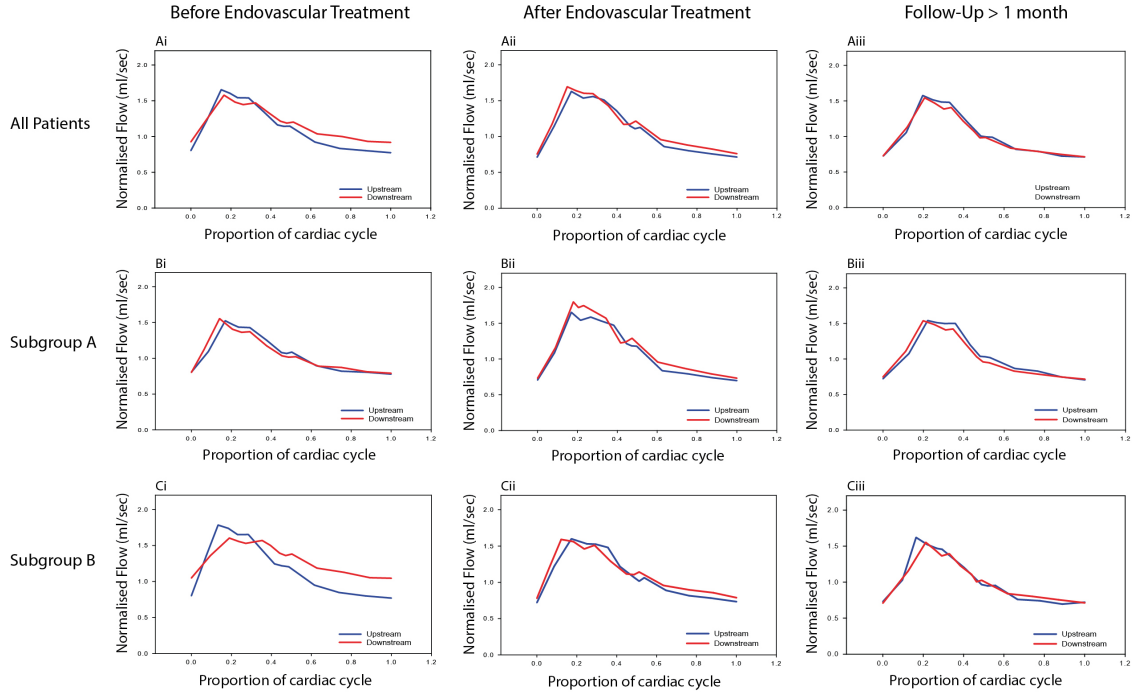


Figure 27 : Normalized VFR waveforms for patient group, subgroup A and subgroup B.

Mean normalized VFR waveforms at upstream and downstream segments of the ICA for patient group (A; row 1), patients subgroup A (B; row 2) and patients subgroup B (C; row 3) before EVT (I; column 1), after EVT (ii; column 2) and at follow-up (iii; column 3). Before EVT the mean normalized VFR waveforms upstream and downstream to the aneurysm were globally similar in the whole patient group and in subgroup A. In the subgroup B, the mean normalized VFR waveforms upstream and downstream were significantly different. Downstream to the aneurysm, the flow profil showed a decrease fo the systolic peak and an increase of the diastolic velocities. After EVT and at follow-up, the mean normalized VFR waveforms upstream and downstream to the aneurysm were similar in the whole patient group, and both subgroup A and subgroup B.

4.4 Discussion

In this part of our work, by following a patient group treated by flow diversion technique for UIAs, we assessed the impact of the aneurysms on the parent vessel hemodynamic with MRI flow measurements upstream and downstream to the malformation. We highlighted two main findings: 1) the IAs induced some hemodynamic disturbances within their parent vessels characterized by a dampened blood flow and a decrease of the Rl ratio and Pl ratio values in the downstream arterial segment. The induced disturbanes were strongly and inversely correlated to the aneurysm's volume. 2) The FDS had a measurable corrective effect on these flow modifications in the parent vessel for large aneurysms.

These results are in good agreement with the *in vitro* observation made on the test bench previously (see chapter 3). They support strongly the impact of the aneurysm on the parent artery resistance, namely its significant decrease (low impedance effect) which should be inversely proportional to the size of the malformation (and therefore to its diameter as described in the equation 15). Moreover, in someway the *in vivo* investigation allowed to overcome one of the limit of the previous *in vitro* investigation with regard to the limited number of explored aneurysm geometries. Indeed, the wide range of aneurysm volumes (55 to 6735 mm³) and their various morphologies in the patient group showed the significance of the aneurysm geometry, and especially its volume, on the flow changes inside the parent artery.

The aneurysms were responsible for a flow disruption into the downstream segment of the parent vessel which was characterized by a decreased and moderately delayed systolic peak and a relative increase of the diastolic flow. It was reflected by decreased *Rratio* and *Plratio* values. These modifications were visible only for large aneurysms (subgroup B, median volume : 3648 mm³), whereas the smaller ones (Subgroup A, median volume : 603 mm³) did not seem to impact significantly the parent artery hemodynamic.

However, the pattern of the hemodynamic changes in the parent vessel induced by the aneurysm *in vivo* can not be summarized only by resistive changes. Indeed, a certain degree of changes in the arterial capacitance might also be involved in the effect of the aneurysm on the parent vessel *in vivo*. Unlike to the silicone hydraulic circuit of the test bench which present a negligible capacitance, the wall mechanical properties of the parent artery are known to change at the level of the aneurysm which have a thinner wall¹¹⁰⁻¹¹². The reduction of the wall thickness as well as the increase of arterial volume corresponding to the malformation should increase the distensibility and therefore the capacitance of the diseased segment. As reported by some authors, the increased distensibility of the aneurysm seems to predominate at its dome¹¹⁰, and therefore might be more pronounced for large aneurysms. One can presume that during systole a part of blood flow might be retained in the aneurysm first, contributing partly to the relative decrease of systolic peak velocity downstream, and might be « regurgitated » into the parent vessel during diastole in a second time, explaining partly the relative increase of diastolic velocities.

Our results are also in good agreement with previous data of Gwilliam et al¹⁰². The average VFR waveforms presented similar shape and modulation over a cardiac cycle as described previously, with no significant change in pulsatility (ie, *PI*) between upstream and downstream measurement points on ICA (represented by *Plratio* values close to 1) in both the control group and in the patient group after the EVT.

The parent artery geometry and the position of the aneurysm with respect to it are known to impact on the intra aneurysmal flow and the FDS efficiency^{2,113}. As hypothesized by Gwilliam et al., the geometric changes in the artery caused by an aneurysm induce some hemodynamic modifications in the parent vessel. Interestingly, the modifications of the VFR waveforms were depicted only within the segment of the ICA downstream to the aneurysm and not at upstream level (extracranial), as suggested by Gwilliam et al. This result weakens the possibility to implement a screening of the patients with IAs at cervical level of the carotid tree by a simple method such as Doppler ultrasounds technique as proposed by the author.

The FDS for the treatment of UIA has already shown great promise by allowing the “morphological reconstruction” of the diseased arterial segment^{32,98}. We observed and quantified a “hemodynamical reconstruction” of the parent vessel treated by FDS. This “hemodynamical reconstruction” was observable only for large aneurysms (subgroup B) immediately after the EVT. It was characterized by an increase of the *Rratio* and *Plratio* values reflecting the increase of *RI* and *PI* values downstream to the aneurysm. It demonstrated the restoration of a normally modulated flow pattern distal to the aneurysm, which remained unchanged at the follow-up examination. Regarding the mVFR in upstream and downstream segments of the parent artery, they were comparable and seemed to not be modified by the presence of the aneurysm, which is consistent with the law of conservation of mass. It suggests that large aneurysms affect the resistive and pulsatility indexes (i.e., the flow pattern) rather than the mVFR in the downstream segment of parent vessel, as shown by the graphical representation of the VFR waveforms. One can reasonably hypothesize that the

changes in the downstream vessels after the EVT, and thereby more distally in the vascular bed within the brain parenchyma, are more related to the acute resistive and pulsatility indexes correction than to the mVFR modifications, which should not be significant because of the law of conservation of mass. From a clinical point of view, these results allows us to make assumptions about some complications reported after treatment of large aneurysms. One can reasonably assume that the sudden increase of the *PI* in a probably long-standing downstream dampened blood flow (i.e., with a decreased *PI*) within the ipsilateral hemisphere could play a role in intra parenchymal haemorrhage or in hyperperfusion syndromes that have been previously reported after the treatment of large aneurysms either by clipping or by endovascular techniques^{35,114,115}. The knowledge of this eventual effect for large aneurysms could be taken into account for the treatment decision and the post-operative management of the patients. We did not observe such complications in our series of patients.

All the symptomatic patients had lower *Rlratio* and *Plratio* values before the EVT, which were associated to the larger volumes. While all the asymptomatic patients had *Rlratio* and *Plratio* values comparable to those in the control group. This analysis is biased by the aneurysm's volume, which can be considered as a confounding factor responsible for both the symptoms and the *Rlratio* and *Plratio* values decrease.

In this work we used a non-invasive and non-irradiating technique widely available in clinical practice: the time resolved 2D PC-MRI. It combines reduced acquisition times and high both (in-plane) spatial and temporal resolutions. Since, the table occupancy was voluntarily limited (20 minutes) the method allowed for the measurements of only 20 to 31 points over the cardiac cycle for each phase-contrast acquisition. This was clearly lower than the 40 measurements points in the work of Gwilliam et al. However, it did not seem to have any impact on the reproducibility of the method and the VFR waveforms analysis. Moreover, we used a 2D PC-MRI acquisition with higher spatial resolution ($0.31 \times 0.31 \text{mm}^2$ in-plane resolution vs. $1.72 \times 1.60 \text{mm}^2$ in previous work) which allowed for a more accurate signal with shorter image times. The 2D PC-MRI was successfully performed by most of the patients and healthy volunteers.

This study had several limitations. Since only aneurysms of the intracranial ICA treated by FDS were included, the number of patients was limited. Only ICA aneurysms were included in order to simplify the analysis and to limit the velocity measurements on relatively large and straight arterial segments for which no underestimation in flow and velocity measurements is expected with 2D PC-MRI¹⁰⁹. Only two partially thrombosed aneurysms were analyzed. Therefore, the effect of the intrasaccular thrombosis on the flow waveform could not be assessed. Thus, the significance of *Rlratio* and *Plratio* values regarding intra saccular thrombosis was not evaluated. Larger prospective studies could be considered to investigate this point. But, the large range of aneurysm volumes (from 55 to 6735mm^3) enabled the demonstration of a significant correlation between the aneurysm's volume and its impact on the parent vessel hemodynamic. Control and patient groups were not matched for age because of the limited size of our series. The mean age of the control group was significantly lower than the mean age of the patient group. The effect of age on the *RI* and *PI* of large arteries, a such as the ICA, has already been reported in the literature literature^{56,109}. Since we analyzed the *Rlratio* and *Plratio* values between the upstream and downstream segments of the parent vessel relative to the aneurysms location instead of the *RI* and *PI* alone, our methodology should overcome the effect of age. Furthermore, the *Rlratio* and *Plratio* values in subgroup A at each time point, the *Rlratio* and *Plratio* values in subgroup B after the EVT and at follow-up, and those in the control group, as well, were comparable and not

significantly different. These latter results highlight the robustness of the *Rlratio* and *Plratio* values analysis in time regarding the potential effects of age. The effect of arterial normal stiffening associated with the age affecting the arterial compliance was not observed in our limited cohort, either in the patient or in control groups. However, the significant age difference between the patient and the control group had an impact on the computationed mVFR. The mVFR were higher in the control group compared to the patient group before the EVT, after the EVT and at follow-up. This result is in good agreement with previous studies that had shown an inverse correlation between the age and the mVFR^{56,109}.

4.5 Conclusion

This clinical part of our work, allowed to clearly demonstrate the hemodynamic disturbances induced by IAs within their parent vessel. The hemodynamic changes were characterized by a dampened blood flow and a decrease of the *Rlratio* and *Plratio* values in the downstream arterial segment. The induced disturbances were strongly and inversely correlated to the aneurysm's volume. The FDS had a measurable corrective effect on these flow modifications in the parent vessel for large aneurysms. This is the first work quantifying *in vivo* the hemodynamic impact of the IAs on the parent vessel and its correction by FDS. These findings provide new insights into the complex relationship between the aneurysm and its parent vessel hemodynamic. We believe that the hemodynamic changes in both the parent vessel and the aneurysmal sac are indissociable for a better comprehension of the intracranial aneurysmal disease. Further studies on a larger number of patients with different aneurysmal localizations and geometries will be needed to confirm our results and to clarify the significance of the computed PI-ratio values regarding the interaction between the aneurysm and parent vessel hemodynamics, and also to the long-term efficiency of the FDS.

CHAPTER 5

5 2D PC-MRI segmentation : an original Fourier Transform based approach

5.1 Introduction

We emphasized in Chapter 2 that the reliable and accurate segmentation of 2D PC-MRI images was crucial to the exploitation of the measured blood flow information (velocities and VFR curves and indices obtained from their analysis). Chapter 4 illustrated the use of segmented 2D PC-MRI allowing for the extraction of VFR curve over time and their exploitation to the understanding of aneurysmal disease. The final chapter of this work offers an original approach for 2D PC-MRI segmentation developed in the neuroradiology department of the University Hospital of Montpellier. This method is based on the Fourier Transform (FT) analysis of the phase image. It was compared with two other widely used methods for segmentation : manual segmentation and segmentation by ACM according to the Chan-Vese model (ACM-CV).

In this part of our work, we will focus on the segmentation by ACM as proposed by Chan-Vese. We will present the approach from a mathematical point of view and we will put forward a new segmentation approach based on the FT analysis of the phase images of 2D PC-MRI.

5.1.1 Active contours method according to the Chan-Vese model for segmentation

The *in vivo* study of our work consisted of segmenting ICAs from 2D PC-MRI obtained from patients followed and treated for IAs. It also consisted of extracting velocity and VFR curves. The segmentation method used was based on the ACM without edge according to the Chan-Vese model⁸⁰. This technique is a powerful and flexible method of segmentation which is able to segment many types of images, including some that would be difficult with more classic segmentation methods, such as thresholding or gradient methods. ACM-CV is widely used in the field of medical imaging, and in particular for the segmentation of the brain, heart, aorta or trachea. This approach is based on the model of Mumford-Shah segmentation¹¹⁶. The principle of the model relies on the statistical homogeneity of intensity in each region within the image and on an energy minimization problem. An average descriptor of the form of an integral equation varying over the region is used. This region based approach takes into account the properties of the image on the regions and not locally. It can be rewritten using the levels set method (LSM), allowing a simpler solution to the problem⁸⁰. This mathematical approach allows automatic management of topology changes, distance function and allows stable and accurate numerical schemes.

The peculiarity of the Chan-Vese model is to overcome the use of gradient functions needed in some contour-based ACM such as the geodesic ACM. In these models, the gradient's functions can be unclear in a picture because of blurring artifacts, a weak signal or a too low

signal to noise ratio (which is sometimes the case with the outline of ICA, for example). Therefore, in this contour-based ACM, contours can sometimes exceed mistakenly those of the object studied.

Chan and Vese described an ACM without any need of gradient (ACM-CV), such as:

Let $C \subset \Omega$ a closed parameterized curve, with *inside* (C) and *outside* (C) open sets. Let u_o an image formed by two intensity regions almost constant, u_0^I and u_0^O . Let u_0^I and u_0^O the colors of the object in the background

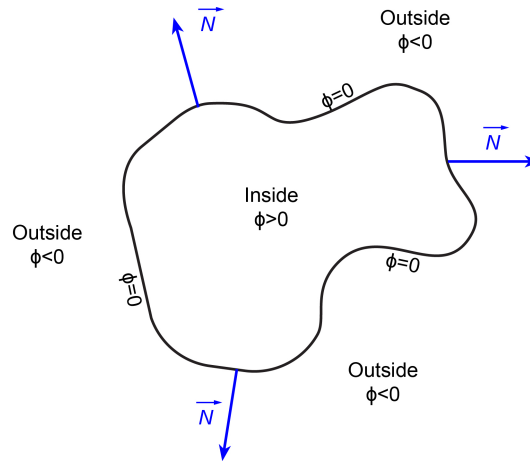


Figure 28 : Simplified illustration of the active contours and its sets (inside and outside).

With curve $C = \{(x,y) : \phi(x,y) = 0\}$ propagating in normal direction \vec{N} .

$$F_1(C) + F_2(C) = \int_{inside(C)} |u_0(x-y) - c_1|^2 dx dy + \int_{outside(C)} |u_0(x-y) - c_2|^2 dx dy \quad \text{Equation 24}$$

With c_1 and c_2 the average intensity inside and outside of C . The minimizer F of the fitting term can be written as :

$$\inf_C \{F_1(C) + F_2(C)\} \approx 0 \approx F_1(C_0) + F_2(C_0) \quad \text{Equation 25}$$

The minimizer of F , $\inf_C \{F_1(C) + F_2(C)\}$, is obtained for $C = C_0$ following the contour of the object and the average intensity c_1 and c_2 of the object to the background.

We then consider the following minimization (optimization) problem:

$$\inf_{c_1, c_2, C} F(c_1, c_2, C) \quad \text{Equation 26}$$

The Chan-Vese method uses functional energy to minimize, as follows:

$$F(c_1, c_2, C) = \mu \cdot \text{Length}(C) + \nu \cdot \text{Area}(\text{int}(C)) \\ + \lambda_1 \int_{\text{int}(C)} |u_0(x-y) - c_1|^2 dx dy + \lambda_2 \int_{\text{ext}(C)} |u_0(x-y) - c_2|^2 dx dy \quad \text{Equation 27}$$

Where $\mu \geq 0, \nu \geq 0, \lambda_1, \lambda_2 > 0$ are fixed parameters.

The method can be formulated in terms of all level sets, as :

$$\begin{cases} C = \partial\omega = \{(x, y) \in \Omega: \phi(x, y) = 0\} \\ \text{inside}(C) = \omega = \{(x, y) \in \Omega: \phi(x, y) > 0\} \\ \text{oustside}(C) = \Omega \setminus \bar{\omega} = \{(x, y) \in \Omega: \phi(x, y) < 0\} \end{cases} \quad \text{Equation 28}$$

$$H(z) = \begin{cases} 1, \text{ si } z \geq 0 \\ 0, \text{ si } z < 0 \end{cases} \quad (\text{Heaviside Fonction}) \quad \text{Equation 29}$$

$$\delta_0(z) = \frac{d}{dz} H(z) \quad (\text{Dirac Fonction}) \quad \text{Equation 30}$$

The length and the area of the shape can be expressed as:

$$\begin{aligned} \text{Length} \{\phi = 0\} &= \int_{\Omega} |\nabla H(\phi(x, y))| dx dy \\ &= \int_{\Omega} \delta_0(\phi(x, y)) |\nabla H(\phi(x, y))| dx dy \end{aligned} \quad \text{Equation 31}$$

$$\text{Area} \{\phi \geq 0\} = \int_{\Omega} H(\phi(x, y)) dx dy \quad \text{Equation 32}$$

The two standard deviations of intensities are thus expressed as:

$$\int_{\phi > 0} |u_0(x, y) - c_1|^2 dx dy = \int_{\Omega} |u_0(x, y) - c_1|^2 H(\phi(x, y)) dx dy \quad \text{Equation 33}$$

$$\int_{\phi < 0} |u_0(x, y) - c_2|^2 dx dy = \int_{\Omega} |u_0(x, y) - c_2|^2 (1 - H(\phi(x, y))) dx dy \quad \text{Equation 34}$$

Then the energy $F(c_1, c_2, C)$ can be written as:

$$\begin{aligned} F(c_1, c_2, C) &= \mu \int_{\Omega} \delta(\phi(x, y)) |\nabla \phi(x, y)| dx dy \quad (\text{Length}) \\ &+ \nu \int_{\Omega} H(\phi(x, y)) dx dy \quad (\text{Area}) \\ &+ \lambda_1 \int_{\Omega} |u_0(x, y) - c_1|^2 H(\phi(x, y)) dx dy \quad (\text{Standard error inside}) \\ &+ \lambda_2 \int_{\Omega} |u_0(x, y) - c_2|^2 (1 - H(\phi(x, y))) dx dy \quad (\text{Standard error outside}) \end{aligned} \quad \text{Equation 35}$$

A regularized version of the functional can also be considered, such as:

$$\begin{aligned}
F_{\varepsilon}(c_1, c_2, C) &= \mu \int_{\Omega} \delta_{\varepsilon}(\phi(x, y)) |\nabla \phi(x, y)| dx dy + \nu \int_{\Omega} H_{\varepsilon}(\phi(x, y)) dx dy \\
&+ \lambda_1 \int_{\Omega} |u_0(x, y) - c_1|^2 H_{\varepsilon}(\phi(x, y)) dx dy \\
&+ \lambda_2 \int_{\Omega} |u_0(x, y) - c_2|^2 (1 - H_{\varepsilon}(\phi(x, y))) dx dy
\end{aligned}
\tag{Equation 36}$$

The regularization of the image may be for example a Gaussian.

We will look for the solution with the Euler-Lagrange equation computation by decreasing the energy gradient F , by keeping bearing c_1 and c_2 fixed, such as:

$$\begin{aligned}
\frac{\partial \phi}{\partial t} &= \delta_{\varepsilon}(\phi) \left[\mu \operatorname{div} \left(\frac{\nabla \phi}{|\nabla \phi|} \right) - \nu - \lambda_1 (u_0 - c_1)^2 + \lambda_2 (u_0 - c_2)^2 \right] \\
&= 0 \quad \text{in } (0, \infty) \times \Omega
\end{aligned}
\tag{Equation 37}$$

$$\phi(0, x, y) = \phi_0(x, y) \in \Omega$$

$$\frac{\delta_{\varepsilon}(\phi)}{|\nabla \phi|} \cdot \frac{\partial \phi}{\partial \vec{n}} = 0 \quad \text{sur } \partial \Omega \tag{Equation 38}$$

In practice, the use of this method for the 2D PC-MRI is done by application of the technique on the amplitude image in the first instance. It provides an initial segmentation mask. This latter allows for the measurements of the areas of the analyzed vessel section over time. The implementation and application of the mask to the phase images enables calculation of the velocities and flows. This method of segmentation initially operates on the amplitude image because of the contrast between the vascular structures, hyper intense, and the background (or noise) hypo intense compared to the lower contrast on phase images. Figure 29 schematically illustrates the action of the ACM-CV model on 2D PC-MRI images.

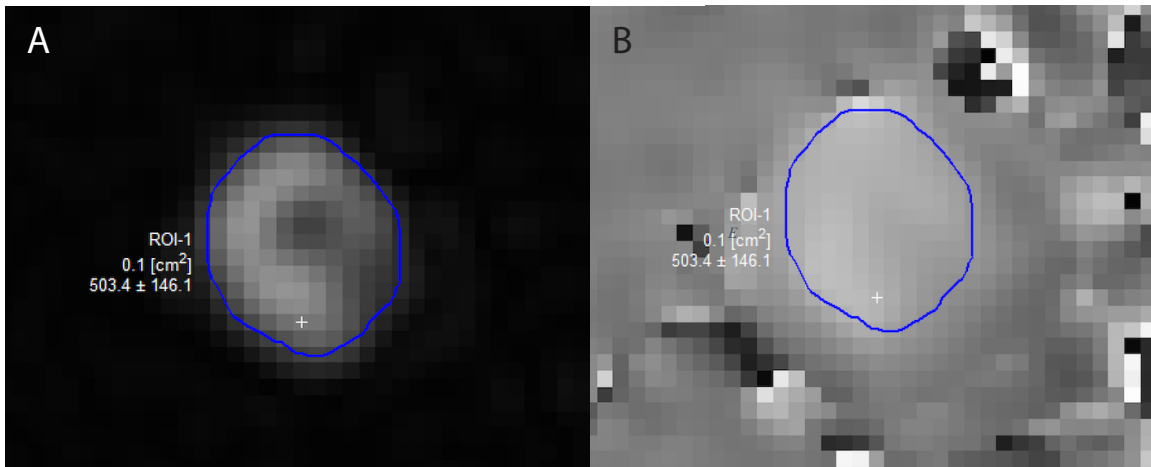


Figure 29 : Exemple of an ICA 2D PC-MRI segmented with ACM-CV.

This exemple illstrates the segmentation on the magnitude image (image A) based on the ACM-CV. The resulted segmentation mask is applied to the phase image (image B). The area of the studied arterial section on the magnitude image seems smaller than that of the phase image. A significant number of « vascular voxels » remain outside of the segmentation contours. The picture comes from the work of Jérémy Deverduin¹¹⁷.

The ACM-CV has demonstrated its efficiency and ease of use for the study of anatomical structures of a large size, such as the heart and the aorta. However, the efficacy of this approach has not been studied for the segmentation of the ICA which present a small size (compared to that of the heart and aorta). Its small size is more subject to low contrast and noise.

5.1.2 New method of segmentation based on a Fourier Transform analysis

The PC-MR images of vascular structures (or CSF) are consistent over time, or temporarily consistent. The CSF and blood are synchronized to the cardiac cycle. This therefore results in a significant cardiac frequency component in their velocity curves over time. The set of images acquired during a heart cycle leads to a coherent one-dimensional signal. Conversely, adjacent structures to the vessels (soft tissue, bone, air) are not synchronized to the cardiac cycle. They have a non-coherent signal that can be likened to the noise. Thus, the PC-MRI can be considered as a series of acquisitions in a sequence which itself is a sampling of a cardiac cycle. The use of the temporal dimension corresponding to physiological information (the kinetic of the velocities over time, for example) to establish segmentation could thus conceptually be considered to help the differentiation between vascular structures surrounded by noise. This is illustrated in Figure 30 which shows the results of the FT analysis of a vascular voxel (with a temporal consistency) compared to that of a noisy background voxel of the phase image. The significance of the difference in amplitude values between both voxels is highlighted here (there is at least a factor of ten between the amplitudes of noise and blood). The signal amplitude of the FT of the image can be a simple threshold criterion for segmenting the phase images of PC-MRI.

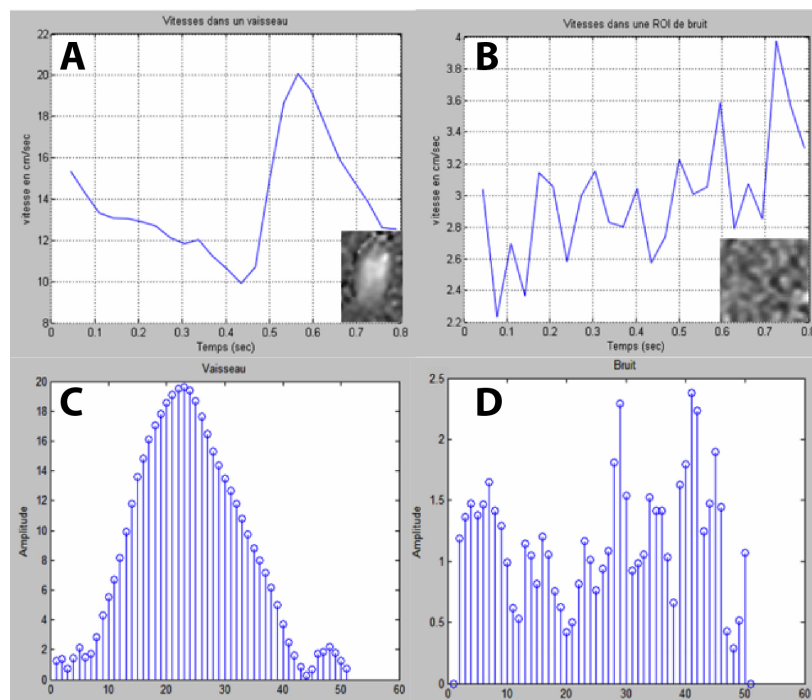


Figure 30 : Difference in velocity curve and FT result between a vessel and noise.

The signal of a vascular voxel shows a velocity profile consistent with cardiac cycle (image A) and discrete 1D FT analysis (image B) showing a coherent “bell shaped” spectrum with a high amplitude. In contrast, a noise voxel present a non-coherent velocity profile (image B) and discrete 1D FT analysis (image D) resulting in a spectrum with random values and very low amplitudes (scale of 1 to 20 times smaller). The picture comes from the work of Jérémy Deverduin¹¹⁷.

The sampling of the 2D MRI sequences is composed of a variable number of images, which is a function of the subject's heart rate, and represents as many phases of the cardiac cycle. These images provide spatial information (or spatial dimensions) and time information (or time dimension), since the same voxel signal is monitored during the cardiac cycle. The analysis of the temporal kinetics of the voxel signal over time (i.e., the cardiac cycle) is the basis of the segmentation method by analysis of FT (FT based method, FTM) used in this work. The latter is inspired from the work of Balédent et al. who initially proposed this approach to segment and quantify the cerebrospinal fluid flow (LCS) from 2D PC-MRI ¹¹⁸.

The velocity curves are derived from a sampling of the PC-MRI signal and therefore from discrete values. N velocity values are acquired at regular intervals during the cardiac cycle at different times separated by Δ , as:

$$\Delta = T/N \quad \text{Equation 39}$$

Where T is the duration of a cardiac cycle and Δ is the sampling period. In the case of digital periodic signals, the discrete or fast FT (for Fast Fourier Transform, FFT) is applied ¹¹⁹. For any discrete signal, the FT is given by the following formula :

$$X(n) = \sum_{k=0}^{N-1} x(k). e^{\frac{j.2\pi.k.n}{N}} \quad \text{Equation 40}$$

Where $n \in [1, N]$, N is the number of samples, k and n are the time and frequency indices respectively, $x(k)$ is the sampled signal at the k^{th} time of the cycle, $X(n)$ is the FT for the n^{th} frequency. Therefore, there is N values of (k) et $X(n)$.

The values $X(n)$ are complex numbers, and will therefore be subsequently decomposed in amplitude and phase. The FFT transforms N integers $x(k)$ in N complex numbers $X(n)$ regardless of the spatial dimension and thus the sampling period. Conventionally, the FT is sampled over a range of frequencies fn between $-fc$ and $+fc$, with $fc = 1/2\Delta$ the critical frequency at which the validity criterion of the sampling or Shannon-Nyquist criterion is not verified. The frequency values of fn for which the signal of the FFT is sampled are of the form:

$$fn = n/N\Delta \quad \text{Equation 41}$$

Where : $N \in 2\mathbb{N}$ and $n = -\frac{N}{2}, -\frac{N}{2} + 1, -\frac{N}{2} + 2 \dots, \frac{N}{2}$

The FFT is periodic in n and with a period of N . Then :

$$X(-n) = X(N - n) \quad \text{Equation 42}$$

Thus, the frequency 0 is thus obtained for $n = 1$. Positive frequencies $0 < f < fc$ correspond to the values $2 \leq n \leq N/2$, while the negative frequencies $-fc < f < 0$ correspond to values $2 + N/2 \leq n \leq N$. We note that the value $n = 1 + N/2$ corresponds to both $f = fc$ and $f = -fc$.

As part of this work, we used a similar approach for the segmentation of the vessels, but more optimized for the analysis of intracranial vascular structures, by Dr. J. Deverdun from the neuroradiology department of the University Hospital of Montpellier (France)¹¹⁷. Indeed, the FFT based approach of the phase image analysis according to the method of Balédent et al. provides only a unique segmentation for all the images, and does not allow to analyze changes over time in the size of the studied object (i.e., the section of the analyzed vascular structure)¹¹⁸.

In order to take into account the variation in size of the segmented object over time (and thus the evolution of the vessel section), the method was modified to allow the application of the FFT over a sliding window of several consecutive phase images for the analysis of one voxel. In other words, by this change the temporal dimension of the voxel signal is analyzed over a window of several images which vary according to the segmented image. Segmenting at the time t the phase image is carried out taking into account the signal of the images from $t - 2$ to $t + 2$ (i.e., a Kernel of 5 images). This 5 image analysis window is thus shifted to obtain the segmentation at time $t + 1$, $t + 2$, and so on up. This results in a segmentation changing over time and thus following the variation of the area of the segmented vessel during the cardiac cycle. In practice, the segmentation based on the FTM is applied directly to the phase images. Figure 31 and 32 illustrates schematically the action of the FTM based segmentation 2D PC-MRI images.

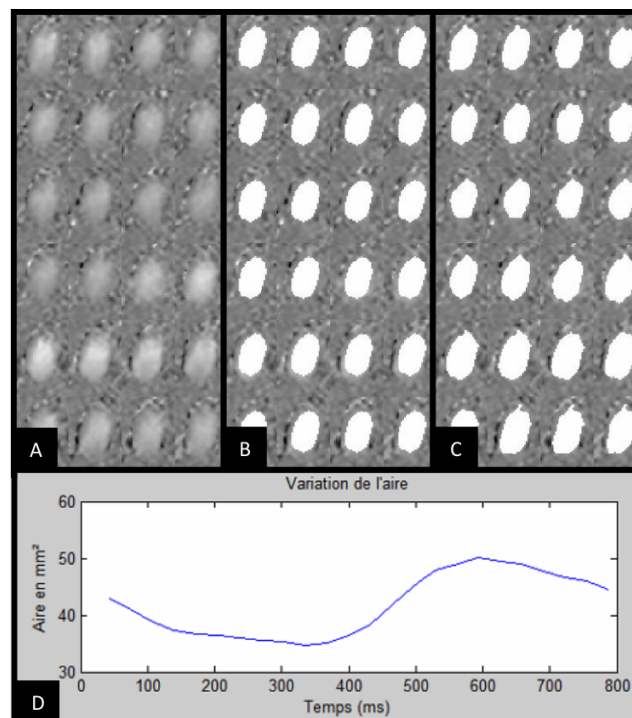


Figure 31 : Principle of the segmentation of PC-MRI with FTM.

No initialization of the contour and no work on the amplitude image are needed. The algorithm operates directly on the phase images (image A). According to the FT amplitude threshold, it provides different results of segmentation (images B and C). A pixel-by-pixel analysis over time of the entire phase contrast image is carried out. It enable also to show the evolution of the area curve (image D). The picture comes from the work of Jérémy Deverdun¹¹⁷.

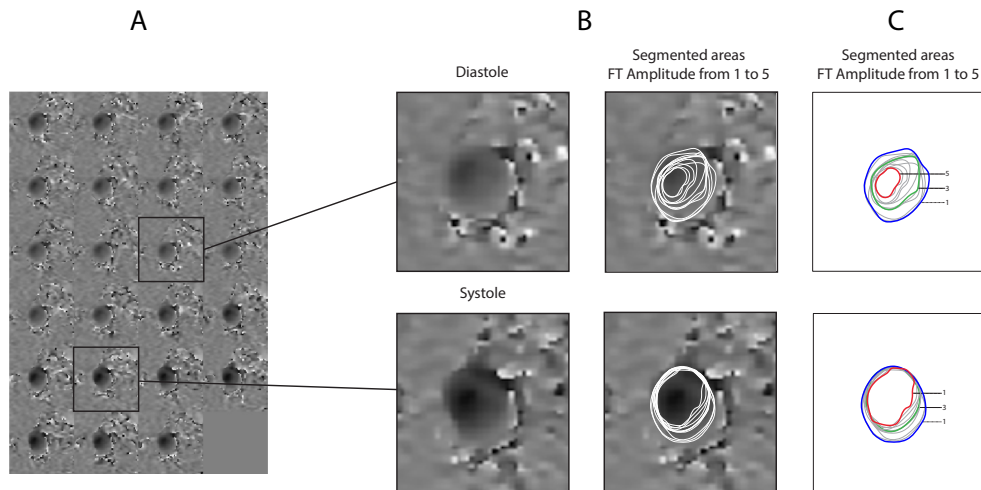


Figure 32: Principle of the segmentation of PC-MRI with FTM.

No initialization of the contour and no work on the amplitude image are needed. The algorithm operates directly on the phase images (A). Two frames corresponding to the diastolic end and to the systolic peak are magnified (image B). A pixel-by-pixel analysis over time of the entire phase contrast image is carried out. The different contours of segmentation according to the FT amplitude threshold varying from 1 to 5 are represented (white contours on image B). The same contours of segmentation were represented and the three remarkable contours were labeled in blue (largest segmentation for $Amp = 1$), in green (the median segmentation for $Amp=3$) and in red (the smallest segmentation for $Amp = 5$).

The FTM segmentation algorithm consists of several steps, as following:

- Step 1: Definition of a ROI encompassing the object of interest (i.e., the ICA) that will be applied to all phase images in the series resulting in a 3D matrix $M[x, y, t]$ representing the evolution of each voxel over time (or the cardiac cycle in our case). The matrix $M[x, y, t]$ characterizes the phase shift of the spins of the voxel related to their movement velocity.
- Step 2: Application of the FFT to each voxel at each time by using a sliding window based on a Kernel of 5 from $M[x, y, t - 2]$ to $M[x, y, t + 2]$, meaning from time $t - 2$ to time $t + 2$. It results in a new matrix in the frequency domain $P[x, y, f]$ with x and y the positions of the voxel within the image and f its frequency varying from 0 to $N - 1$, as seen above.
- Step 3: Selecting a minimum threshold amplitude (Amp) of the matrix $[x, y, f]$ thus permitting the selection of voxels synchronized to the cardiac cycle (whose amplitude is greater than Amp) and the elimination of those with a very low or no synchronization with the heartbeat (whose amplitude is less than Amp). The use in the previous step (step 2) of a sliding window of analysis allows us to achieve a scalable segmentation over time.
- Step 4: Displaying the mask and the results of the segmentation directly on the phase images and the average velocity, the average flow rate and the surface variation curves over a cardiac cycle of the selected vessel.

The threshold value of the *Amp* after operation by the FTM defines the sensitivity of the segmentation. A low value of this threshold is associated with the inclusion of the lower velocity voxels within the segmentation surface.

5.2 Materials and methods

The new FTM based segmentation approach was used to segment 2D PC-MRI of ICA performed in healthy volunteers. Initially, the effect of the *Amp* variation on the results of the segmentation FTM was evaluated. Secondly, the results of the segmentation by this method were compared with the results of segmentations obtained with the MM and ACM-CV.

5.2.1 Population and 2D PC-MRI examinations

2D PC-MRI images of ICA performed on five healthy volunteers were used for this work. The healthy volunteers were aged from 22 to 55 years old (the average age being of 29; interquartile range 25 to 39). The agreement of the local ethics committee was obtained for this work (DGRI CCTIRS MG / CP 2012528; Ethics Committee of the University Hospital of Lyon, Lyon / France) and informed consent was obtained from all volunteers.

2D PC-MRI was performed using the same protocol and the same conditions as previously described in Chapter 4 (§ 4.2.3). However, a single 2D PC-MRI acquisition on the ICA was performed at its sub-petrousal or intra-petrous segments. The choice of ICA segment studied by 2D PC-MRI depended on the anatomy of the artery, and particular attention was paid to set the acquisition plane on a straight arterial segment. Figure 33 shows the positioning of the 2D PC-MRI acquisition plan.

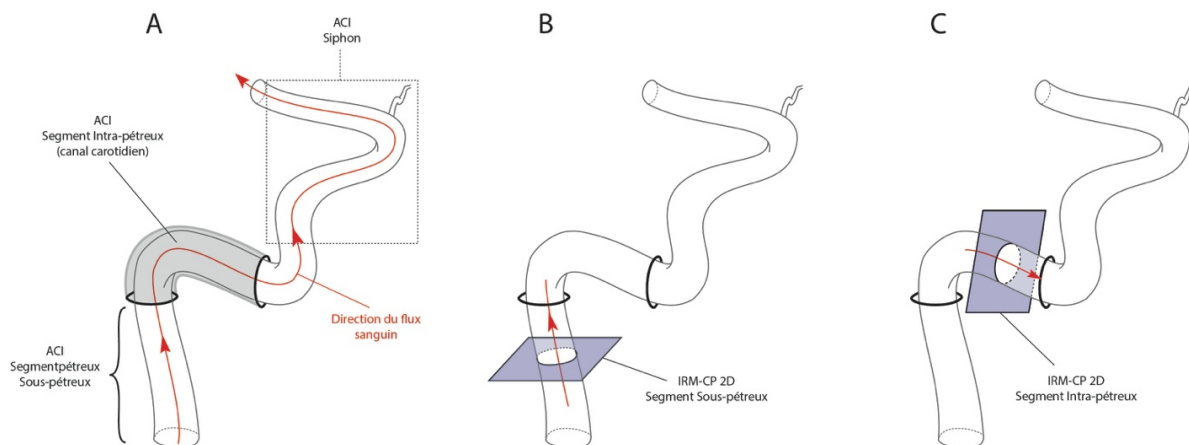


Figure 33 : Positioning of 2D PC-MRI slice on the ICA.

A : ICA shown with its different segments (sub-petrousal, intra-petrous and siphon) and the direction of blood flow (red). *B* : placement of a 2D PC-MRI acquisition plan orthogonal to the flow direction on the sub-petrous segment. *C* : placement of a 2D PC-MRI acquisition plan orthogonal to the flow direction on intra-petrous segment.

5.2.2 Segmentation of 2D PC-MRI by three different methods

All the acquired flow MRI data was post-processed by the three different segmentation methods: MM, ACM-CV and the FTM proposed in this work.

5.2.2.1 Segmentation by Manual method

The segmentation of the acquired 2D PC-MRI by the MM was carried out by two independent and experienced users (user 1 and user 2) in the analysis of supra aortic trunks and particularly of the ICA. Image analysis was performed using the free SEGMENT software (version 1.9 SEGMENT R4510; <http://segment.heiberg.se>) which allows the realization of manual segmentation¹²⁰⁻¹²². The software calculated the area of the segmented arterial section, the average velocity and average flow rate through the same arterial section on each image. The results were shown as graphics of the areas, velocities and flow rate curves over time (i.e., one cardiac cycle). The numerical results were immediately usable from an Excel spreadsheet.

5.2.2.2 Segmentation by active contours method according to the Chan-Vese model

Semi-automatic segmentation by ACM-CV was performed on the same images with the same free SEGMENT software (version 1.9 SEGMENT R4510; <http://segment.heiberg.se>)¹²⁰⁻¹²² which also allows automated segmentation based on this method. An initiation of the segmentation was performed by a first manual delineation of the ICA on the first frame of each series of 2D PC-MRI. After automatic segmentation of ICA in each image of the 2D PC-MRI sequence, the software calculated the area of the segmented arterial section and the average velocity and average flow rate through the same arterial section on each image. The results were also shown in graphic form, the areas, velocities and flow rate curves over time (i.e., one cardiac cycle). The numerical results were instantly usable from an Excel spreadsheet.

5.2.2.3 Segmentation by Fourier Transform based method

The series of 2D PC-MRI images were segmented with the FTM tool developed in the neuroradiology department of the University Hospital of Montpellier and implemented with MATLAB software (MATLAB software, R2014a Student Version 8.3.0.532, The MathWorks, Inc., Natick, Massachusetts, United States). No initiation of segmentation was necessary. Only the ROI containing the vascular structure of interest (ICA) was defined to reduce the time of calculations. Initially the approach of Balédent et al incorporated choosing the *Amp* parameter by the user and different values of *Amp* needed to be tested to obtain the best fitted segmentation. As part of this work and in order to propose a segmentation tool as automatic as possible and requiring the least amount of intervention from the user, we focused initially on the effect of the variation of *Amp* on the results of the segmentation of the ICA. Thus, we have made several segmentations without user intervention with values of *Amp* ranging from 1 to 5 (increasing by steps of 0.5). Secondly, the results of the FTM segmentations for all values of *Amp* were compared with the results of the segmentation obtained with the MM and the ACM-CV.

5.2.3 Analysis of the impact of the Fourier Transform amplitude threshold

The impact of the *Amp* variation on the segmentation with the FTM was evaluated for the results of the areas (A in mm^2), mean velocities (V in cm.s^{-1}) and mean flow rates (D in mL.min^{-1}) of the segmented arterial sections. These results were represented as A , V , and D curve functions of time, as $A(t)$, $V(t)$ and $D(t)$. Each curve was characterized by the amplitude of the systolic-diastolic difference and the average of the variable over the cardiac cycle (i.e., the area under the curve). Assessing the effect of the variation of *Amp* on the segmentation results by FTM was carried out through the calculation of three parameters for each *Amp* value i (from 1 and 5), as follows: the amplitude of the systolo-diastolic difference relative to the value at the systolic peak (a *RI* equivalent parameter), the average value over the cardiac cycle, and the amplitude of the systolo-diastolic difference relative to average value over the cardiac cycle (a *PI* equivalent parameter).

5.2.4 Parameters of analysis : average, resistive and pulsatility equivalent indexes

The amplitude of the systolic-diastolic difference of A relative to its value at the systolic peak RIA_i is defined as :

$$RIA_i = \frac{Asyst_i - Adiastr_i}{Asyst_i} \quad \text{Equation 43}$$

With $Asyst_i$ and $Adiastr_i$ the values of A at the systolic peak and at the diastolic end, respectively, and $(Asyst_i - Adiastr_i)$ its systolic-diastolic difference, and i th evalue of *Amp*. This parameter is the equivalent of the *RI* used in Doppler velocimetry flow analysis.

The average value of A (A_{avg}) over a cardiac cycle, such that:

$$A_{average_i} = \int_{t \in I} A_i(t) dt \quad \text{Equation 44}$$

with $A_i(t)$ the function of A over time for the value i of *Amp*, $I = [0, T]$ and T corresponding to the duration of the cardiac cycle.

And the difference $(Asyst_i - Adiastr_i)$ relative to $A_{average_i}$, which can be considered as a *PI* used in velocimetric flow studies and is calculated as follows:

$$PIA_i = \frac{Asyst_i - Adiastr_i}{A_{average_i}} \quad \text{Equation 45}$$

Likewise, similar indexes were calculated for mean velocities (RIV , $V_{average}$, RIV) and average flow rates (RID , $D_{average}$, PID), such as:

$$RIV_i = \frac{Vsyst_i - Vdiast_i}{Vsyst_i} \quad RID_i = \frac{Dsyst_i - Ddiast_i}{Dsyst_i} \quad \text{Equation 46}$$

$$V_{average_i} = \int_{t \in I} V_i(t) dt \quad D_{average_i} = \int_{t \in I} D_i(t) dt \quad \text{Equation 47}$$

$$PIV_i = \frac{Vsyst_i - Vdiast_i}{V_{average_i}} \quad PID = \frac{Dsyst_i - Ddiast_i}{D_{average_i}} \quad \text{Equation 48}$$

With $Vsyst_i$, $Dsyst_i$, $Vdiast_i$, and $Ddiast_i$ the values of V and D at systolic peak and at diastole, respectively, and $V_i(t)$ and $D_i(t)$ the functions of V and D over time (the duration of a cardiac cycle). The main interest of these parameters is to distinguish the overall impact (via the values of PI) from the more specific impacts (through values of IR and *average*) of the variation of Amp on the results of the segmentation with FTM.

5.2.5 Normalization of the average, resistive and pulsatility equivalent indexes

For each ICA, the parameters previously described were therefore calculated for each value i of Amp ranging from between 1 to 5. Given the inter-individual variation in flow conditions within the ICA (velocities, flow rates), and in order to average the results obtained in different subjects, normalization of those parameters was carried out by taking as a reference the values of the indexes obtained for $Amp = 1$, such that:

Equations 49

$$\begin{aligned} nRIA_i &= \frac{RIA_i}{RIA_1} & nA_{average_i} &= \frac{A_{average_i}}{A_{average_1}} & nPIA_i &= \frac{PIA_i}{PIA_1} \\ nRIV_i &= \frac{RIV_i}{RIV_1} & nV_{average_i} &= \frac{V_{average_i}}{V_{average_1}} & nPIV_i &= \frac{PIV_i}{PIV_1} \\ nRID_i &= \frac{RID_i}{RID_1} & nD_{average_i} &= \frac{D_{average_i}}{D_{average_1}} & nPID_i &= \frac{PID_i}{PID_1} \end{aligned}$$

5.2.6 Agreement analysis of the segmentation results by the three segmentation methods

The values of A (in mm^2), V (in cm.s^{-1}) and D (in mL.min^{-1}) obtained with the three methods of segmentation were compared and their concordance was evaluated. To achieve this analysis, the segmentation methods (i.e., MM, ACM-CV and FTM) were compared two by two by the representation of graphics equivalence, Bland-Altman graphs, histogram of differences and the calculation of Lin's concordance correlation coefficient (CCC) (65). The CCC assessing the agreement or the reproducibility of two measures of the same phenomenon is better suited than the Pearson correlation coefficient in the context of our work^{123,124}. Indeed, the CCC evaluates the accuracy between two "readings" (i.e., methods of segmentation in our work) by measuring the variation of the linear relationship adjusted with respect to its consistency with the straight line of equivalence (45° straight line through the origin) and accuracy by measuring how far each observation deviates from the fitted line. Let x and y a pair of continuous random variables measured on the same subject (i.e., A , V or D) using two different methods (i.e., MM and ACM-CV, or FTM and MM, or FTM and ACM-CV). The CCC to measure the agreement between the values x and y is defined as:

$$\rho_c = 1 - \frac{E[(x-y)^2]}{E_{indep}[(x-y)^2]} = \frac{2s_{xy}}{s_x^2 + s_y^2 + (\bar{x} - \bar{y})^2} \quad \text{Equation 50}$$

where s_{xy} is the covariance of x and y , s_x^2 and s_y^2 are the variances of the x and y variables, \bar{x} and \bar{y} are their respective means, $E[(x - y)^2]$ is the estimate of the square of the expected distance to the straight line of concordance (i.e., $x = y$), $E_{indep}[(x - y)^2]$ is the same estimate by considering independence of variables.

The mean \bar{x} , the variance s_x^2 and the covariance s_{xy} are calculated, such as:

$$\bar{x} = \frac{1}{N} \sum_{n=1}^N x_n \quad \text{Equation 51}$$

$$s_x^2 = \frac{1}{N} \sum_{n=1}^N (x_n - \bar{x})^2 \quad \text{Equation 52}$$

$$s_{xy} = \frac{1}{N} \sum_{n=1}^N (x_n - \bar{x})(y_n - \bar{y}) \quad \text{Equation 53}$$

First, the agreement of two users (1 and 2) with MM was analyzed. Secondly, the average values of A , V and D obtained by both users have been calculated to provide the results of this segmentation method intended to be compared to the results of the other two methods. Thirdly, the segmentation by MM was compared with segmentation by ACM-CV. Fourthly, segmentation FTM was compared to the two previous methods for each *Amp* value. The graphs of equivalence, as well as, the Bland Altman graphs, and the Linn CCC calculations were made using free software R (R 3.2.1 software, R Foundation for Statistical Computing Vienna, Austria, 2015; [http:// www.R-project.org](http://www.R-project.org))¹⁰⁰. The CCC were expressed with 95% confidence intervals (CI). The mean average values of *Amp* associated with higher CCC were recorded directly in PDF format, and in an EXCEL spreadsheet for data numerical processing. The CCC were also plotted over the values of *Amp* ranging from 1 to 5. The maximum values of CCC and their averages resulting from the concordance analysis between the different segmentation methods were compared by the rank of Mann-Whitney-Wilcoxon and Kruskal-Wallis.

5.3 Results

5.3.1 MRI flow parameters

The 2D PC-MRI sequences performed in the five healthy volunteers corresponded to a total of 130 images compared. Table 4 summarizes the heart rate (number of heart beats per minute, bpm), the average duration of a cardiac cycle during acquisitions (in ms), and the number of phases by cardiac cycle (or N value of the cardiac cycle sampling, in absolute value), as well as their respective average (expressed in mean±SD). The results of the values of A , V and D obtained from the segmentation of each volunteer are reported in Appendix 2 to 5.

Sujets	Fréquence cardiaque (bpm)	Durée du cycle cardiaque (ms)	Nombre de phase
1	80	747	21
2	61	980	28
3	64	932	28
4	82	735	22
5	58	1032	31
Moyenne±SD	68.3±10.1	889.3±122.4	26.2±3.9

Table 5 : Characteristics of the volunteers imaged with 2D PC-MRI.

5.3.2 Manual Method : agreement analysis between two examiners

The results of the agreement analysis of the manual segmentations performed by the users 1 and 2 showed :

- A very good agreement for A values , with an estimated CCC of 0.974 [0.965,0.981].
- An excellent agreement for V values, with an estimated CCC of 0.994 [0.991,0.996].
- An excellent agreement for D values, with an estimated CCC of 0.995 [0.993,0.997].

Figure 34 illustrates these results by showing the equivalence and the Bland-Altman graphs and the histograms of differences. User 2 had a slight tendency to segment more widely than user 1, resulting in slightly larger A values. The histogram of differences shows differences of the A values ranged from -2 mm^2 to $+1 \text{ mm}^2$ and centered on -0.5 mm^2 . These results of A values resulted secondarily in slightly lower values of V and slightly higher values of D for the segmentation by user 2 compared to the values of segmentation by user 1. The differences of the V values ranged from -4 cm.s^{-1} to $+2 \text{ cm.s}^{-1}$ and were essentially centered between 0 and 1 cm.s^{-1} . The differences of D values ranged from -30 mL.min^{-1} and $+20 \text{ mL.min}^{-1}$, and were essentially centered between -10 mL.min^{-1} and 0 mL.min^{-1} .

5.3.3 Agreement analysis of the segmentations by MM and ACM-CV

The results of the agreement analysis of the segmentations performed with MM and ACM-CV showed :

- A moderate agreement for A values , with an estimated CCC of 0.934 [0.912,0.950].
- An excellent agreement for V values, with an estimated CCC of 0.993 [0.990,0.995].
- An excellent agreement for D values, with an estimated CCC of 0.982 [0.978,0.986].

Figure 35 illustrates these results by showing the equivalence, the Bland-Altman graphs and the histograms of differences. ACM-CV had a slight tendency to segment the artery sections more closely than MM, resulting in slightly smaller A values. The histogram of differences shows differences of the A values ranging from -1 mm^2 to $+3 \text{ mm}^2$ and centered on $+1.5 \text{ mm}^2$. These results of A values resulted secondarily in slightly higher values of V and slightly lower values of D for the segmentation with ACM-CV compared to the values of the segmentation with MM. The differences of the V values ranged from -3 cm.s^{-1} to -1 cm.s^{-1} and were essentially centered between -1 and 0 cm.s^{-1} . The differences of D values ranged from -10 mL.min^{-1} and $+50 \text{ mL.min}^{-1}$, and were essentially centered between 10 mL.min^{-1} and $+20 \text{ mL.min}^{-1}$.

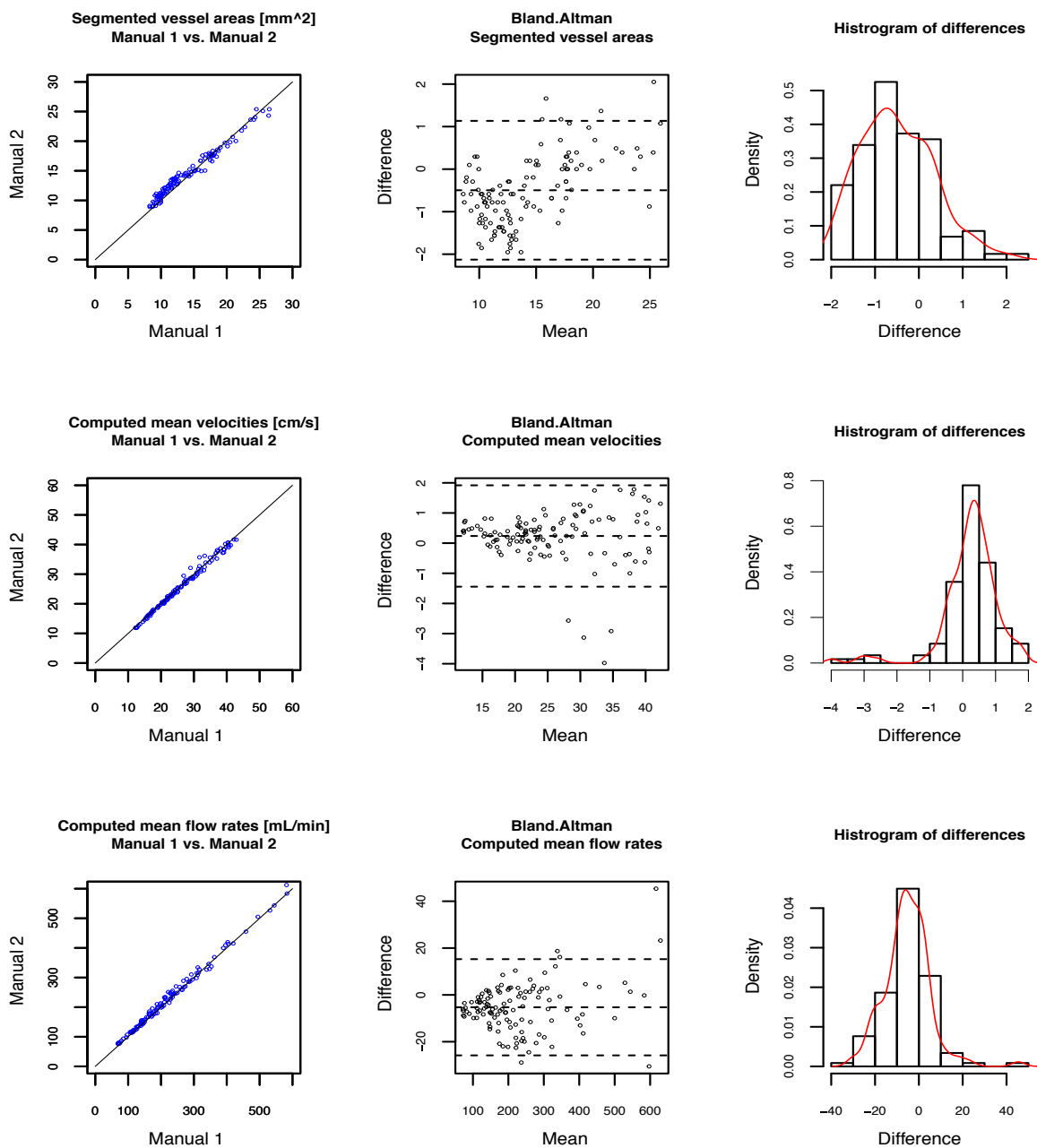


Figure 34 : Agreement analysis between manual segmentations by users 1 and by user 2.

The results of the agreement analysis of the ICA manual segmentations by the user 1 and the user 2 are presented as the equivalence (column 1), the Bland-Altman graphs (column 2) and the histograms of the differences (column 3) for the values of the calculated area (A ; row 1), mean velocities (V ; row 2) and mean flow rates and (D ; row 3). The analysis shows a good agreement between the user 1 and user 2, with small differences in values of A , V and D .

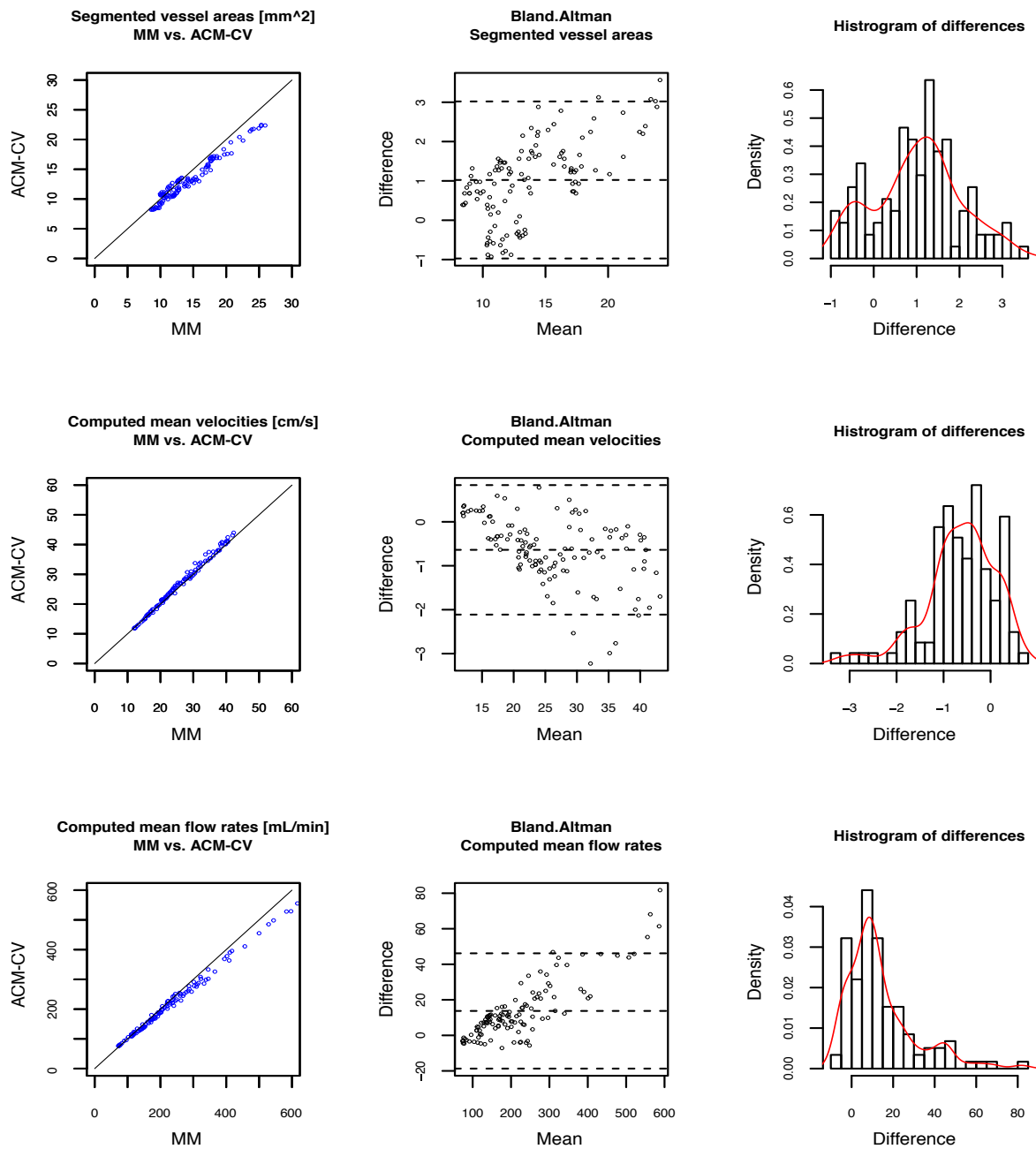


Figure 35 : Agreement analysis of MM and ACM-CV from segmentation.

The results of the ICA manual segmentations with MM and the ACM-CV are presented as the equivalence (column 1), the Bland-Altman graphs (column 2) and the histograms of the differences (column 3) for the values of the calculated area (A ; row 1), mean velocities (V ; row 2) and mean flow rates and (D ; row 3). The analysis shows a good agreement between the segmentation with MM and the segmentation ACM-CV with small differences in values of A , V and D . However, the ACM-CV tends to segment smaller areas of the arterial section compared to the MM.

5.3.4 FTM : effect of varying the amplitude threshold on the segmentation results

The ICAs were segmented with FTM for Amp values i varying from 1 to 5 (increase in 0.5 steps) except for case 1 in which the maximum increase of Amp was 4.5. The results of the 2D PC-MRI segmentation with FTM for case 1 are shown for illustrative purposes in Figure 36. They are represented as graphs of the values of A , V and D over time (i.e., $A(t)$, $V(t)$ and $D(t)$, respectively, over a cardiac cycle) for each value i of Amp . In order to not overload the present manuscript, the results of the 2D PC-MRI segmentations with FTM for the other four cases are reported in Appendix 2 to 10.

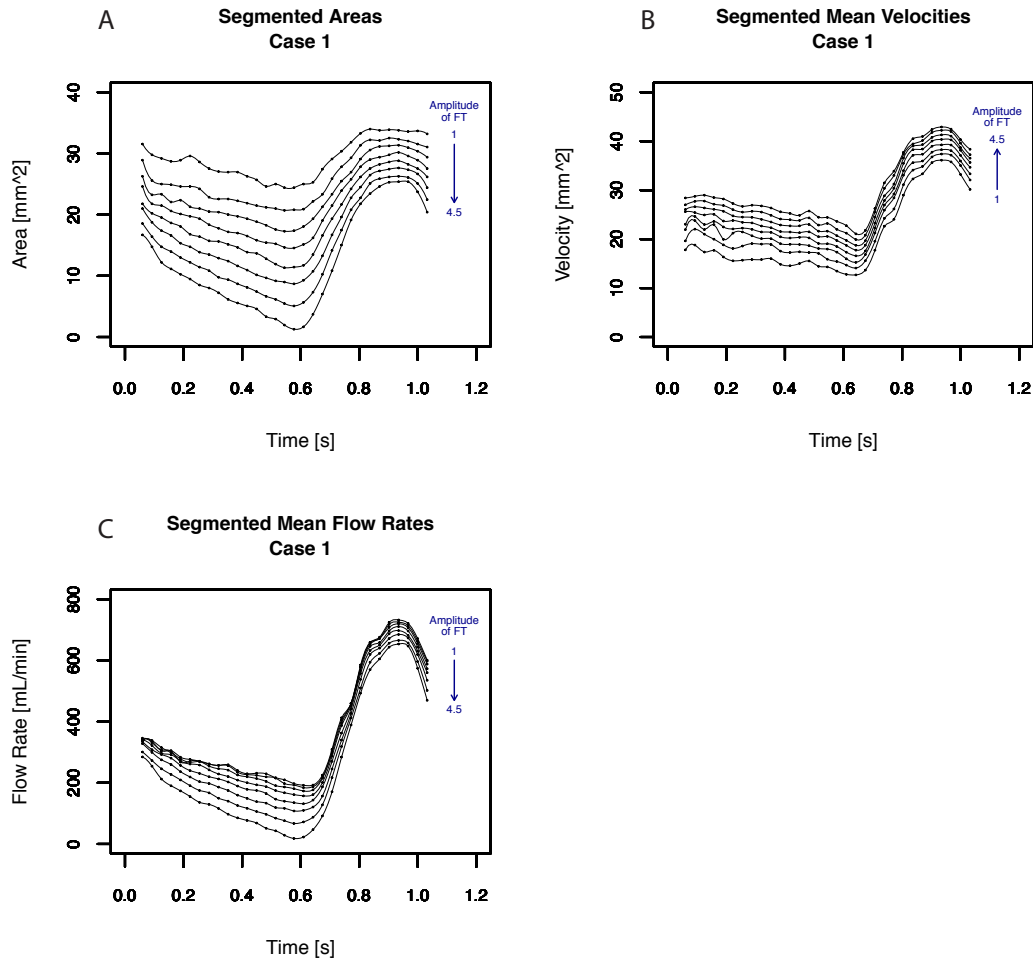


Figure 36: The impact of the FT amplitude threshold on the area, velocity and flow rate curves.

The area, the velocity and the flow rate curves over the time for each value of FT amplitude threshold (Amp) varying from 1 to 4.5 for the case 1 are represented. The increase of Amp is associated to a decrease of the area of the segmented arterial section, an increase of the velocities and a decrease of the flow rates.

5.3.4.1 Effect of the FT amplitude threshold on $A_{average}$, $V_{average}$ and $D_{average}$

The variation of Amp induced variation of $A_{average}$, $V_{average}$ and $D_{average}$ values. The increase of the Amp value was associated with the decrease of the $A_{average}_i$ values, the increase of the $V_{average}_i$ and the moderate decrease of the $D_{average}_i$ values. These variations were greater during the diastolic phase of the cardiac cycle for $A_{average}_i$ and $D_{average}_i$, and were fairly homogeneous throughout the cardiac cycle for the $V_{average}_i$ values as clearly shown by the $A(t)$, $V(t)$ and $D(t)$ curves.

On average over the five segmented ICA, the increase of *Amp* from 1 to 5 was associated with:

A decrease of $nAaverage_i$, with a mean $nAaverage_5$ of 0.38 ± 0.04 , corresponding to a mean decrease of $62\% \pm 6\%$ relatively to $nAaverage_1$.

An increase of $nVaverage_i$, with a mean $nVaverage_5$ of 1.47 ± 0.07 , corresponding to a mean increase of $47\% \pm 7\%$ relatively to $nVaverage_1$.

A decrease of $nDaverage_i$, with a mean $nDaverage_5$ of 0.61 ± 0.04 , corresponding to a mean decrease of $39\% \pm 6\%$ relatively to $nDaverage_1$.

To illustrate these results in case 1, an *Amp* value of 4.5 was associated with a $nAaverage_{4.5}$ of 0.42 (namely a decrease of 58% relatively to $nAaverage_1$), $nVaverage_{4.5}$ of 1.46 (namely a decrease of 46% relatively to $nVaverage_1$), and a $nDaverage_{4.5}$ of 0.67 (namely a decrease of 33% relatively to $nDaverage_1$).

5.3.4.2 Effect of the FT amplitude threshold on RIA, RIV and RID

The variation of *Amp* induced variation of the systolodiastolic differences of each parameter *A*, *V* and *D*, and therefore of the *RIA*, *RIV* and *RID* values. The increase of the *Amp* value was associated with an important increase of the RIA_i values, the moderate decrease of the RIV_i values and the increase of the RID_i values. These variations were clearly shown by the $A(t)$, $V(t)$ and $D(t)$ curves.

On average over the five segmented ICA, the increase of *Amp* from 1 to 5 was associated with:

A significant increase of $nRIA_i$, with a mean $nRIA_5$ of 4.38 ± 1.60 , corresponding to a mean increase of $338\% \pm 172\%$ relatively to $nRIA_1$.

A moderate decrease of $nRIV_i$, with a mean $nRIV_5$ of 0.82 ± 0.09 , corresponding to a mean decrease of $19\% \pm 9\%$ relatively to $nRIV_1$.

An increase of $nRID_i$, with a mean $nRID_5$ of 1.49 ± 0.14 , corresponding to a mean increase of $50\% \pm 16\%$ relatively to $nRID_1$.

To illustrate these results in case 1, the *Amp* value of 4.5 was associated with a $nRIA_{4.5}$ of 3.37 (namely an increase of 237% relatively to $nRIA_1$), $nRIV_{4.5}$ of 0.78 (namely a decrease of 22% relatively to $nRIV_1$), and a $nRID_{4.5}$ of 1.32 (namely an increase of 32% relatively to $nRID_1$).

5.3.4.3 Effect of the FT amplitude threshold on PIA, PIV and PID

The variation of *Amp* induced a variation of the global results of the segmentation reflected by the *IPA*, *IPV* and *IPD* values. The increase of the *Amp* value was associated with a big increase of the PIA_i values, a moderate decrease of the PIV_i values and a moderate increase of the PID_i values. These variations were clearly shown by the $A(t)$, $V(t)$ and $D(t)$ curves.

On average over the five segmented ICA, the increase of *Amp* from 1 to 5 was associated with:

A significant increase of $nPIA_i$, with a mean $nPIA_5$ of 6.93 ± 2.26 , corresponding to a mean increase of $600\% \pm 212\%$ relatively to $nPIA_1$.

A moderate decrease of $nPIV_i$, with a mean $nPIV_5$ of 0.75 ± 0.08 , corresponding to a mean decrease of $26\% \pm 9\%$ relatively to $nPID_1$.

An increase of $nPID_i$, with a mean $nPID_5$ of 1.91 ± 0.22 , corresponding to a mean increase of $99\% \pm 31\%$ relatively to $nPID_1$.

To illustrate these results in case 1, the Amp value of 4.5 was associated with a $nPIA_{4.5}$ of 6.05 (namely an increase of 505% relatively to $nPIA_1$), $nPIV_{4.5}$ of 0.64 (namely a decrease of 36% relatively to $nPIV_1$), and a $nPID_{4.5}$ of 1.75 (namely an increase of 75% relatively to $nPID_1$).

The effects of the Amp variation on the global results of the segmentations with the FTM are illustrated in Figure 37 representing the $nAaverage(i)$, $nVaverage(i)$, $nDaverage(i)$, $nRIA(i)$, $nRIA(i)$, $nRIA(i)$, $nPIA(i)$, $nPIA(i)$ and $nPIA(i)$ curves for the case 1.

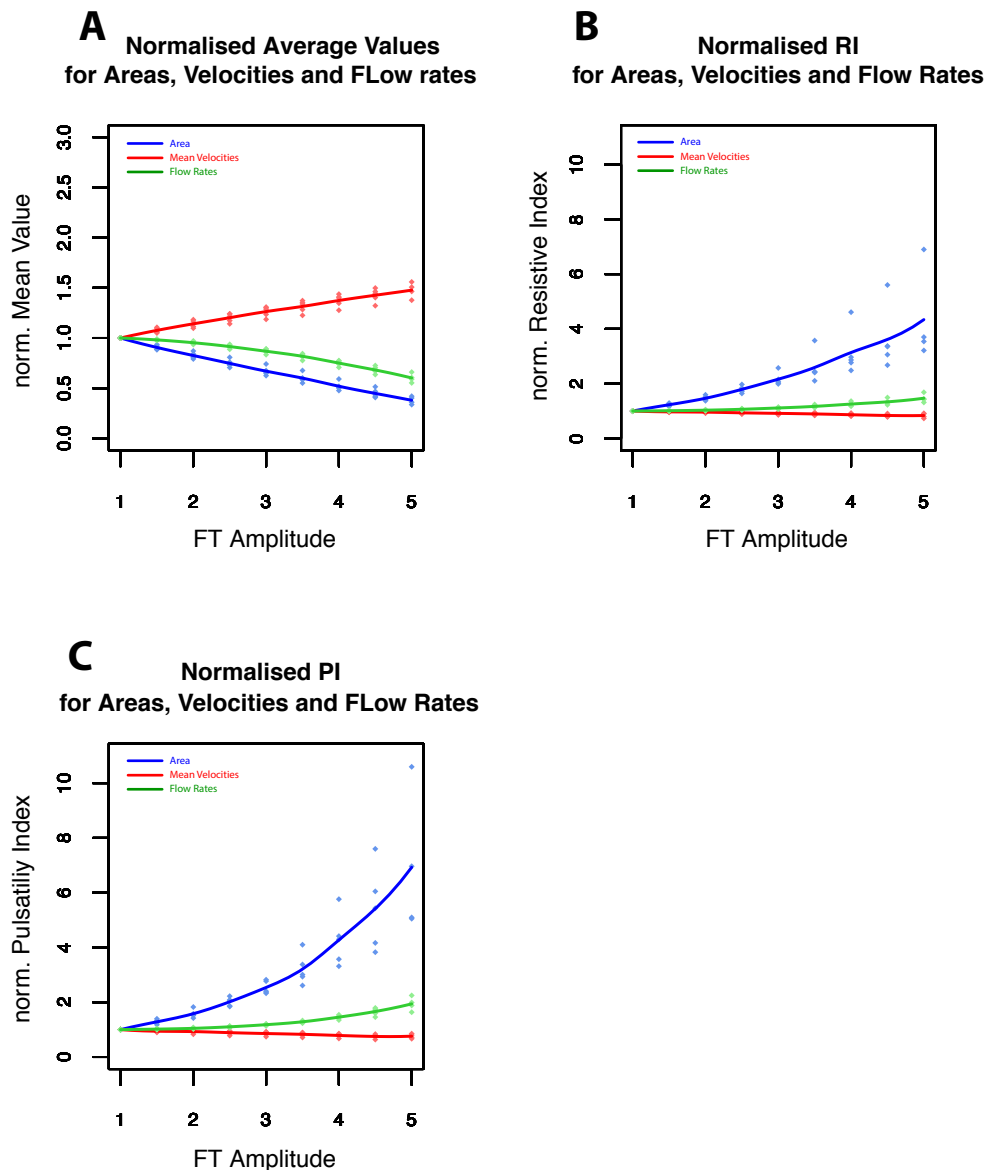


Figure 37: The impact of the Amp on the normalised area, Average, RI and PI values of A, V and D.

The curve of the normalised Average, RI and PI values for the segmented area (blue curves), mean velocities (red curves) and flow rates (green curves) are represented. The area curves for average, RI and PI values are the most impacted variables compared to the mean velocities (red curves) and flow rate (green curves). The most impacted parameters is the PI for the area of the segmented arterial section (blue curve – graph C). The less impacted parameters is the RI for the mean velocities (red curve – graph B).

5.3.5 Agreement analysis : FTM versus MM and FTM versus ACM-CV

The CCC values of the agreement analysis firstly between FTM and MM segmentations and secondly between the FTM and ACM-CV segmentations are reported in Annexe 6 to 10. The detailed results of the agreement analysis and the corresponding CCC values are detailed for each case and each *i* value of *Amp*.

A poor agreement for the results of *A* values was shown between the FTM and the other two methods of segmentation. Maximum mean values of CCC were 0.772 ± 0.157 (mean *Amp* of 3.00 ± 0.35 , median = 3.00) when compared to the MM and 0.530 ± 0.129 (mean *Amp* of 3.10 ± 0.22 , median = 3.00) when compared to the ACM-CV, with no significant difference between the two comparison ($P=0.31$). The mean *Amp* values associated with maximum values of CCC showed no significant difference ($P=0.70$).

An excellent agreement was shown for the results of *V* values between the FTM and the other two methods, with a slight superiority of agreement between FTM and MM in comparison to FTM and ACM-CV. The average values of maximum CCC were 0.983 ± 0.006 (mean *Amp* of 2.70 ± 0.27 , median = 2.50) when compared to the MM and 0.981 ± 0.005 (mean *Amp* of 3.00 ± 0.00 , median = 30) when compared to the ACM-CV, with no significant difference ($P=0.59$). The *Amp* values associated with maximum values of CCC were slightly lower when compared to the MM in comparison to when compared to the ACM-CV, with no significant difference ($P=0.28$).

An excellent agreement was shown for the results of *D* values between the FTM and the other two methods, with a slight superiority of agreement between FTM and MM in comparison to FTM and ACM-CV. The average values of maximum CCC were 0.980 ± 0.012 (mean *Amp* of 3.00 ± 0.00 , median = 3.00) when compared to the MM and 0.960 ± 0.027 (mean *Amp* of 3.30 ± 0.27 , median = 3.50) when compared to the ACM-CV, with no significant difference ($P=0.29$). The *Amp* values associated with maximum values of CCC were slightly lower when compared to the MM in comparison to when compared to the ACM-CV, with no significant difference ($P=0.07$).

An additional analysis of the CCC values was performed by averaging all CCC values according to the *Amp* values. The curves of the averaged CCC for the five subjects as a function of *Amp* values illustrate these results in Figure 38 “bell shape” of the curves, marked for the CCC values related to the agreement for the *A* values. Low average CCC values were associated with poor agreement for *A* values between the FTM and the MM, and also between the FTM and the ACM-CV (maximal average CCC of 0.763 ± 0.155 and 0.596 ± 0.129 , respectively). The average CCC values were higher for the *V* values (0.978 ± 0.010 and 0.981 ± 0.005 for the analysis between FTM and MM, and for the analysis between FTM and ACM-CV, respectively) and for the *D* values (0.980 ± 0.012 and 0.952 ± 0.031 for the analysis between FTM and MM, and for the analysis between FTM and ACM-CV, respectively). The highest average CCC values of agreement for the values of *A*, *V* and *D* were obtained for values of *Amp* ranging from 2.5 to 3.5.

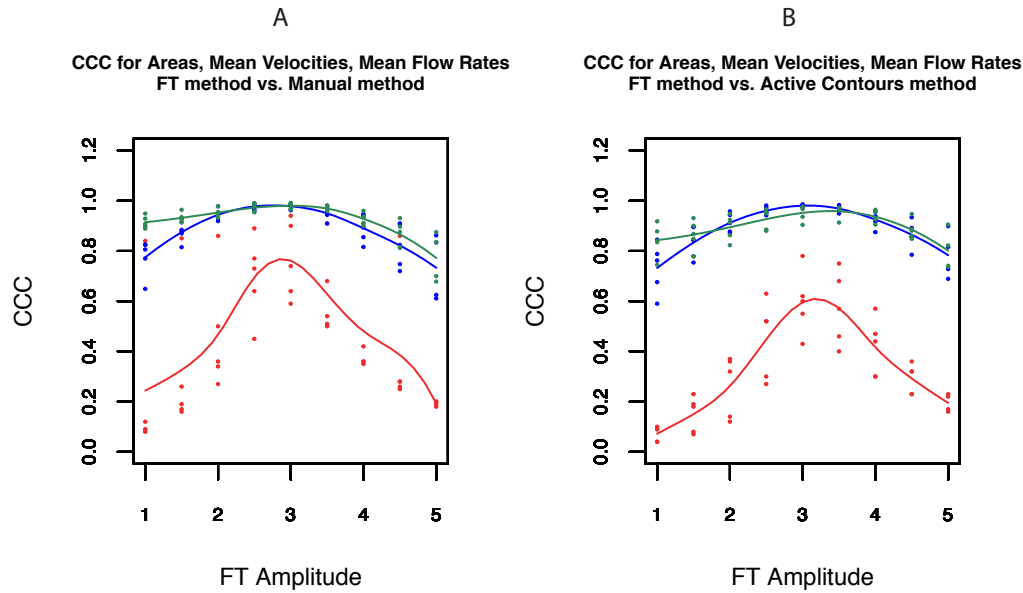


Figure 38: Evolution of the CCC values averaged on the five subjects as function of Amp.

The graphs show the evolution of the averaged CCC values for the analysis between the FTM and MM (Graph A, left) and between FTM and ACM-CV (Graph B, right). It shows "bell shaped" curves with excellent CCC values for the velocity (blue curves) and flow rate (green curves) for Amp values varying between 2.5 and 3.5. The curves of CCC values for the segmented area values were lower than the other in favor of a poor agreement for this parameter.

5.4 Discussion

As we have previously pointed out, segmentation is the first step in the process of interpreting an image. In medical imaging, image segmentation is the key step in the analysis and extraction of the "useful" information necessary for physicians.

We suggested a new segmentation method for 2D PC-MRI based on an analysis of the FT of the images. The algorithm integrates the temporal coherence of the velocities in the vessels to discriminate the vascular voxels from the surrounding noise voxels. The originality of this approach relies in a FT analysis of the phase image using a sliding window based on a Kernel of 5 images in order to take into account the velocities within a voxel over time. We characterized the method and its behavior for the segmentation of 2D PC-MRI images of the ICA in five healthy subjects. We analyzed the impact of the *Amp* variation on the results of the segmentations, with regard to the obtained values for the areas (*A*) of the segmented arterial sections, the mean velocities (*V*) and mean flow rates (*D*) through this latter. Secondly, the results of the segmentation were compared with two other segmentation methods widely used in medical imaging: MM and ACM-CV⁸⁰.

FTM allows the automatic segmentation of ICA in 2D PC-MRI images without user intervention with varying results according to the parameter of interest (areas, mean velocities or mean flow rates) and depending on the chosen amplitude threshold of the FT (*Amp*). this latter has been shown to have a big impact on the segmentation results, particularly with regard to the area values. The increase of this threshold was associated with a significant decrease in the area values of the segmented arterial section, particularly during the diastolic phase of the cardiac cycle. Changes were also shown for the mean velocities (which in

contrary increased) and mean flow rates values (which also decreased), but to a lesser extent. The variation of the mean velocity values were more homogeneous and affected all the time points during the cardiac cycle, whereas the variation of the mean flow rates affected preferential time points during the diastolic phase.

The *RI* and *PI* equivalent indexes for the analysis of the areas, mean velocity and mean flow rate curves (i.e., *RIA*, *PIA*, *RIV*, *PIV*, *RID* and *PID*, respectively) also presented variations with the increase of the *Amp* value. It increased the *RI* values for areas and mean flow rates, whereas the *RI* decreased moderately for the mean velocities. It increased the *PI* values for areas and mean flow rates, whereas the *PI* decreased moderately for the mean velocities.

The agreement analysis between the FTM and MM, and between the FTM and ACM-CV for the segmentation of the ICA in healthy volunteers showed a good agreement between the segmentations with MM and ACM-CV. Nevertheless, the first method showed a slight tendency (but not significant) to segment larger areas than the second method. This slight difference could be explained by the application of the ACM-CV on the magnitude images. Therefore, its accuracy is dependent on the natural contrast of these images which can be limited. The agreement analysis showed low concordance between the FTM and the two other methods for the results of the calculated areas of the arterial section. But this low concordance did not seem to have any impact on the agreement degree between the methods for the calculation of the mean velocities and mean flow rate values which were very good.

The change of *Amp* mainly affected the results of mean values of area values (*Aaverage*), the systolo diastolic difference of the area values (*RIA*) and the pulsatility index for the areas (*PIA*). The least sensitive parameter to the variation of the FT amplitude threshold was the *RI* for the mean velocities (*RIV*).

These variations of the FTM results depending on the FT amplitude threshold (*Amp*) are important to consider in the use of this new method. Indeed, the FTM is a fully automatic method that can be used reliably for the segmentation of the ICA imaged by 2D PC-MRI for *Amp* values ranging from 2.5 to 3.5. For these values of *Amp*, the results of the segmentation with FTM are very consistent with the results of segmentations obtained with MM and ACM-CV. The impact of the *Amp* is not minimal. The *RI* values for mean velocities were the least impacted by this threshold variation.

CHAPTER 6

6 General conclusion

This work was conducted through transversal approach combining *in vitro* experiments and *in vivo* investigations (clinical and by imaging).

First, we have demonstrated by combining *in vitro* and *in vivo* investigations that the aneurysm induces a significant decrease of the resistance in the parent vessel segment downstream to the aneurysm. This effect was measurable *in vitro* as a decrease in the hydraulic resistance of the circuit embedded in the test bench, and *in vivo* as a significant decrease of the resistive and pulsatility indexes associated to a demodulated (dampened) flow within the parent vessel segment downstream to the aneurysm. *In vivo*, the impact of the aneurysm was characterized by a decrease in the *RI* and *PI* in the downstream arterial segment. This effect was significantly correlated to its volume. *In vitro*, given the experimental conditions (negligible capacitance and constant flow rate) only the variations in resistance were assessed by measuring the pressures. However, the capacitance might also be involved in the effect of the aneurysm on the parent vessel *in vivo*. Indeed, the wall mechanical properties of the parent artery change at the level of the aneurysm which have a thinner wall¹¹⁰⁻¹¹². The reduction of the wall thickness as well as the increase of arterial volume corresponding to the malformation increase the distensibility and therefore the capacitance of the diseased segment. As reported by some authors, the increased distensibility of the aneurysm seems to predominate at its dome¹¹⁰⁻¹¹². One can reasonably assume that large aneurysms present larger domes and therefore should induce more of impact on flow by an increase of their capacitance.

By analogy to an electric circuit, our results suggest that the aneurysm behaves like the combination of a resistor and a capacitor on the blood flow stream, so as a RC circuit (a resistor – capacitor circuit) does act on the electric stream. The resistive property of the aneurysm would be related to its diameter change (increase), while its capacitance property would be related to the aneurysmal mechanical properties (volume and biomechanical properties of the wall). By dampening the flow as observed *in vivo* through the VFR waveform analysis, the aneurysms seem to have a low-pass filter which strongly depends on their volume. This latter might explain the demodulated and slow flow observed in the arterial bed downstream to the aneurysm.

This work allowed us to move forward in the understanding of aneurysmal disease. It highlighted new insights on the complex aneurysm – parent vessel relation, and on its impact on the downstream arterial bed. The hemodynamic changes in both the parent vessel and the aneurysmal sac are indissociable for a better understanding of intracranial aneurysmal disease. Although the assimilation of the aneurysm to an RC circuit presenting a low-pass filter might be simplistic, conceptually, it may have some significant implications in perspective of research and in clinical practice. Indeed, the understanding of the aneurysm and its consequences on the cerebral blood flow might be approached by an equivalent of electrical circuit model (lumped model). Because of the complexity of cerebral vasculature and its

regulation, *in vitro* (*in silico*) and *in vivo* experiments for aneurysm disease comprehension are complex to enforce. Lumped-parameter models help to recreate and understand several flow aspects of a system (including among others the effects of wall elasticity and compliance). They are able to quantitatively and qualitatively describe pressure and flow waveforms without providing detailed solution on, mainly, local phenomena. They do provide a reasonable initial means to assess the overall system behaviour, and have a great potential to perform fast, easy and scalable studies on the influence of individual parameters. This approach has been widely used for cardiovascular diseases¹²⁵. Very little works have been applied for intracranial vessels and none on the aneurysms^{126 127}. This approach should be developed for the research on aneurysm disease.

From a clinical point of view, it allows us to make assumptions about some complications reported after treatment of large aneurysms. One can reasonably assume that the sudden increase of the arterial resistance (with increased arterial *RI* and *PI*) in a probably long-standing dampened blood flow in the downstream arterial bed (i.e., with a decreased arterial *RI* and *PI*) within the ipsilateral hemisphere might play a role in the intra parenchymal haemorrhage or in hyperperfusion syndromes that have been previously reported after the treatment of large aneurysms either by clipping or by endovascular techniques^{35,114,115}. Like in chronic carotid stenosis, the long-standing dampened flow in the downstream arterial bed due to the aneurysm effect is probably responsible for an impairment of the cerebral autoregulation. Within certain limits, even if their primary pathophysiological mechanisms are clearly different (arterial narrowing in carotid stenosis versus arterial dilatation in aneurysm disease), the giant aneurysms and the carotid chronic stenosis seem to have the same consequence on the downstream flow. This potential implication of giant aneurysms in cerebral hyperperfusion after their treatment should be investigated by studies including pre- and post- operative perfusion imaging. The acute correction of the aneurysm effect after FDS deployment raises the question of blood pressure control after the endovascular treatment of giant aneurysm. Similarly, the EVT of those aneurysms might also be considered by stages: an initial (incomplete) coiling session followed by a postponed FDS deployment. This more progressive strategy might allow the recovery of an efficient cerebral autoregulation. We did not observe such complications in our series of patients.

Second, we proposed a new and fully automated segmentation method for 2D PC-MRI based on an analysis of the FT of the images. The algorithm integrates the temporal coherence of the velocities in the vessels to discriminate the vascular voxels from the surrounding noise voxels. In five healthy subjects, the method allowed for the segmentation of the cervical ICAs. The results of the agreement analysis between the FTM and two widely used methods for image segmentation (i.e., MM and ACM-CV) showed promising result. The significant impact of the FT amplitude value (threshold) on the results of the segmentation has to be considered in the use of this new method. Its efficacy on larger and smaller arteries has to be tested on larger studies.

From the point of view of research, our work had important links with several ongoing research projects. The implication of the parent vessel flow changes in aneurysm vulnerability has not been investigated in our work. This point might be addressed by the ANEUVYSM (ANEurysm Vulnerability Index assessment by Simulation and Medical imaging) research project. This ongoing clinical study has been promoted by the department of neuroradiology at the University Hospital of Montpellier since 2014. It aims to evaluate the aneurysm vulnerability by establishing a multi composite index. Two groups of patients with intracranial aneurysms are compared according to whether the aneurysm ruptures or not. All

patients are imaged before the endovascular treatment. The results of this work and especially the flow analysis methodology and the FTM methods for 2D PC-MRI have been integrated into the study protocol.

Published articles

MR derived volumetric flow rate waveforms of internal carotid artery in patients treated for unruptured intracranial aneurysms by flow diversion technique.

Eker OF, Boudjeltia KZ, Jerez RA, Le Bars E, Sanchez M, Bonafé A, Costalat V, Courbebaisse G.

J Cereb Blood Flow Metab. 2015. PMID : 26264871

Determination of a shear rate threshold for thrombus formation in intracranial aneurysms.

Ribeiro de Sousa D, Vallecilla C, Chodzynski K, Corredor Jerez R, Malaspina O, **Eker OF**, Ouared R, Vanhamme L, Legrand A, Chopard B, Courbebaisse G, Zouaoui Boudjeltia K.

J Neurointerv Surg. 2015. PMID : 26215274

Intracranial Aneurysms : Wall Motion Analysis for Prediction of Rupture.

Vanrossomme AE, **Eker OF**, Thiran JP, Courbebaisse GP, Zouaoui Boudjeltia K.

AJNR Am J Neuroradiol. 2015. PMID : 25929878

Intracranial aneurysmal pulsatility as a new individual criterion for rupture risk evaluation : biomechanical and numeric approach (IRRAs Project).

Sanchez M, **Ecker O**, Ambard D, Jourdan F, Nicoud F, Mendez S, Lejeune JP, Thines L, Dufour H, Brunel H, Machi P, Lobotesis K, Bonafé A, Costalat V.

AJNR Am J Neuroradiol. 2014. PMID : 24852288

Experimental measures of human intracranial arteries wall properties.

Lafon B, **Eker O**, Ambard D, Costalat V, Sanchez M, Baldit A, Jourdan F.

Comput Methods Biomech Biomed Engin. 2013. PMID : 23923954

Extra-aneurysmal flow modification following pipeline embolization device implantation : focus on regional branches, perforators, and the parent vessel.

Gascou G, Lobotesis K, Brunel H, Machi P, Riquelme C, **Eker O**, Bonafé A, Costalat V.

AJNR Am J Neuroradiol. 2015. PMID : 25523592

References

7 References

1. Juvela, S., Porras, M. & Poussa, K. Natural history of unruptured intracranial aneurysms: probability of and risk factors for aneurysm rupture. *J Neurosurg* **93**, 379-387 (2000).
2. Castro, M.A. Understanding the Role of Hemodynamics in the Initiation, Progression, Rupture, and Treatment Outcome of Cerebral Aneurysm from Medical Image-Based Computational Studies. *ISRN Radiology* **2013**, 17 (2013).
3. Clarke, M. Systematic review of reviews of risk factors for intracranial aneurysms. *Neuroradiology* **50**, 653-664 (2008).
4. Juvela, S. Prevalence of and risk factors for intracranial aneurysms. *Lancet Neurol* **10**, 595-597 (2011).
5. Greving, J.P., *et al.* Development of the PHASES score for prediction of risk of rupture of intracranial aneurysms: a pooled analysis of six prospective cohort studies. *Lancet Neurol* **13**, 59-66 (2014).
6. van Gijn, J., Kerr, R.S. & Rinkel, G.J. Subarachnoid haemorrhage. *Lancet* **369**, 306-318 (2007).
7. Rinkel, G.J. Natural history, epidemiology and screening of unruptured intracranial aneurysms. *Journal of neuroradiology. Journal de neuroradiologie* **35**, 99-103 (2008).
8. Vlak, M.H., Algra, A., Brandenburg, R. & Rinkel, G.J. Prevalence of unruptured intracranial aneurysms, with emphasis on sex, age, comorbidity, country, and time period: a systematic review and meta-analysis. *Lancet Neurol* **10**, 626-636 (2011).
9. Zipfel, G.J. & Dacey, R.G. Update on the management of unruptured intracranial aneurysms. *Neurosurg Focus* **17**, E2 (2004).
10. Molyneux, A., *et al.* International Subarachnoid Aneurysm Trial (ISAT) of neurosurgical clipping versus endovascular coiling in 2143 patients with ruptured intracranial aneurysms: a randomised trial. *Lancet* **360**, 1267-1274 (2002).
11. Molyneux, A.J., *et al.* International subarachnoid aneurysm trial (ISAT) of neurosurgical clipping versus endovascular coiling in 2143 patients with ruptured intracranial aneurysms: a randomised comparison of effects on survival, dependency, seizures, rebleeding, subgroups, and aneurysm occlusion. *Lancet* **366**, 809-817 (2005).
12. Molyneux, A.J. & Kerr, R.S. The future management of subarachnoid haemorrhage. *Journal of neuroradiology. Journal de neuroradiologie* **29**, 74-75 (2002).
13. Derrey, S., *et al.* French collaborative group series on giant intracranial aneurysms: Current management. *Neurochirurgie* **61**, 371-377 (2015).
14. Molyneux, A., *et al.* International Subarachnoid Aneurysm Trial (ISAT) of neurosurgical clipping versus endovascular coiling in 2143 patients with

- ruptured intracranial aneurysms: a randomised trial. *Lancet* **360**, 1267-1274 (2002).
15. Lindsay, K.W. The impact of the International Subarachnoid Aneurysm Treatment Trial (ISAT) on neurosurgical practice. *Acta Neurochir (Wien)* **145**, 97-99 (2003).
 16. Derdeyn, C.P., *et al.* The International Subarachnoid Aneurysm Trial (ISAT): a position statement from the Executive Committee of the American Society of Interventional and Therapeutic Neuroradiology and the American Society of Neuroradiology. *AJNR Am J Neuroradiol* **24**, 1404-1408 (2003).
 17. Michael, W.F. Posterior fossa aneurysms simulating tumours. *J Neurol Neurosurg Psychiatry* **37**, 218-223 (1974).
 18. German, W.J. & Black, S.P. Intra-aneurysmal hemodynamics-jet action. *Circ Res* **3**, 463-468 (1955).
 19. Busse, O. & Grote, E. Recurrent cerebral embolization from a carotid bifurcation aneurysm. *Acta Neurochir (Wien)* **62**, 203-206 (1982).
 20. Peiris, J.B. & Ross Russell, R.W. Giant aneurysms of the carotid system presenting as visual field defect. *J Neurol Neurosurg Psychiatry* **43**, 1053-1064 (1980).
 21. Sadik, A.R., Budzilovich, G.N. & Shulman, K. Giant Aneurysm of Middle Cerebral Artery: A Case Report. *J Neurosurg* **22**, 177-181 (1965).
 22. Choi, I.S. & David, C. Giant intracranial aneurysms: development, clinical presentation and treatment. *Eur J Radiol* **46**, 178-194 (2003).
 23. Gonzalez, N.R., Duckwiler, G., Jahan, R., Murayama, Y. & Vinuela, F. Challenges in the endovascular treatment of giant intracranial aneurysms. *Neurosurgery* **59**, S113-124; discussion S113-113 (2006).
 24. Debrun, G., *et al.* Giant unclippable aneurysms: treatment with detachable balloons. *AJNR Am J Neuroradiol* **2**, 167-173 (1981).
 25. Mathis, J.M., *et al.* Temporary balloon test occlusion of the internal carotid artery: experience in 500 cases. *AJNR Am J Neuroradiol* **16**, 749-754 (1995).
 26. Zhang, Y., *et al.* Comparison of the flow diverter and stent-assisted coiling in large and giant aneurysms: safety and efficacy based on a propensity score-matched analysis. *Eur Radiol* (2015).
 27. Gao, X., Liang, G., Li, Z., Wei, X. & Cao, P. A single-centre experience and follow-up of patients with endovascular coiling of large and giant intracranial aneurysms with parent artery preservation. *Journal of clinical neuroscience : official journal of the Neurosurgical Society of Australasia* **19**, 364-369 (2012).
 28. Chalouhi, N., *et al.* Coiling of large and giant aneurysms: complications and long-term results of 334 cases. *AJNR Am J Neuroradiol* **35**, 546-552 (2014).
 29. Wang, B., Gao, B.L., Xu, G.P., Xiang, C. & Liu, X.S. Endovascular embolization is applicable for large and giant intracranial aneurysms: experience in one center with long-term angiographic follow-up. *Acta Radiol* **56**, 105-113 (2015).
 30. Consoli, A., *et al.* Assisted coiling of saccular wide-necked unruptured intracranial aneurysms: stent versus balloon. *Journal of neurointerventional surgery* **8**, 52-57 (2016).
 31. Byrne, J.V., Beltechi, R., Yarnold, J.A., Birks, J. & Kamran, M. Early experience in the treatment of intra-cranial aneurysms by endovascular flow diversion: a multicentre prospective study. *PloS one* **5**(2010).

32. Szikora, I., *et al.* Treatment of intracranial aneurysms by functional reconstruction of the parent artery: the Budapest experience with the pipeline embolization device. *AJNR Am J Neuroradiol* **31**, 1139-1147 (2010).
33. Zanaty, M., *et al.* Flow diversion for complex middle cerebral artery aneurysms. *Neuroradiology* **56**, 381-387 (2014).
34. Lanzino, G., Crobeddu, E., Cloft, H.J., Hanel, R. & Kallmes, D.F. Efficacy and safety of flow diversion for paraclinoid aneurysms: a matched-pair analysis compared with standard endovascular approaches. *AJNR Am J Neuroradiol* **33**, 2158-2161 (2012).
35. Brinjikji, W., Murad, M.H., Lanzino, G., Cloft, H.J. & Kallmes, D.F. Endovascular treatment of intracranial aneurysms with flow diverters: a meta-analysis. *Stroke* **44**, 442-447 (2013).
36. Arrese, I., Sarabia, R., Pintado, R. & Delgado-Rodriguez, M. Flow-diverter devices for intracranial aneurysms: systematic review and meta-analysis. *Neurosurgery* **73**, 193-199; discussion 199-200 (2013).
37. Murthy, S.B., *et al.* The SILK flow diverter in the treatment of intracranial aneurysms. *Journal of clinical neuroscience : official journal of the Neurosurgical Society of Australasia* **21**, 203-206 (2014).
38. D'Urso, P.I., Lanzino, G., Cloft, H.J. & Kallmes, D.F. Flow diversion for intracranial aneurysms: a review. *Stroke* **42**, 2363-2368 (2011).
39. Lubicz, B., *et al.* Flow-diverter stent for the endovascular treatment of intracranial aneurysms: a prospective study in 29 patients with 34 aneurysms. *Stroke* **41**, 2247-2253 (2010).
40. Cebal, J.R., Mut, F., Weir, J. & Putman, C. Quantitative characterization of the hemodynamic environment in ruptured and unruptured brain aneurysms. *AJNR Am J Neuroradiol* **32**, 145-151 (2011).
41. Cebal, J.R., Mut, F., Weir, J. & Putman, C.M. Association of hemodynamic characteristics and cerebral aneurysm rupture. *AJNR Am J Neuroradiol* **32**, 264-270 (2011).
42. Chen, H., *et al.* Investigating the influence of haemodynamic stimuli on intracranial aneurysm inception. *Annals of biomedical engineering* **41**, 1492-1504 (2013).
43. Jiang, J., *et al.* Comparison of blood velocity measurements between ultrasound Doppler and accelerated phase-contrast MR angiography in small arteries with disturbed flow. *Physics in medicine and biology* **56**, 1755-1773 (2011).
44. Marzo, A., *et al.* Computational hemodynamics in cerebral aneurysms: the effects of modeled versus measured boundary conditions. *Annals of biomedical engineering* **39**, 884-896 (2011).
45. Karmonik, C., *et al.* Temporal variations of wall shear stress parameters in intracranial aneurysms--importance of patient-specific inflow waveforms for CFD calculations. *Acta Neurochir (Wien)* **152**, 1391-1398; discussion 1398 (2010).
46. Sforza, D.M., Putman, C.M. & Cebal, J.R. Hemodynamics of Cerebral Aneurysms. *Annual review of fluid mechanics* **41**, 91-107 (2009).
47. Castro, M.A., Putman, C.M. & Cebal, J.R. Computational fluid dynamics modeling of intracranial aneurysms: effects of parent artery segmentation on intra-aneurysmal hemodynamics. *AJNR Am J Neuroradiol* **27**, 1703-1709 (2006).

48. Cebral, J.R., *et al.* Hemodynamics in Normal Cerebral Arteries: Qualitative Comparison of 4D Phase-Contrast Magnetic Resonance and Image-Based Computational Fluid Dynamics. *Journal of engineering mathematics* **64**, 367-378 (2009).
49. Larrabide, I., *et al.* Intra-aneurysmal pressure and flow changes induced by flow diverters: relation to aneurysm size and shape. *AJNR Am J Neuroradiol* **34**, 816-822 (2013).
50. Evans, D.H. & McDicken, W.N. *Doppler Ultrasound: Physics, Instrumentation and Signal Processing*, (Wiley, 2000).
51. Akif Topcuoglu, M. Transcranial Doppler ultrasound in neurovascular diseases: diagnostic and therapeutic aspects. *Journal of neurochemistry* **123**, 39-51 (2012).
52. Levitt, M.R., *et al.* Cerebral aneurysms treated with flow-diverting stents: computational models with intravascular blood flow measurements. *AJNR Am J Neuroradiol* **35**, 143-148 (2014).
53. Torii, R., *et al.* A computational study on the influence of catheter-delivered intravascular probes on blood flow in a coronary artery model. *J Biomech* **40**, 2501-2509 (2007).
54. Mynard, J.P., Wasserman, B.A. & Steinman, D.A. Errors in the estimation of wall shear stress by maximum Doppler velocity. *Atherosclerosis* **227**, 259-266 (2013).
55. Stalder, A.F., *et al.* Quantitative 2D and 3D phase contrast MRI: optimized analysis of blood flow and vessel wall parameters. *Magnetic resonance in medicine : official journal of the Society of Magnetic Resonance in Medicine / Society of Magnetic Resonance in Medicine* **60**, 1218-1231 (2008).
56. van Raamt, A.F., Appelman, A.P., Mali, W.P., van der Graaf, Y. & Group, S.S. Arterial blood flow to the brain in patients with vascular disease: the SMART Study. *Radiology* **240**, 515-521 (2006).
57. Zhao, M., *et al.* Regional cerebral blood flow using quantitative MR angiography. *AJNR Am J Neuroradiol* **28**, 1470-1473 (2007).
58. Amin-Hanjani, S., *et al.* Use of quantitative magnetic resonance angiography to stratify stroke risk in symptomatic vertebrobasilar disease. *Stroke* **36**, 1140-1145 (2005).
59. Hollnagel, D.I., Summers, P.E., Poulikakos, D. & Kollias, S.S. Comparative velocity investigations in cerebral arteries and aneurysms: 3D phase-contrast MR angiography, laser Doppler velocimetry and computational fluid dynamics. *NMR in biomedicine* **22**, 795-808 (2009).
60. Spilt, A., *et al.* Reproducibility of total cerebral blood flow measurements using phase contrast magnetic resonance imaging. *J Magn Reson Imaging* **16**, 1-5 (2002).
61. Schneiders, J.J., *et al.* Comparison of phase-contrast MR imaging and endovascular sonography for intracranial blood flow velocity measurements. *AJNR Am J Neuroradiol* **33**, 1786-1790 (2012).
62. Brown, R.W., Cheng, Y.C.N., Haacke, E.M., Thompson, M.R. & Venkatesan, R. *Magnetic Resonance Imaging: Physical Principles and Sequence Design*, (Wiley, 2014).
63. Lee, V.S. *Cardiovascular MRI: Physical Principles to Practical Protocols*, (Lippincott Williams & Wilkins, 2006).
64. Kastler, B. & Vetter, D. *Comprendre l'IRM: Manuel d'auto-apprentissage*, (Elsevier Health Sciences France, 2011).

65. Meckel, S., *et al.* Intracranial artery velocity measurement using 4D PC MRI at 3 T: comparison with transcranial ultrasound techniques and 2D PC MRI. *Neuroradiology* **55**, 389-398 (2013).
66. Wetzel, S., *et al.* In vivo assessment and visualization of intracranial arterial hemodynamics with flow-sensitized 4D MR imaging at 3T. *AJNR Am J Neuroradiol* **28**, 433-438 (2007).
67. Setarehdan, S.K. & Singh, S. *Advanced Algorithmic Approaches to Medical Image Segmentation: State-of-the-Art Applications in Cardiology, Neurology, Mammography and Pathology*, (Springer London, 2012).
68. El-Baz, A.S., U, R.A., Mirmehdi, M. & Suri, J.S. *Multi Modality State-of-the-Art Medical Image Segmentation and Registration Methodologies*, (Springer US, 2011).
69. Kozerke, S., *et al.* Automatic vessel segmentation using active contours in cine phase contrast flow measurements. *J Magn Reson Imaging* **10**, 41-51 (1999).
70. Rousselle, J.-J. Tours (2003).
71. McInerney, T. & Terzopoulos, D. Deformable models in medical image analysis: a survey. *Medical image analysis* **1**, 91-108 (1996).
72. Pham, D.L., Xu, C. & Prince, J.L. Current methods in medical image segmentation 1. *Annual review of biomedical engineering* **2**, 315-337 (2000).
73. Pal, N.R. & Pal, S.K. A review on image segmentation techniques. *Pattern recognition* **26**, 1277-1294 (1993).
74. Montagnat, J., Delingette, H. & Ayache, N. A review of deformable surfaces: topology, geometry and deformation. *Image and vision computing* **19**, 1023-1040 (2001).
75. Cocquerez, J.P. & Philipp-Foliguet, S. *Analyse d'images: filtrage et segmentation*. (1995).
76. Herbulot, A. INRIA (Rennes (2010).
77. Haralick, R.M. & Shapiro, L.G. Image segmentation techniques. *Computer vision, graphics, and image processing* **29**, 100-132 (1985).
78. Monga, O. & Wrobel, B. Segmentation d'images: vers une méthodologie. *TS Traitement du signal* **4**, 169-193 (1987).
79. Burr, D.J. Elastic matching of line drawings. *IEEE Transactions on Pattern Analysis & Machine Intelligence*, 708-713 (1981).
80. Chan, T.F. & Vese, L.A. Active contours without edges. *IEEE transactions on image processing : a publication of the IEEE Signal Processing Society* **10**, 266-277 (2001).
81. Lasjaunias, P., Berenstein, A. & Brugge, K.T. *Clinical Vascular Anatomy and Variations*, (Springer Berlin Heidelberg, 2013).
82. Rhoton, A.L. *Rhoton's Cranial Anatomy and Surgical Approaches*, (Lippincott Williams & Wilkins, 2007).
83. Osborn, A.G. & Jacobs, J.M. *Diagnostic Cerebral Angiography*, (Lippincott Williams & Wilkins, 1999).
84. Krejza, J., *et al.* Carotid artery diameter in men and women and the relation to body and neck size. *Stroke* **37**, 1103-1105 (2006).
85. Lee, V.S., Hertzberg, B.S., Kliewer, M.A. & Carroll, B.A. Assessment of Stenosis: Implications of Variability of Doppler Measurements in Normal-appearing Carotid Arteries 1. *Radiology* **212**, 493-498 (1999).

86. Bendel, P., Buonocore, E., Bockisch, A. & Besozzi, M.C. Blood flow in the carotid arteries: quantification by using phase-sensitive MR imaging. *AJR. American journal of roentgenology* **152**, 1307-1310 (1989).
87. Manniesing, R., *et al.* Robust CTA lumen segmentation of the atherosclerotic carotid artery bifurcation in a large patient population. *Medical Image Analysis* **14**, 759-769 (2010).
88. Tang, H., *et al.* Semiautomatic carotid lumen segmentation for quantification of lumen geometry in multispectral MRI. *Medical Image Analysis* **16**, 1202-1215 (2012).
89. Chung, A., Noble, J.A. & Summers, P. Vascular segmentation of phase contrast magnetic resonance angiograms based on statistical mixture modeling and local phase coherence. *Medical Imaging, IEEE Transactions on* **23**, 1490-1507 (2004).
90. Persson, M., Solem, J., Markenroth, K., Svensson, J. & Heyden, A. Phase Contrast MRI Segmentation Using Velocity and Intensity. in *Scale Space and PDE Methods in Computer Vision*, Vol. 3459 (eds. Kimmel, R., Sochen, N. & Weickert, J.) 119-130 (Springer Berlin Heidelberg, 2005).
91. Solem, J., Persson, M. & Heyden, A. Velocity Based Segmentation in Phase Contrast MRI Images. in *Medical Image Computing and Computer-Assisted Intervention – MICCAI 2004*, Vol. 3216 (eds. Barillot, C., Haynor, D. & Hellier, P.) 459-466 (Springer Berlin Heidelberg, 2004).
92. Fasquel, J.-B., Lécluse, A., Cavaro-Ménard, C. & Willoteaux, S. A semi-automated method for measuring the evolution of both lumen area and blood flow in carotid from Phase Contrast MRI. *Computers in Biology and Medicine* **66**, 269-277 (2015).
93. Klabunde, R. *Cardiovascular Physiology Concepts*, (Wolters Kluwer Health, 2011).
94. Chodzynski, K.J., *et al.* An in vitro test bench reproducing coronary blood flow signals. *Biomedical engineering online* **14**, 77 (2015).
95. Levine, W.S. *Control System Fundamentals*, (Taylor & Francis, 1999).
96. Garcia, C.E. & Morari, M. Internal model control. A unifying review and some new results. *Industrial & Engineering Chemistry Process Design and Development* **21**, 308-323 (1982).
97. Paramasivam, S., Baltasvias, G., Psatha, E., Matis, G. & Valavanis, A. Silicone models as basic training and research aid in endovascular neurointervention—a single-center experience and review of the literature. *Neurosurgical review* **37**, 331-337 (2014).
98. Becske, T., *et al.* Pipeline for uncoilable or failed aneurysms: results from a multicenter clinical trial. *Radiology* **267**, 858-868 (2013).
99. Chodzyński, K.J., *et al.* An in vitro test bench reproducing coronary blood flow signals. *Biomedical engineering online* **14**, 1-26 (2015).
100. Ripley, B.D. The R project in statistical computing. *MSOR Connections. The newsletter of the LTSN Maths, Stats & OR Network* **1**, 23-25 (2001).
101. Westerhof, N., Lankhaar, J.W. & Westerhof, B.E. The arterial Windkessel. *Medical & biological engineering & computing* **47**, 131-141 (2009).
102. Gwilliam, M.N., *et al.* MR derived volumetric flow rate waveforms at locations within the common carotid, internal carotid, and basilar arteries. *J Cereb Blood Flow Metab* **29**, 1975-1982 (2009).

103. Ford, M.D., Alperin, N., Lee, S.H., Holdsworth, D.W. & Steinman, D.A. Characterization of volumetric flow rate waveforms in the normal internal carotid and vertebral arteries. *Physiol Meas* **26**, 477-488 (2005).
104. Marks, M.P., Pelc, N.J., Ross, M.R. & Enzmann, D.R. Determination of cerebral blood flow with a phase-contrast cine MR imaging technique: evaluation of normal subjects and patients with arteriovenous malformations. *Radiology* **182**, 467-476 (1992).
105. Marshall, I., Papathanasopoulou, P. & Wartolowska, K. Carotid flow rates and flow division at the bifurcation in healthy volunteers. *Physiol Meas* **25**, 691-697 (2004).
106. Wells, C.E., Pugh, N.D. & Woodcock, J.P. Abdominal aortic aneurysm detection by common femoral artery Doppler ultrasound waveform analysis. *Journal of medical engineering & technology* **35**, 34-39 (2011).
107. Barbosa, D., *et al.* B-spline explicit active surfaces: an efficient framework for real-time 3-D region-based segmentation. *IEEE transactions on image processing : a publication of the IEEE Signal Processing Society* **21**, 241-251 (2012).
108. Johnston, K.W., Maruzzo, B.C. & Cobbold, R.S. Doppler methods for quantitative measurement and localization of peripheral arterial occlusive disease by analysis of the blood flow velocity waveform. *Ultrasound in medicine & biology* **4**, 209-223 (1978).
109. Hendrikse, J., van Raamt, A.F., van der Graaf, Y., Mali, W.P. & van der Grond, J. Distribution of cerebral blood flow in the circle of Willis. *Radiology* **235**, 184-189 (2005).
110. Steiger, H.J., Aaslid, R., Keller, S. & Reulen, H.J. Strength, elasticity and viscoelastic properties of cerebral aneurysms. *Heart Vessels* **5**, 41-46 (1989).
111. Costalat, V., *et al.* Biomechanical wall properties of human intracranial aneurysms resected following surgical clipping (IRRA Project). *J Biomech* **44**, 2685-2691 (2011).
112. Sanchez, M., *et al.* Biomechanical assessment of the individual risk of rupture of cerebral aneurysms: a proof of concept. *Annals of biomedical engineering* **41**, 28-40 (2013).
113. Wong, G.K. & Poon, W.S. Current status of computational fluid dynamics for cerebral aneurysms: the clinician's perspective. *Journal of clinical neuroscience : official journal of the Neurosurgical Society of Australasia* **18**, 1285-1288 (2011).
114. Murakami, H., Inaba, M., Nakamura, A. & Ushioda, T. Ipsilateral hyperperfusion after neck clipping of a giant internal carotid artery aneurysm. Case report. *J Neurosurg* **97**, 1233-1236 (2002).
115. Chiu, A.H. & Wenderoth, J. Cerebral hyperperfusion after flow diversion of large intracranial aneurysms. *Journal of neurointerventional surgery* **5**, e48 (2013).
116. Mumford, D. & Shah, J. Optimal approximations by piecewise smooth functions and associated variational problems. *Communications on pure and applied mathematics* **42**, 577-685 (1989).
117. Deverdun, J. Université Montpellier 2 (2015).
118. Balédent, O., Henry-Feugeas, M.C. & Idy-Peretti, I. Cerebrospinal fluid dynamics and relation with blood flow: a magnetic resonance study with semiautomated cerebrospinal fluid segmentation. *Investigative radiology* **36**, 368-377 (2001).

119. Cooley, J.W. & Tukey, J.W. An algorithm for the machine calculation of complex Fourier series. *Mathematics of computation* **19**, 297-301 (1965).
120. Heiberg, E., Markenroth, K. & Arheden, H. Validation of free software for automated vessel delineation and MRI flow analysis. *Journal of Cardiovascular Magnetic Resonance* **9**, 375 (2007).
121. Heiberg, E., *et al.* Design and validation of Segment--freely available software for cardiovascular image analysis. *BMC medical imaging* **10**, 1 (2010).
122. Bidhult, S.L., Carlsson, M., Steding-Ehrenborg, K., Arheden, H. & Heiberg, E. A new method for vessel segmentation based on a priori input from medical expertise in cine phase-contrast Magnetic Resonance Imaging. *Journal of Cardiovascular Magnetic Resonance* **16**, 1-2 (2014).
123. Lawrence, I. & Lin, K. A concordance correlation coefficient to evaluate reproducibility. *Biometrics*, 255-268 (1989).
124. Lawrence, I. & Lin, K. Assay validation using the concordance correlation coefficient. *Biometrics*, 599-604 (1992).
125. Shi, Y. *Lumped-parameter Modelling of Cardiovascular System Dynamics Under Different Healthy and Diseased Conditions*, (University of Sheffield, 2013).
126. Murray, K.D. Dimensions of the circle of Willis and dynamic studies using electrical analogy. *Journal of neurosurgery* **21**, 26-34 (1964).
127. Olufsen, M.S., Nadim, A. & Lipsitz, L.A. Dynamics of cerebral blood flow regulation explained using a lumped parameter model. *American Journal of Physiology - Regulatory, Integrative and Comparative Physiology* **282**, R611-R622 (2002).

Appendix

8 Appendix

8.1 APPENDIX 1

Configuration of Circle of Willis and mean Blood Flow Rates

	N	Complete Circle of Willis [†]	Anterior Communicating artery	Ipsilateral A1 segment **	Ipsilateral Posterior Communicating artery [‡]	MBFR BEVT (mL/min) [§]		MBFR AEVT (mL/min) [§]		MBFR FU (mL/min) [§]		P-value
						Up-S	Down-S	Up-S	Down-S	Up-S	Down-S	
Patient group	1	-	+	I<C	-	181	173	264	243	246	228	0.44 [‡]
	2	-	+	I=C	-	222	211	210	198	243	226	
	3	+	+	I=C	+f	277	258	299	278	328	317	
	4	-	+	I=C	-	338	286	351	na	296	na	
	5	-	+	I=C	+d	194	234	202	223	262	239	
	6	-	+	I=C	+f	253	227	264	244	227	212	
	7	-	+	I>C	-	310	269	296	252	232	218	
	8	+	+	I<C	+s	138	133	na	na	na	na	
	9	+	+	I<C	+s	156	156	205	185	179	167	
	10	-	+	I=C	-	267	232	241	348	316	272	
Mean±SD						234±66	218±50	259±50	246±51	259±47	235±44	
Control group	1	-	+	I=C	-	272	260	272	260	272	260	0.24 [‡]
	2	+	+	I=C	+s	368	350	368	350	368	350	
	3	-	+	I=C	-	266	255	266	255	266	255	
	4	+	+	I=C	+s	274	259	274	259	274	259	
	5	-	+	I=C	+f	316	359	316	359	316	359	
	6	+	+	I=C	+d	317	294	317	294	317	294	
	7	+	+	I=C	+s	316	300	316	300	316	300	
	8	+	+	I<C	+d	325	306	325	306	325	306	
	9	+	+	I=C	+d	341	314	341	314	341	314	
	10	+	+	I=C	+f	265	241	265	241	265	241	
Mean±SD						306±35	294±40	306±35	294±40	306±35	294±40	
P-value						0.02 [‡]	<0.01 [‡]	0.02 [‡]	0.03 [‡]	0.02 [‡]	0.01 [‡]	

* No complete circle of Willis (-) versus Complete circle of Willis (+).

** I<C: Dominant contralateral A1 segment and small ipsilateral A1 segment; I=C: co-dominant A1 segments; I>C: dominant ipsilateral A1 segment.

† (-): No ipsilateral posterior communicating artery; (+d): developed ipsilateral posterior communicating artery; (+f): fetal type ipsilateral posterior communicating artery; (+s): small ipsilateral posterior communicating artery.

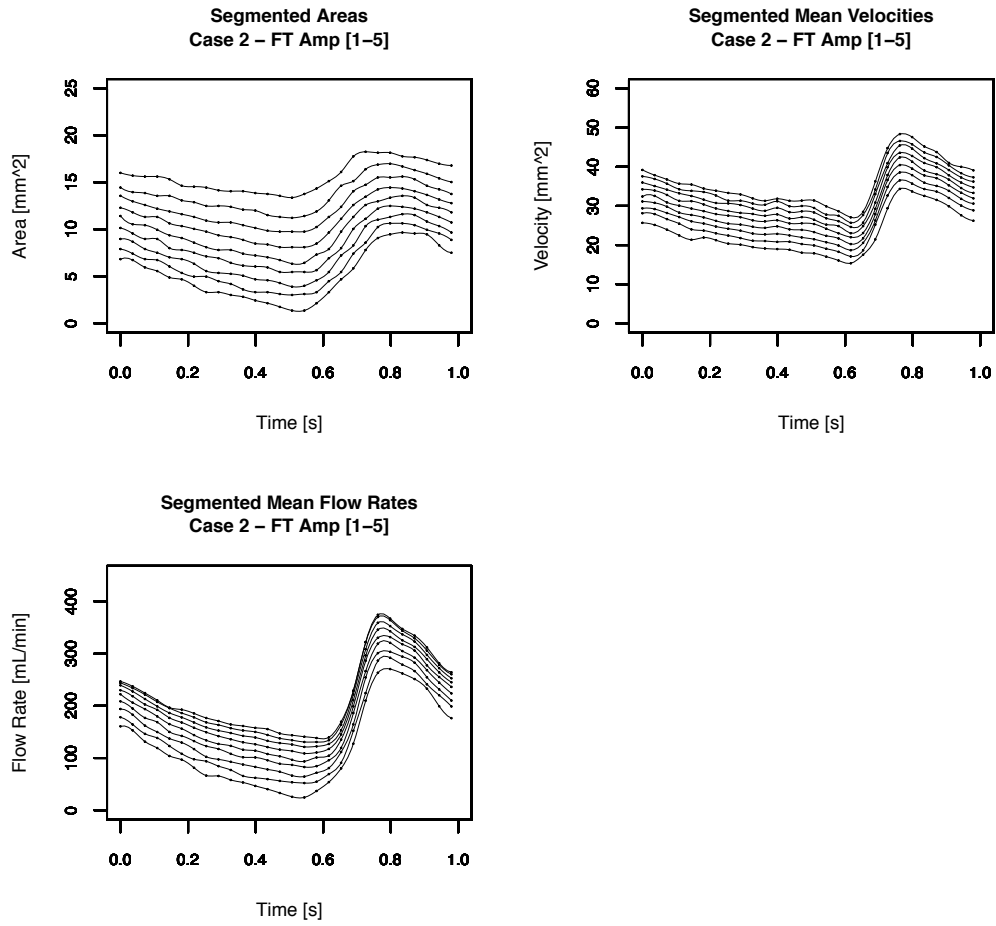
§ MBFR: mean blood flow rate; BEVT: before the endovascular treatment; AEVT: after endovascular treatment; FU: at follow-up; Up-S: upstream; Down-S: downstream.

‡ Kruskal-Wallis Rank Sum Test for the comparison of MBFR in patient group. † Mann-Whitney Rank two-sided Test for the comparison of MBFR between patient and control group.

8.2 APPENDIX 2

Case 2

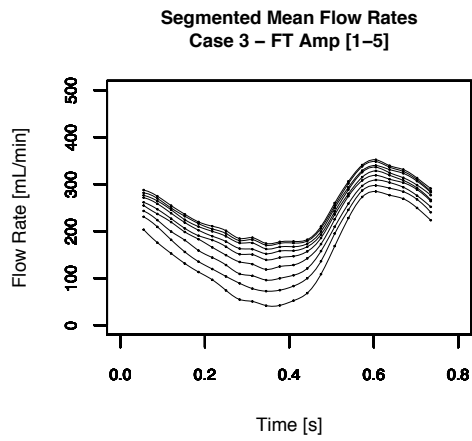
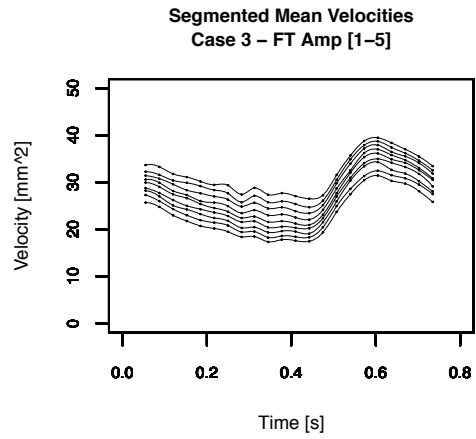
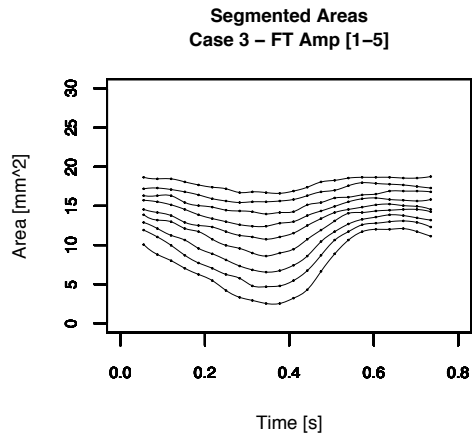
Curves $A(t)$, $V(t)$ and $D(t)$ over a cardiac cycle for each value i of Amp



8.3 APPENDIX 3

Case 3

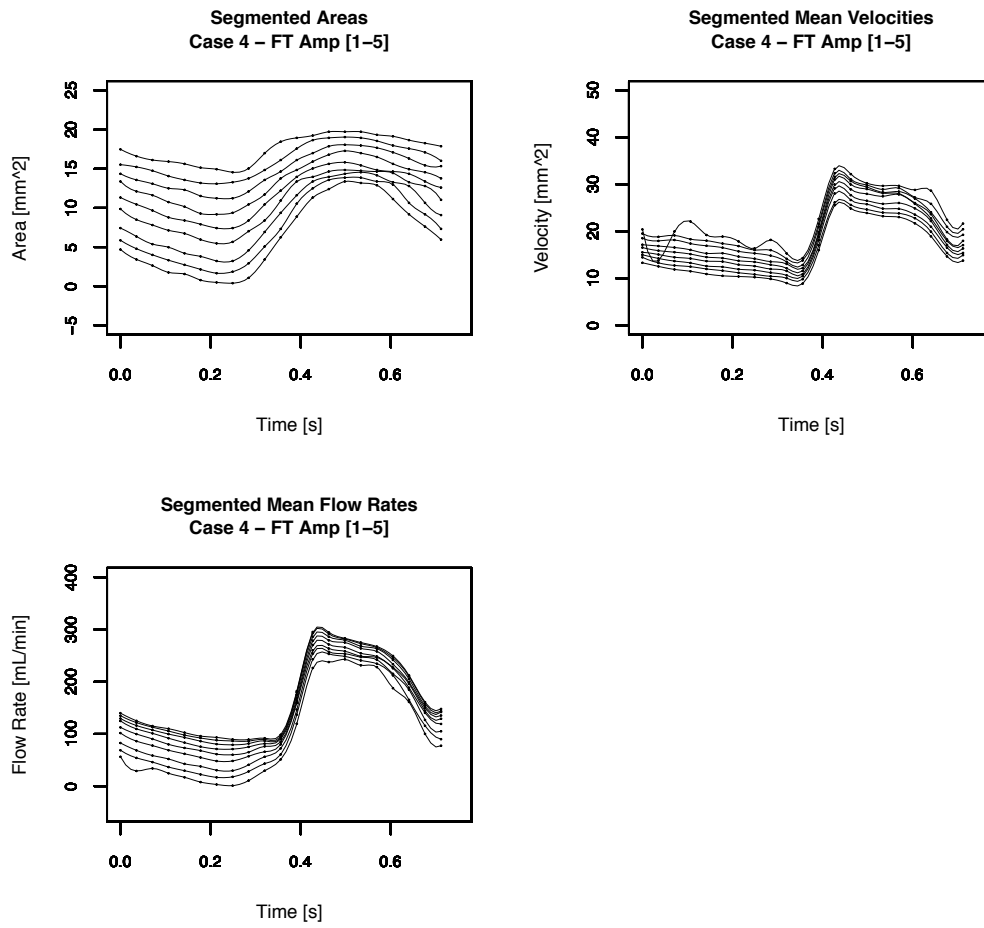
Curves $A(t)$, $V(t)$ and $D(t)$ over a cardiac cycle for each value i of Amp



8.4 APPENDIX 4

Case 4

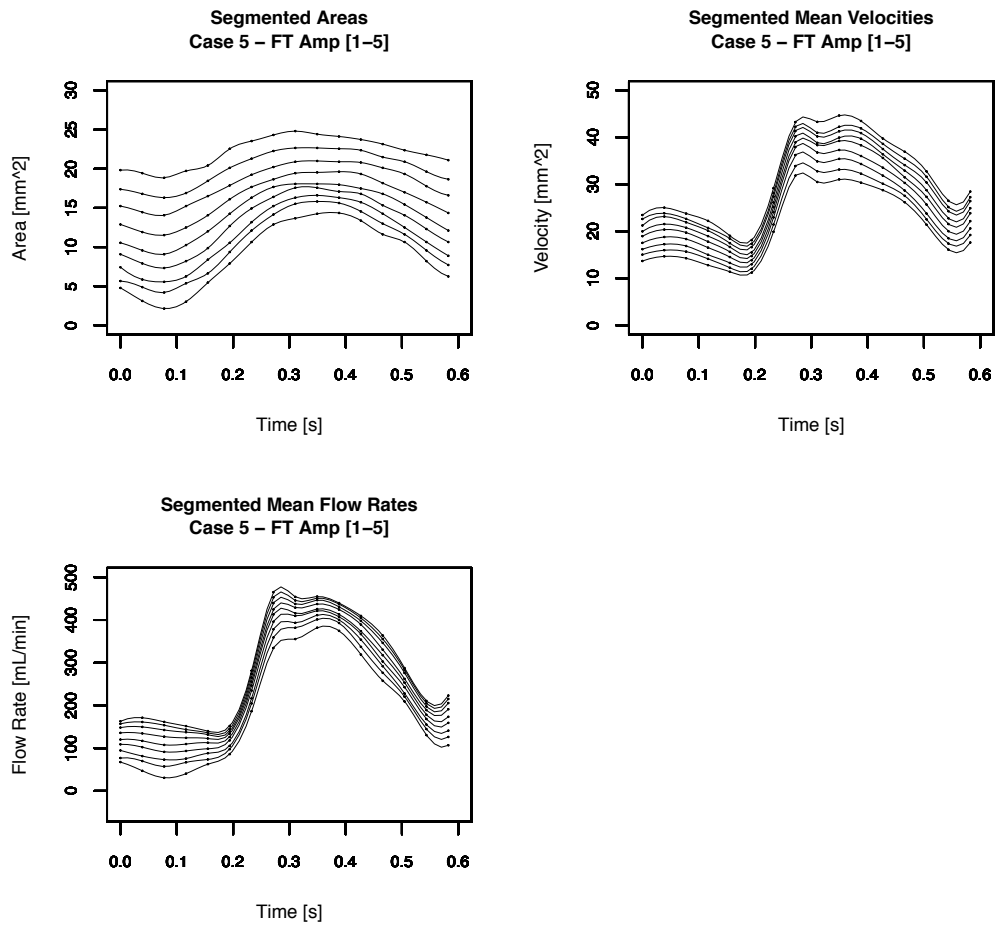
Curves $A(t)$, $V(t)$ and $D(t)$ over a cardiac cycle for each value i of Amp



8.5 APPENDIX 5

Case 4

Curves $A(t)$, $V(t)$ and $D(t)$ over a cardiac cycle for each value i of Amp



8.6 APPENDIX 6

		CASE 1	FT Amplitude values								
			1	1.5	2	2.5	3	3.5	4	4.5	5
FT Method versus Manual Method	Areas	\$rho.c	0.087	0.167	0.343	0.729	0.940	0.684	0.415	0.285	0.192
		\$LowerCI	0.034	0.076	0.184	0.551	0.865	0.501	0.245	0.150	0.092
		\$UpperCI	0.139	0.255	0.484	0.844	0.974	0.808	0.561	0.409	0.289
		\$s.shift	1.852	1.670	1.414	1.099	0.936	0.684	0.552	0.467	0.410
		\$l.shift	-4.281	-3.005	-1.807	-0.758	0.107	0.766	1.481	2.025	2.656
		\$C.b	0.097	0.177	0.371	0.774	0.992	0.732	0.439	0.298	0.202
	Mean Velocities	\$rho.c	0.770	0.870	0.947	0.983	0.982	0.944	0.855	0.748	0.611
		\$LowerCI	0.630	0.772	0.895	0.964	0.962	0.891	0.748	0.597	0.434
		\$UpperCI	0.861	0.928	0.973	0.992	0.992	0.971	0.919	0.848	0.742
		\$s.shift	1.125	1.107	1.072	1.075	1.068	1.115	1.162	1.221	1.304
		\$l.shift	0.749	0.515	0.292	0.096	-0.107	-0.290	-0.536	-0.766	-1.065
		\$C.b	0.777	0.879	0.957	0.993	0.992	0.954	0.866	0.761	0.624
	Mean Flow Rates	\$rho.c	0.908	0.930	0.955	0.981	0.991	0.975	0.911	0.815	0.678
		\$LowerCI	0.837	0.874	0.915	0.962	0.983	0.947	0.836	0.692	0.515
		\$UpperCI	0.949	0.962	0.976	0.990	0.996	0.989	0.952	0.892	0.794
		\$s.shift	1.144	1.143	1.138	1.107	1.081	1.006	0.936	0.869	0.811
		\$l.shift	-0.417	-0.350	-0.256	-0.136	0.014	0.177	0.412	0.639	0.938
		\$C.b	0.913	0.934	0.960	0.986	0.997	0.985	0.920	0.824	0.684
FT Method versus Active Contour Method (Chan-Vese)	Areas	\$rho.c	0.039	0.066	0.119	0.267	0.548	0.749	0.567	0.363	0.223
		\$LowerCI	0.015	0.027	0.050	0.137	0.363	0.646	0.418	0.216	0.112
		\$UpperCI	0.063	0.106	0.187	0.387	0.691	0.826	0.686	0.494	0.329
		\$s.shift	1.384	1.249	1.057	0.821	0.699	0.512	0.413	0.349	0.306
		\$l.shift	-6.763	-5.196	-3.672	-2.271	-1.163	-0.215	0.724	1.433	2.220
		\$C.b	0.042	0.069	0.129	0.278	0.574	0.796	0.595	0.379	0.235
	Mean Velocities	\$rho.c	0.676	0.779	0.877	0.942	0.983	0.983	0.938	0.857	0.728
		\$LowerCI	0.515	0.646	0.789	0.896	0.970	0.974	0.891	0.757	0.577
		\$UpperCI	0.790	0.866	0.929	0.968	0.991	0.988	0.965	0.917	0.831
		\$s.shift	1.191	1.171	1.135	1.138	1.130	1.179	1.230	1.291	1.380
		\$l.shift	0.962	0.732	0.512	0.321	0.123	-0.050	-0.284	-0.502	-0.784
		\$C.b	0.677	0.781	0.878	0.943	0.985	0.985	0.942	0.863	0.736
	Mean Flow Rates	\$rho.c	0.745	0.778	0.823	0.880	0.936	0.966	0.955	0.881	0.741
		\$LowerCI	0.600	0.645	0.706	0.792	0.882	0.938	0.926	0.799	0.597
		\$UpperCI	0.843	0.866	0.896	0.932	0.966	0.982	0.972	0.930	0.839
		\$s.shift	0.956	0.955	0.951	0.925	0.903	0.841	0.782	0.727	0.678
		\$l.shift	-0.820	-0.747	-0.643	-0.506	-0.339	-0.148	0.122	0.382	0.719
		\$C.b	0.748	0.781	0.828	0.884	0.941	0.975	0.964	0.889	0.749

\$rho.c is the the concordance correlation coefficient, \$UpperCI and \$LowerCI its con fiance interval with 95% of confidence, s.shift is the scale shift, l.shift is the location shift, C.b is the a bias correction factor that measures how far the best-fit line deviates from a line at 45 degrees. No deviation from the 45 degree line occurs when C.b = 1.

8.7 APPENDIX 7

		CASE 2	FT Amplitude values								
			1	1.5	2	2.5	3	3.5	4	4.5	5
FT Method versus Manual Method)	Areas	\$rho.c	0.116	0.258	0.499	0.774	0.740	0.542	0.357	0.248	0.179
		\$LowerCI	0.058	0.148	0.346	0.676	0.644	0.391	0.222	0.140	0.095
		\$UpperCI	0.174	0.361	0.627	0.846	0.813	0.664	0.479	0.350	0.260
		\$s.shift	0.760	0.666	0.612	0.566	0.513	0.504	0.476	0.463	0.445
		\$l.shift	-3.760	-2.314	-1.276	-0.398	0.359	1.028	1.662	2.243	2.807
		\$C.b	0.123	0.266	0.516	0.803	0.772	0.564	0.375	0.261	0.189
	Mean Velocities	\$rho.c	0.649	0.815	0.919	0.973	0.962	0.909	0.816	0.720	0.625
		\$LowerCI	0.505	0.714	0.866	0.957	0.937	0.848	0.711	0.587	0.476
		\$UpperCI	0.758	0.883	0.951	0.983	0.977	0.946	0.885	0.816	0.739
		\$s.shift	1.255	1.221	1.212	1.202	1.219	1.205	1.209	1.200	1.190
		\$l.shift	1.004	0.637	0.361	0.102	-0.147	-0.383	-0.622	-0.842	-1.060
		\$C.b	0.654	0.818	0.923	0.978	0.970	0.917	0.825	0.729	0.634
	Mean Flow Rates	\$rho.c	0.889	0.917	0.953	0.979	0.983	0.961	0.900	0.812	0.700
		\$LowerCI	0.820	0.863	0.921	0.966	0.975	0.935	0.835	0.707	0.563
		\$UpperCI	0.932	0.950	0.972	0.987	0.988	0.977	0.940	0.882	0.800
		\$s.shift	0.892	0.871	0.869	0.865	0.851	0.851	0.840	0.836	0.828
		\$l.shift	-0.484	-0.401	-0.276	-0.129	0.037	0.215	0.423	0.640	0.888
		\$C.b	0.890	0.917	0.954	0.982	0.986	0.965	0.905	0.819	0.708
FT Method versus Active Contour Method (Chan-Vese)	Areas	\$rho.c	0.089	0.188	0.363	0.632	0.784	0.678	0.466	0.321	0.226
		\$LowerCI	0.043	0.101	0.228	0.492	0.743	0.563	0.324	0.198	0.129
		\$UpperCI	0.135	0.271	0.484	0.741	0.818	0.766	0.587	0.434	0.319
		\$s.shift	0.739	0.648	0.595	0.550	0.499	0.491	0.463	0.450	0.433
		\$l.shift	-4.336	-2.837	-1.764	-0.856	-0.067	0.616	1.271	1.865	2.445
		\$C.b	0.096	0.195	0.371	0.645	0.798	0.688	0.472	0.325	0.229
	Mean Velocities	\$rho.c	0.590	0.754	0.871	0.951	0.974	0.949	0.875	0.785	0.689
		\$LowerCI	0.441	0.633	0.794	0.919	0.962	0.914	0.797	0.671	0.550
		\$UpperCI	0.708	0.839	0.921	0.971	0.982	0.970	0.924	0.863	0.790
		\$s.shift	1.259	1.225	1.216	1.207	1.223	1.209	1.213	1.204	1.194
		\$l.shift	1.144	0.775	0.500	0.240	-0.008	-0.244	-0.482	-0.702	-0.920
		\$C.b	0.595	0.757	0.874	0.956	0.980	0.954	0.881	0.791	0.695
	Mean Flow Rates	\$rho.c	0.835	0.868	0.914	0.954	0.975	0.972	0.926	0.848	0.737
		\$LowerCI	0.742	0.789	0.860	0.926	0.966	0.958	0.879	0.760	0.610
		\$UpperCI	0.897	0.918	0.948	0.972	0.982	0.981	0.955	0.905	0.827
		\$s.shift	0.855	0.834	0.832	0.829	0.815	0.815	0.805	0.801	0.793
		\$l.shift	-0.604	-0.518	-0.390	-0.239	-0.069	0.113	0.326	0.548	0.801
		\$C.b	0.837	0.869	0.915	0.956	0.977	0.973	0.929	0.851	0.742

\$rho.c is the the concordance correlation coefficient, \$UpperCI and \$LowerCI its con fiance interval with 95% of confidence, s.shift is the scale shift, l.shift is the location shift, C.b is the a bias correction factor that measures how far the best-fit line deviates from a line at 45 degrees. No deviation from the 45 degree line occurs when C.b = 1.

8.8 APPENDIX 8

CASE 3		FT Amplitude values									
		1	1.5	2	2.5	3	3.5	4	4.5	5	
FT Method versus Manual Method	Areas	\$rho.c	0.092	0.187	0.358	0.640	0.641	0.501	0.357	0.277	0.201
		\$LowerCI	0.021	0.054	0.135	0.377	0.409	0.267	0.155	0.105	0.066
		\$UpperCI	0.162	0.313	0.547	0.807	0.795	0.679	0.530	0.432	0.329
		\$s.shift	0.840	0.725	0.673	0.574	0.507	0.452	0.416	0.400	0.388
		\$l.shift	-3.976	-2.594	-1.549	-0.508	0.317	0.857	1.419	1.825	2.359
		\$C.b	0.112	0.226	0.439	0.777	0.775	0.589	0.414	0.321	0.235
	Mean Velocities	\$rho.c	0.806	0.884	0.946	0.979	0.986	0.972	0.940	0.910	0.862
		\$LowerCI	0.652	0.776	0.887	0.954	0.968	0.936	0.871	0.815	0.733
		\$UpperCI	0.896	0.942	0.974	0.991	0.994	0.988	0.973	0.957	0.931
		\$s.shift	1.277	1.224	1.162	1.135	1.110	1.112	1.109	1.101	1.064
		\$l.shift	0.639	0.455	0.281	0.108	-0.055	-0.171	-0.309	-0.409	-0.540
		\$C.b	0.810	0.889	0.952	0.986	0.993	0.980	0.950	0.919	0.871
	Mean Flow Rates	\$rho.c	0.949	0.964	0.978	0.990	0.991	0.982	0.960	0.931	0.875
		\$LowerCI	0.897	0.926	0.953	0.978	0.982	0.961	0.912	0.854	0.751
		\$UpperCI	0.975	0.983	0.990	0.995	0.996	0.992	0.982	0.968	0.939
		\$s.shift	0.921	0.920	0.920	0.915	0.910	0.894	0.883	0.883	0.890
		\$l.shift	-0.314	-0.257	-0.189	-0.094	0.015	0.109	0.229	0.333	0.488
		\$C.b	0.950	0.965	0.979	0.992	0.995	0.988	0.967	0.941	0.888
FT Method versus Active Contour Method (Chan-Vese)	Areas	\$rho.c	0.039	0.076	0.141	0.297	0.428	0.396	0.296	0.227	0.159
		\$LowerCI	0.009	0.019	0.041	0.126	0.286	0.273	0.155	0.098	0.056
		\$UpperCI	0.070	0.132	0.239	0.451	0.552	0.507	0.425	0.349	0.259
		\$s.shift	0.457	0.395	0.367	0.313	0.276	0.246	0.227	0.218	0.212
		\$l.shift	-6.392	-4.448	-2.999	-1.519	-0.351	0.423	1.215	1.779	2.512
		\$C.b	0.046	0.088	0.165	0.344	0.497	0.446	0.327	0.251	0.178
	Mean Velocities	\$rho.c	0.762	0.842	0.911	0.956	0.977	0.974	0.956	0.934	0.899
		\$LowerCI	0.592	0.711	0.827	0.913	0.959	0.951	0.907	0.863	0.796
		\$UpperCI	0.867	0.916	0.955	0.978	0.987	0.986	0.979	0.969	0.951
		\$s.shift	1.376	1.319	1.251	1.222	1.195	1.198	1.195	1.186	1.146
		\$l.shift	0.715	0.536	0.365	0.197	0.040	-0.072	-0.205	-0.302	-0.430
		\$C.b	0.765	0.846	0.916	0.962	0.984	0.981	0.964	0.943	0.908
	Mean Flow Rates	\$rho.c	0.878	0.900	0.924	0.949	0.967	0.971	0.964	0.947	0.905
		\$LowerCI	0.768	0.808	0.851	0.901	0.942	0.957	0.940	0.900	0.811
		\$UpperCI	0.937	0.949	0.962	0.974	0.982	0.981	0.978	0.973	0.953
		\$s.shift	0.824	0.824	0.824	0.819	0.814	0.800	0.791	0.790	0.797
		\$l.shift	-0.484	-0.423	-0.352	-0.250	-0.135	-0.034	0.094	0.204	0.367
		\$C.b	0.880	0.902	0.925	0.951	0.971	0.975	0.969	0.954	0.915

\$rho.c is the the concordance correlation coefficient, \$UpperCI and \$LowerCI its confiance interval with 95% of confidence, s.shift is the scale shift, l.shift is the location shift, C.b is the a bias correction factor that measures how far the best-fit line deviates from a line at 45 degrees. No deviation from the 45 degree line occurs when C.b = 1.

8.9 APPENDIX 9

CASE 4		FT Amplitude values									
		1	1.5	2	2.5	3	3.5	4	4.5	5	
FT Method versus Manual Method	Areas	\$rho.c	0.840	0.848	0.863	0.885	0.904	0.913	0.905	0.860	0.840
		\$LowerCI	0.758	0.771	0.794	0.830	0.866	0.894	0.888	0.813	0.758
		\$UpperCI	0.895	0.901	0.910	0.923	0.932	0.929	0.920	0.897	0.895
		\$s.shift	0.708	0.707	0.702	0.695	0.681	0.663	0.644	0.614	0.708
		\$l.shift	-0.498	-0.474	-0.427	-0.343	-0.234	-0.100	0.077	0.269	-0.498
		\$C.b	0.845	0.853	0.866	0.888	0.907	0.917	0.908	0.864	0.845
	Mean Velocities	\$rho.c	0.826	0.929	0.978	0.990	0.978	0.946	0.893	0.824	0.826
		\$LowerCI	0.728	0.879	0.961	0.982	0.962	0.909	0.829	0.731	0.728
		\$UpperCI	0.890	0.959	0.988	0.994	0.988	0.968	0.934	0.887	0.890
		\$s.shift	1.019	1.060	1.085	1.089	1.099	1.121	1.147	1.187	1.019
		\$l.shift	0.623	0.357	0.156	0.003	-0.160	-0.302	-0.459	-0.618	0.623
		\$C.b	0.837	0.939	0.985	0.996	0.983	0.951	0.897	0.829	0.837
	Mean Flow Rates	\$rho.c	0.929	0.935	0.945	0.958	0.965	0.959	0.933	0.876	0.929
		\$LowerCI	0.885	0.896	0.912	0.936	0.953	0.948	0.901	0.813	0.885
		\$UpperCI	0.956	0.960	0.966	0.972	0.974	0.968	0.954	0.918	0.956
		\$s.shift	0.814	0.813	0.807	0.799	0.783	0.761	0.740	0.705	0.814
		\$l.shift	-0.315	-0.293	-0.249	-0.172	-0.072	0.051	0.215	0.390	-0.315
		\$C.b	0.934	0.939	0.949	0.961	0.968	0.963	0.936	0.879	0.934
FT Method versus Active Contour Method (Chan-Vese)	Areas	\$rho.c	0.100	0.225	0.373	0.524	0.624	0.571	0.444	0.325	0.100
		\$LowerCI	0.051	0.130	0.243	0.390	0.544	0.493	0.332	0.215	0.051
		\$UpperCI	0.149	0.316	0.490	0.637	0.692	0.641	0.544	0.426	0.149
		\$s.shift	0.696	0.543	0.476	0.431	0.389	0.349	0.316	0.282	0.696
		\$l.shift	-4.007	-2.458	-1.597	-0.929	-0.282	0.286	0.879	1.406	-4.007
		\$C.b	0.110	0.237	0.390	0.553	0.658	0.606	0.470	0.344	0.110
	Mean Velocities	\$rho.c	0.788	0.898	0.958	0.981	0.983	0.961	0.917	0.855	0.788
		\$LowerCI	0.675	0.829	0.926	0.964	0.970	0.931	0.863	0.773	0.675
		\$UpperCI	0.865	0.940	0.977	0.990	0.991	0.978	0.950	0.910	0.865
		\$s.shift	1.028	1.070	1.095	1.098	1.109	1.130	1.157	1.197	1.028
		\$l.shift	0.698	0.434	0.235	0.083	-0.079	-0.220	-0.375	-0.532	0.698
		\$C.b	0.804	0.912	0.969	0.992	0.992	0.969	0.925	0.864	0.804
	Mean Flow Rates	\$rho.c	0.840	0.848	0.863	0.885	0.904	0.913	0.905	0.860	0.840
		\$LowerCI	0.758	0.771	0.794	0.830	0.866	0.894	0.888	0.813	0.758
		\$UpperCI	0.895	0.901	0.910	0.923	0.932	0.929	0.920	0.897	0.895
		\$s.shift	0.708	0.707	0.702	0.695	0.681	0.663	0.644	0.614	0.708
		\$l.shift	-0.498	-0.474	-0.427	-0.343	-0.234	-0.100	0.077	0.269	-0.498
		\$C.b	0.845	0.853	0.866	0.888	0.907	0.917	0.908	0.864	0.845

\$rho.c is the the concordance correlation coefficient, \$UpperCI and \$LowerCI its confidence interval with 95% of confidence, s.shift is the scale shift, l.shift is the location shift, C.b is the a bias correction factor that measures how far the best-fit line deviates from a line at 45 degrees. No deviation from the 45 degree line occurs when C.b = 1.

8.10 APPENDIX 10

CASE 5			FT Amplitude values								
			1	1.5	2	2.5	3	3.5	4	4.5	5
FT Method versus Manual Method	Areas	\$rho.c	0.082	0.157	0.270	0.452	0.591	0.509	0.347	0.264	0.201
		\$LowerCI	0.082	0.157	0.270	0.452	0.591	0.509	0.347	0.264	0.201
		\$UpperCI	0.029	0.067	0.132	0.275	0.466	0.381	0.209	0.142	0.098
		\$s.shift	0.133	0.244	0.398	0.600	0.693	0.618	0.472	0.379	0.301
		\$l.shift	0.640	0.537	0.482	0.419	0.384	0.330	0.275	0.254	0.244
		\$C.b	-4.359	-3.071	-2.065	-1.103	-0.246	0.425	1.142	1.688	2.225
	Mean Velocities	\$rho.c	0.824	0.876	0.929	0.963	0.983	0.979	0.947	0.906	0.834
		\$LowerCI	0.706	0.787	0.872	0.934	0.972	0.962	0.900	0.829	0.692
		\$UpperCI	0.897	0.930	0.961	0.980	0.990	0.988	0.972	0.950	0.914
		\$s.shift	1.247	1.256	1.218	1.197	1.160	1.164	1.213	1.241	1.189
		\$l.shift	0.609	0.473	0.328	0.186	0.040	-0.073	-0.226	-0.364	-0.501
		\$C.b	0.826	0.879	0.932	0.968	0.988	0.986	0.958	0.918	0.877
	Mean Flow Rates	\$rho.c	0.898	0.913	0.933	0.954	0.970	0.968	0.937	0.897	0.835
		\$LowerCI	0.822	0.846	0.880	0.918	0.951	0.953	0.897	0.826	0.723
		\$UpperCI	0.943	0.951	0.962	0.974	0.981	0.978	0.962	0.940	0.904
		\$s.shift	0.836	0.829	0.825	0.820	0.815	0.792	0.748	0.724	0.714
		\$l.shift	-0.440	-0.394	-0.325	-0.231	-0.114	0.008	0.173	0.322	0.501
		\$C.b	0.899	0.913	0.933	0.956	0.973	0.974	0.946	0.905	0.845
FT Method versus Active Contour Method (Chan-Vese)	Areas	\$rho.c	0.094	0.182	0.322	0.519	0.597	0.460	0.303	0.226	0.172
		\$LowerCI	0.037	0.083	0.173	0.362	0.519	0.332	0.176	0.117	0.082
		\$UpperCI	0.151	0.278	0.456	0.647	0.666	0.572	0.420	0.329	0.260
		\$s.shift	0.592	0.497	0.447	0.388	0.355	0.306	0.255	0.235	0.226
		\$l.shift	-4.138	-2.833	-1.805	-0.829	0.048	0.723	1.444	2.001	2.554
		\$C.b	0.103	0.190	0.336	0.548	0.631	0.488	0.319	0.235	0.179
	Mean Velocities	\$rho.c	0.845	0.895	0.943	0.972	0.986	0.976	0.938	0.892	0.816
		\$LowerCI	0.738	0.817	0.898	0.951	0.977	0.955	0.883	0.804	0.666
		\$UpperCI	0.911	0.941	0.968	0.984	0.991	0.987	0.967	0.941	0.903
		\$s.shift	1.242	1.251	1.213	1.193	1.156	1.160	1.209	1.237	1.185
		\$l.shift	0.561	0.424	0.280	0.137	-0.008	-0.121	-0.275	-0.414	-0.551
		\$C.b	0.847	0.897	0.945	0.976	0.990	0.982	0.947	0.902	0.858
	Mean Flow Rates	\$rho.c	0.918	0.931	0.948	0.966	0.977	0.969	0.932	0.887	0.822
		\$LowerCI	0.855	0.877	0.908	0.941	0.966	0.954	0.886	0.807	0.702
		\$UpperCI	0.954	0.962	0.971	0.980	0.984	0.979	0.960	0.935	0.896
		\$s.shift	0.844	0.837	0.833	0.828	0.822	0.800	0.755	0.731	0.721
		\$l.shift	-0.386	-0.340	-0.272	-0.179	-0.062	0.058	0.221	0.369	0.547
		\$C.b	0.918	0.931	0.949	0.967	0.979	0.974	0.940	0.895	0.831

\$rho.c is the the concordance correlation coefficient, \$UpperCI and \$LowerCI its con fiance interval with 95% of confidence, s.shift is the scale shift, l.shift is the location shift, C.b is the a bias correction factor that measures how far the best-fit line deviates from a line at 45 degrees. No deviation from the 45 degree line occurs when C.b = 1.